# Synthesis and Validation of Flight Control for UAV

A DISSERTATION
SUBMITTED TO THE FACULTY OF THE GRADUATE SCHOOL
OF THE UNIVERSITY OF MINNESOTA
BY

Yew Chai Paw

IN PARTIAL FULFILLMENT OF THE REQUIREMENTS
FOR THE DEGREE OF
DOCTOR OF PHILOSOPHY

Gary J. Balas

December 2009

# Acknowledgements

I would like to express my deepest gratitude to my advisor, Professor Gary Balas for his guidance, helps and precious advices in shaping my research work and exposure gained. I am grateful and appreciate his constant supports and initiatives for the UAV research group that make my research possible. His enthusiasm in research and sense of humor have never fail to surprise me. I am really delighted and never regret the tough decision I made four years ago to come to bitter cold Minnesota to work under him.

I am also grateful to Professor Demoz Gebre-Egziabher who shares his insights and experiences in sensor fusion. I always enjoyed having discussions with him in various research areas. Thanks to my other committee members, Professor Tryphoon Georgiou (I have gathered quite a number of life philosophies from him after attending 3 of his courses) and Professor William Garrard (who happens to be my undergraduate and master theses advisor's advisor) for their constructive advices and criticism.

Thanks to the past and present residents of Control and Dynamics Lab who make it a wonderful place for research with a lot of interactions and activities that kept everyone going days and nights throughout the years. Special thanks to Rohit who has helped and taught me embedded software programming, Abhijit who volunteered to drive the flight test team many early weekend mornings and Balint who always give me valuable advices.

Contributions from the UAV team members have been critical to my research progress. Thanks to the RC pilots, Brian, Christopher, James, Andrew and Troy, for their professional flying skills that saved the UAV from numerous crashes during the flight test, to Tom for his endless help in the ground control software. 4 years stay in Minneapolis would not be great without the colleagues that turned to great caring friends like Arnar, Guijin and Troy. Troy has been an awesome buddy who always help me to reach out and feel home in

Minnesota.

I would also like to thanks my company colleagues, Zhou Min, Lim Kok Yong, Peter Seah, Boyd Loh and Alvin Teng, who took over my job responsibilities and continue to help me one way or another while I am on study leave. I am grateful to my previous lab head, Dr Ho Quan Wai and Dr Cheng Wei Ping for their advices, supports and helps in getting the postgraduate scholarship. Thanks to my bachelor and master thesis advisor, Professor Eicher Low, who has been helping and guiding me all these years towards my PhD dream, not forgetting to mention his important influence on my decision to choose Professor Balas as my PhD advisor.

My gratitude to my sponsor company, DSO National Laboratories, for awarding me the postgraduate scholarship and in giving me the opportunity to fulfill my dream of overseas PhD study. I appreciate the great financial support over the years that makes my study life and overseas stay easier than my peers.

Finally, thanks to my parents for their constant supports while I am away from them these four years.

*Success begins with a fellow's will.*

*It's all in the state of mind.*

*Life's battles don't always go*

*To the stronger or faster man,*

*But sooner or later, the man who wins*

*Is the man who thinks he can!*

**'The Victor' ∼ C W Longenecker**

# Abstract

Unmanned Aerial Vehicles (UAVs) are widely used worldwide for a board range of civil and military applications. There continues to be a growing demand for reliable and low cost UAV systems. This is especially true for small-size mini UAV systems where majority of systems are still deployed as prototypes due to their lack of reliability. Improvement in the modeling, testing and flight control for the small UAVs would increase their reliability during autonomous flight.

The traditional approach used in manned aircraft and large UAV system synthesizing, implementing and validating the flight control system to achieve desired objectives is time consuming and resource intensive. This thesis aims to provide an integrated framework with systematic procedures to synthesize and validate flight controllers. This will help in the certification of UAV system and provide rapid development cycle from simulation to real system flight testing. The effectiveness of the approach is demonstrated by applying the developed framework on a small UAV system that was developed at the University of Minnesota.

The thesis is divided into four main parts. The first part is mathematical modeling of the UAV nonlinear simulation model using first principle theory. Flight test system identification technique is used to extract model and model uncertainty parameters to update the nonlinear simulation model. The nonlinear simulation model developed must be able to simulate the actual UAV flight dynamics accurately for real-time simulation and robust control design purposes. Therefore it is important to include model uncertainties into the nonlinear simulation model developed, especially in small UAV system where its dynamics is less well understood than the full-size aircraft. The second part of the work provides the approach and procedures for uncertainty modeling into the nonlinear simulation model such that realization of linear uncertain model is possible.

The third part of work describes the flight control design and architecture used in the

UAV autopilot system. Classical and model-based control synthesis approaches are presented for roll angle tracking controller to demonstrate the controller synthesis approaches and practical controller implementation issues on the embedded flight computer system. The last part of work blends in all the previous works into the integrated framework for testing and validation of the synthesized controllers. This involves software-in-the-loop, processor-in-the-loop and flight testing of the synthesized controllers using the integrated framework developed.

# Contents

# List of Tables

# List of Figures

# List of Symbols

| | | |
|---|---|---|
| $S$ | Vehicle wing reference area | $(m^2)$ |
| $b$ | Vehicle wing span | $(m)$ |
| $g$ | Gravitational acceleration | $(m/s^2)$ |
| $\bar{c}$ | Vehicle wing chord | $(m)$ |
| $m$ | Vehicle gross takeoff weight | $(kg)$ |
| $p, q, r$ | Vehicle body angular rates | $(rad/s)$ |
| $a_x, a_y, a_z$ | Vehicle body linear accelerations | $(m/s^2)$ |
| $h_x, h_y, h_z$ | Vehicle body earth magnetic field | $(Gauss)$ |
| $V_a$ | Vehicle airspeed | $(m/s)$ |
| $h$ | Vehicle barometric altitude | $(m)$ |
| $v_e, v_n, v_u$ | GPS velocities in ENU frame | $(m/s)$ |
| $u, v, w$ | Vehicle body linear velocities | $(m/s)$ |
| $lon, lat, alt$ | GPS positions in geodetic frame using WGS84 | $(deg, deg, m)$ |
| $X, Y, Z$ | Forces acting on vehicle body x, y and z direction | $(N)$ |
| $L, M, N$ | Moments acting on vehicle body x, y and z direction | $(Nm)$ |
| $\phi, \theta, \psi$ | Vehicle body attitude angles | $(rad)$ |
| $\bar{q}$ | Dynamic pressure | $(Pa)$ |
| $T$ | Thrust of propulsion system | $(N)$ |
| $C_X, C_Y, C_Z$ | Aerodynamic force coefficients in x, y and z direction | $(N)$ |
| $c_l, c_m, c_n$ | Aerodynamic moment coefficients in x, y and z direction | |
| $\alpha, \beta$ | Vehicle angle of attack and sideslip angle | $(rad)$ |
| $I_{xx}, I_{yy}, I_{zz}, I_{xz}$ | Vehicle moment of inertia | $(kgm^2)$ |
| $I_p$ | Propulsion system moment of inertia | $(kgm^2)$ |
| $\omega_p$ | Propeller rotation speed | $(rad/s)$ |
| $\delta_a, \delta_e, \delta_T, \delta_r$ | Aileron, elevator, throttle and rudder control input | $(rad)$ |

# Acronyms

| | |
|---|---|
| **UAV** | Unmanned aerial vehicle |
| **COTS** | Commercial off-the-shelf |
| **RC** | Radio-Controlled |
| **IMU** | Inertia measurement unit |
| **GPS** | Global positioning system |
| **ENU** | Local east, north, up |
| **eCos** | Embedded configurable operating system |
| **PWM** | Pulse-width modulated |
| **RPM** | Revolutions per minute |
| **SIDPAC** | System identification program for aircraft |
| **FFT** | Fast fourier transform |
| **LFT** | Linear Fractional Transformation |
| **USS** | Uncertain state-space |
| **AOA** | Angle of attack |
| **LTI** | Linear Time Invariant |
| **SISO** | Single input single output |
| **MIMO** | Multiple input multiple output |
| **PID** | Proportional-integral-derivative |
| **SIL** | Software-in-the-loop |
| **PIL** | Processor-in-the-loop |
| **AHRS** | Attitude and heading reference system |
| **RTWT** | Real-time window target |
| **UDP** | User datagram protocol |
| **DOF** | Degrees of freedom |

# Chapter 1

# Introduction

## 1.1 Overview

Unmanned Aerial Vehicles (UAVs) are widely used worldwide for a board range of civil and military applications. There continues to be a growing demand for reliable and low cost UAV systems. This is especially true for small-size, mini UAV systems (less than 2 meters wing span) where majority of systems are still deployed as prototypes due to their lack of reliability. Improvement in the modeling, testing and flight control for the small UAVs would increase their reliability during autonomous flight.

The traditional approach used in manned aircraft and large UAV system synthesizing, implementing and validating the flight control system to achieve desired objectives is time consuming and resource intensive. Applying the same techniques to small UAVs is not productive. To reduce cost and time to market, small UAV systems make use of low cost commercial-off-the-shelf autopilots [1]. Most of these autopilots use classical Propotional-integral-derivative (PID) controllers where *ad-hoc* methods are used to tune the controller gains in flight. This methodology is time consuming and high risk. The flight test approach to tuning controller has limitations in performance optimality and robustness. To increase the speed of the development cycle, simulation through flight test and improve system reliability and robustness of the flight control system, it is important to develop an integrated framework to the flight control design process with a set of design tools that enables control engineer to rapidly synthesize, implement, analyze and validate a candidate controller design using iterative development cycles.

Numerous researchers have made the case for an integrated framework in recent years [2–7]. The central paradigm is a model-based development environment for the UAV where different design tools and techniques can be formulated, deployed and applied. The different processes in model-based flight control development (shown in Figure 1.1) are tightly-coupled and the development process will severely hindered if each process is tackled as a separate problem. Hence flight control design must be look at in the context of dynamic modeling, control and model analysis, simulation, control design, real-time implementation, software and hardware-in-the-loop simulation and flight testing.

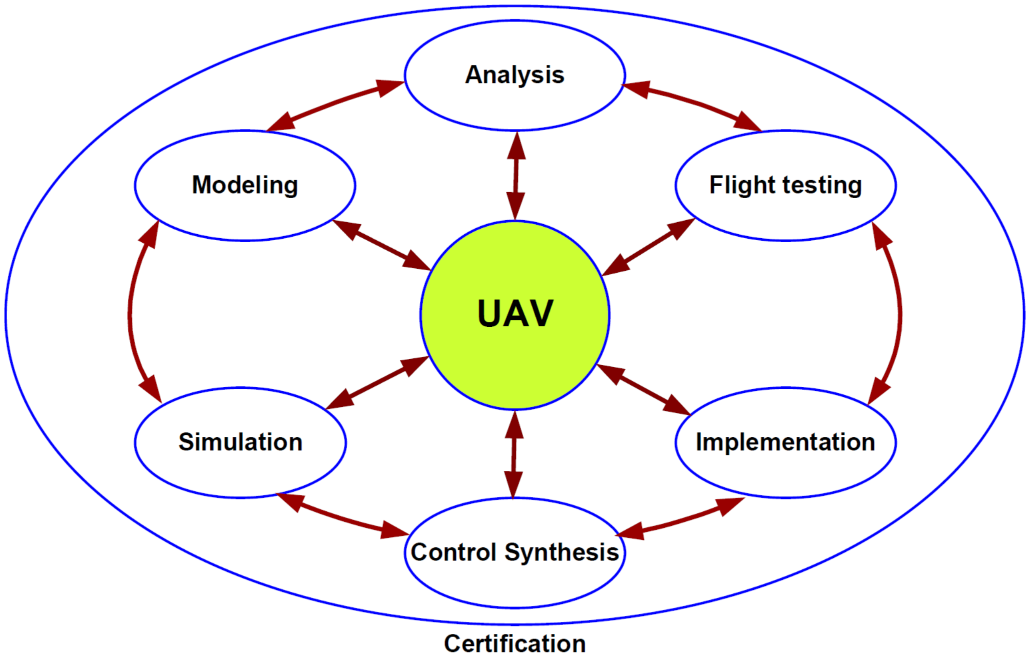

Figure 1.1: Integrated framework for flight control development

## 1.2 Challenges in UAV Flight Control Synthesis and Validation

The task of flight control synthesis and validation involves multi-disciplinary fields that pose challenges in research and development. Many of these challenges identified are the focus of ongoing research. The ability to gain a comprehensive insight into the underlying principles and problems will allow us to focus on the algorithmic steps and intricacies involved in the problem. This allows us to build on past and recent research advancements to accelerate our research progress.

### 1.2.1 High Fidelity Simulation Model

Development of accurate high fidelity simulation model to represent actual flight mechanics requires an in depth understanding of the system dynamics. Three standard approaches to flight dynamic simulation model development are analytical, wind-tunnel and flight test technique. Each approach can be used to complement one another during different phase of model development. A comprehensive model built using all the available complex system behavior does not necessary provide a good model as this might have many redundant parameters, making it too complicated for its intended purpose. A good simulation model should have fidelity required within a specific tolerance with minimum number of parameters. The resulting model is simple, easy to construct, validate and use. Development of these simple, accurate models requires a good understand of flight dynamics and experience in using adequate number of suitable parameters to model the system through suitable experiments. This systematic approach is still quite lacking for small UAV system development.

### 1.2.2 Uncertainty Modeling

Mathematical models are used to describe the behavior of complex physical system. These models are only an approximation of the real system. Model uncertainty accounts for actual system response using the model developed. Hence it is important to include uncertainty during the model development to provide a confidence level as well as a bound on predicting the actual system response. Uncertainty modeling is especially crucial in the model development for small UAV since their aerodynamics data are less well understood than full-size aircraft. In addition, small UAVs are generally more sensitive to wind gust disturbance which are difficult to model. Low cost sensors used onboard result in significant sensor data errors and measurement noise. These are a few of the practical reasons to incorporate uncertainty modeling in the UAV model development.

Incorporating uncertainty modeling leads to the issue of deciding the best approach for deriving and representing model uncertainty (stochastic or deterministic), its practical implementation and its integration into the nonlinear and linear model development. There is no standard approach in the representation for uncertainty modeling due to it being problem dependent problem.

### 1.2.3 Model Validation

Model validation is a necessary step to gain confidence or reject a model based on the input and output experiment data obtained from the system. It is never possible to validate a model on the basis of a finite number of experiments. However, the model can be invalidated by experimental data [8]. Hence model development and validation are closely coupled and integrally related to experimental data.

The fundamental principle used in many model validation techniques is to compare and evaluate the residue between simulated model data and experiment validation data. Different model validation methods result in different non-unique validated model sets. Also, the technique of model validation depends on the uncertainty modeling approach, model and uncertainty assumptions, this dependency makes the task of model validation even harder.

### 1.2.4 Performance Validation

The objective in flight control system development is to formulate control design specifications from system performance requirements with the end goal of achieving these performance requirements at the end of development cycle. A validated UAV model for flight control synthesis allows simple and straight forward techniques to validate closed-loop system performance. The presence of model uncertainty resulted from actual physical system approximation affects the robustness of designed controller performance as well as the validation methodology. Therefore it is important to relate the interplay between model uncertainty, model validation and control system performance robustness in closed-loop performance validation, which is a similar problem faced in model validation.

## 1.3 Integrated Framework

An integrated framework to flight control synthesis and validation merges different design and analysis tools with the linear and nonlinear simulation models that allows for an iterative controller laws design and validation environment. At the same time, the linear and nonlinear models used for controller design and validation are being updated as part of the development cycle. The parallel effort of redesigning and validating of the flight control laws and the models are used for controller synthesis and validation facilitate rapid controller design, analysis and implementation process with the latest updated models.

## 1.4 Research Outline: Objectives and Scope

### 1.4.1 Objective

The primary objectives of this thesis are to demonstrate and implement an integrated framework for synthesis and validation of flight controllers using a small UAV testbed. It combines theoretical design tools and experimental procedures.

### 1.4.2 Scope

The scope of the thesis is the development process of an integrated framework for synthesis and validation of UAV flight controller using a small commercial off-the-shelf radio-controlled airplane integrated with flight avionics system.

Nonlinear modeling of the UAV system is done using first principle theory in Matlab/Simulink environment with experiments carried out for obtaining physical model parameters. In the flight dynamics modeling, flight test system identification process is conducted to update and verify the lateral model developed used for flight control synthesis and validation. Parametric uncertainties due to the modeling process are modeled into the nonlinear simulation model developed. The uncertain nonlinear simulation model is further linearized to uncertain linear model for the purpose of flight control synthesis and analysis.

Flight control synthesis is carried out to design lateral-directional axis roll angle controller with the uncertain linear model to meet the design specifications. Both classical and modern control design approach are used for the controller synthesis. The controllers obtained are implemented on embedded flight computer system for controller testings.

Software and processor-in-the-loop testing environments are developed for the flight control development testing. The developed framework provides an incremental and systematic approach of testing the synthesized controllers before putting the controllers on the UAV for flight tests. With the developed integrated framework, the designed controller, model and model uncertainty developed are validated.

## 1.5 Research Contribution

The contributions of this thesis are as follows:

- Systematic procedures for parametric uncertainty modeling in nonlinear simulation models with realization of uncertain linear model.
- Approach for uncertain model simplification.
- Approach for nonlinear simulation model aerodynamic coefficients update using flight test parameter identification results.
- Integrated framework and environment for development of flight control synthesis and validation.

## 1.6 Organization of Dissertation

The disseration is organized as follows. The introduction, objective and scope of the research is given in Chapter 1. Chapter 2 develops the nonlinear simulation model of the experimental UAV system. Chapter 3 covers the flight test system identification experiments, system identification flight test procedures, parameter identification techniques and gives the results of the identification used to update the nonlinear simulation model. Chapter 4 describes the approach to uncertainty modeling for inclusion into the nonlinear simulation model. Procedures for performing linear uncertain model realization and analysis are also discussed. In Chapter 5, flight control synthesis and controller implementation on the embedded flight computer is presented. Chapter 6 provides model and flight control performance validation for the UAV system using both simulation tools and flight testing methods. The conclusion and future recommendations for the research are given in Chapter 7.

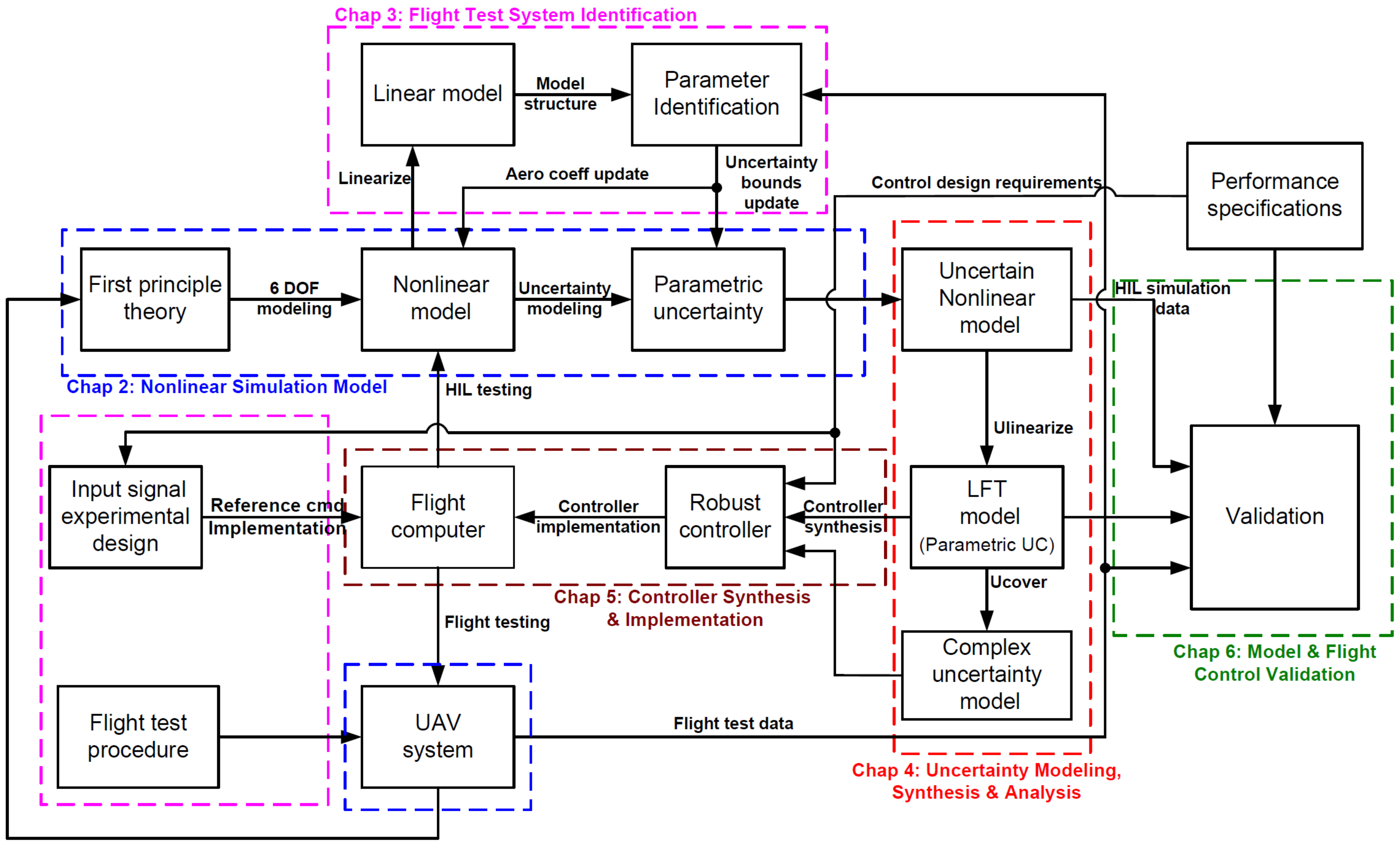
Chap 3: Flight Test System Identification
Linear model
Model structure
Parameter Identification
Linearize
Aero coeff update
Uncertainty bounds update
Control design requirements
Performance specifications
First principle theory
6 DOF modeling
Nonlinear model
Uncertainty modeling
Parametric uncertainty
Uncertain Nonlinear model
HIL simulation data
Chap 2: Nonlinear Simulation Model
HIL testing
Ulinearize
Validation
Input signal experimental design
Reference cmd Implementation
Flight computer
Controller implementation
Robust controller
Controller synthesis
LFT model (Parametric UC)
Ucover
Chap 5: Controller Synthesis & Implementation
Flight testing
Complex uncertainty model
Chap 6: Model & Flight Control Validation
Flight test procedure
UAV system
Flight test data
Chap 4: Uncertainty Modeling, Synthesis & Analysis

Figure 1.2: Overview of dissertation

# Chapter 2

# Small UAV Nonlinear Simulation Model

Aircraft fight dynamics models are used extensively for simulation analysis, flight control law algorithms implementation and extraction of low-order model for flight control synthesis. This has the benefits of lowering the cost and risk associated with design and operation of the aircraft system. Modeling, simulation analysis and flight testing of full-size aircraft are very well established and documented over the past few decades. However, limited literature is available regarding the detail modeling, simulation and analysis of small UAV systems [9]. It is expected that the use of high fidelity simulation model in small UAV systems development will bring similar benefits in lowering the cost and risk involved during the system development cycle.

For a simulation model to be useful, it should be able to predict the actual system response accurately. However, a mathematical model is just an approximation of the actual physical system. Hence there will be uncertainty in predicting the actual system response using the model developed. Therefore it is important to include model uncertainty in the simulation model. Uncertainty modeling is even more crucial in small UAV modeling since small UAV flight dynamics is less well understood than full-size aircraft.

This chapter describes the development of the nonlinear UAV simulation model from first principle using forces and moments equations. The major difficulty faced in the model development is in accurate determination of the model's physical parameters. Experiments conducted to obtain these physical parameters are covered. The nonlinear simulation model developed in this chapter provides the basic foundation for the integrated framework approach.

## 2.1 UAV Platform

### 2.1.1 Physical Geometry

The aircraft chosen for the research is a commercial off-the-shelf (COTS) Radio-Controlled (RC) plane *UltraStick 25E* (shown in Figure 2.1). The plane has a conventional horizontal and vertical tail with rudder and elevator control surfaces. The aircraft uses a symmetrical airfoil wing and has both aileron and flap control surfaces. All the control surfaces are actuated by *Hitec* servos. The propulsion system is made up of a 600 watts *E-Flite* electric outrunner motor driving an *APC* 12 x 6 propeller. A summary of important physical parameters is provided in Table 2.1.

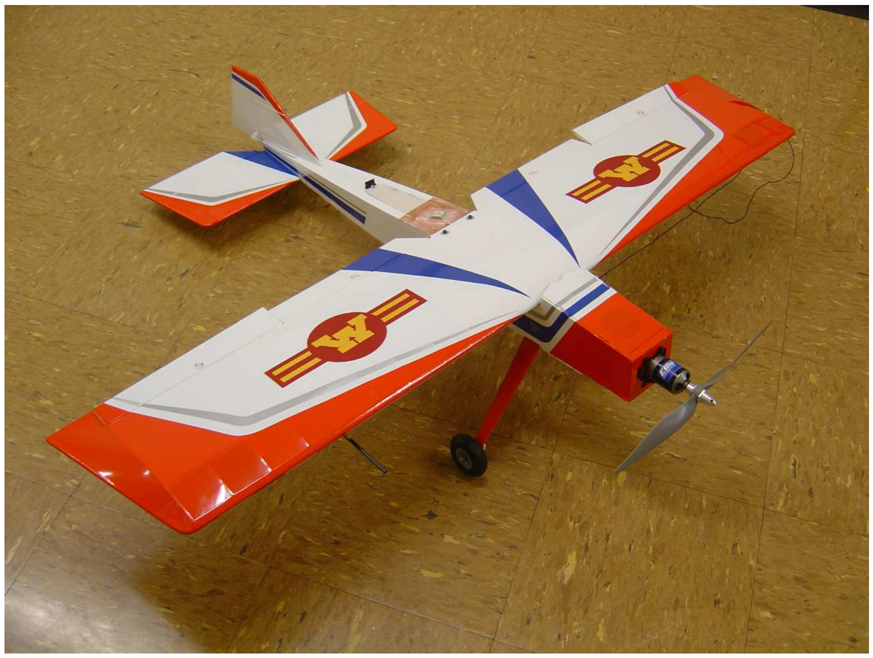

Figure 2.1: Research testbed: Ultra Stick 25E RC plane

| Parameter | Description | Value and Units |
|---|---|---|
| $A$ | wing reference area | $0.32\,m^2$ |
| $b$ | wing span | $1.2\,m$ |
| $\bar{c}$ | wing chord | $0.3\,m$ |
| $m$ | gross take off weight | $1.9\,kg$ |

Table 2.1: Summary of important aircraft geometry

### 2.1.2 Flight Avionics System

The RC plane is instrumented with a suite of flight avionics for the flight control development research. Figure 2.2 shows the architecture of the flight avionics system and Table 2.2 gives a listing of the individual component in the avionics system. The IMU/GPS sensor provides the following measurement data:

- Angular rates: $p$ $(deg/s)$, $q$ $(deg/s)$ and $r$ $(deg/s)$
- Accelerations: $a_x$ $(g)$, $a_y$ $(g)$ and $a_z$ $(g)$
- Magnetic fields: $H_x$ $(gauss)$, $H_y$ $(gauss)$ and $H_z$ $(gauss)$
- Airspeed and barometric altitude: $V_s$ $(m/s)$ and $h$ $(m)$
- GPS velocities (ENU format) and positions: $v_e$ $(cm/s)$ , $v_n$ $(cm/s)$, $v_u$ $(cm/s)$ and $p_x$ $(10^{-7}deg)$, $p_y$ $(10^{-7}deg)$, $p_z$ $(m)$.

The flight computer runs the *eCos* (embedded configurable operating system) [10] real-time operating system. Sensor data are acquired into the flight computer and attitude determination is done using a 7 states Kalman Filter [11]. At the same time, the flight computer also executes flight control algorithms and outputs Pulse-Width Modulated (PWM) signals to control the servo actuators and sends telemetry data information to the data modem and datalogger through serial communication port for flight test data collection. Dual channels datalogger is used to record both raw sensor data (at 50 Hz) and flight control data (at 20 Hz). The flight test data is also sent to ground control station for real-time health monitoring during flight testing. A failsafe switch board is used as a safety precaution to switch flight computer commands back to manual pilot commands if necessary.

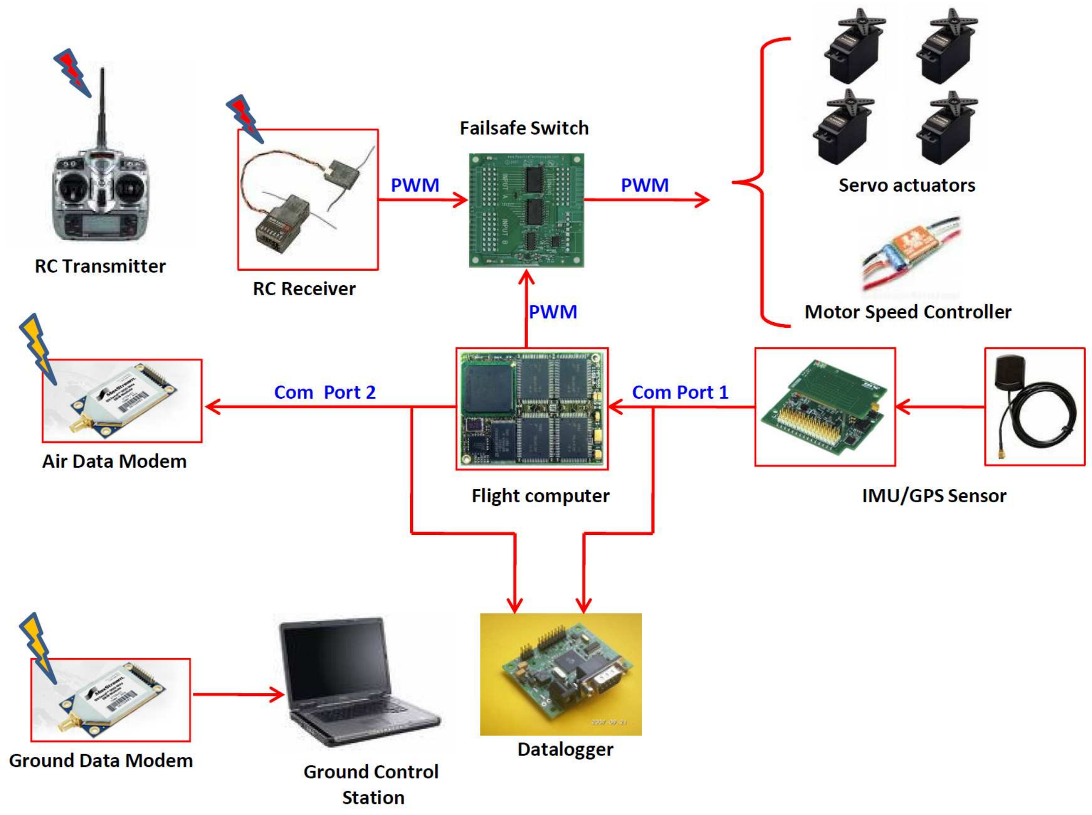

Figure 2.2: Flight avionics system architecture layout

| Component | Module |
|---|---|
| Flight computer | Phytec MPC 555 microcontroller [12] |
| IMU/GPS sensor | Crossbow Micronav sensor [13] |
| Data Modem | Maxstream 900 Mhz modem [14] |
| RC telemetry | Spektrum DX-7 2.4 Ghz RC system [15] |
| Failsafe switch | RxMux board [16] |
| Datalogger | Antilog RS232 serial datalogger [17] |

Table 2.2: Components in flight avionics system

## 2.2 Nonlinear Simulation Model

This section describes development of the nonlinear UAV flight dynamics model using Matlab/Simulink environment. Simulink modeling of the UAV model is adapted from Aerosonde UAV Simulink model provided by AeroSim Blockset from Unmanned Dynamics [18]. The AeroSim Blockset is a Matlab/Simulink library block that provides standard aircraft model components for rapid development of nonlinear 6-DOF aircraft dynamic models. Beside aircraft dynamics model blocks, the blockset also provides environment and earth models. Figure 2.3 shows a simplified layout of the nonlinear aircraft model block diagram from AeroSim Blockset [19].

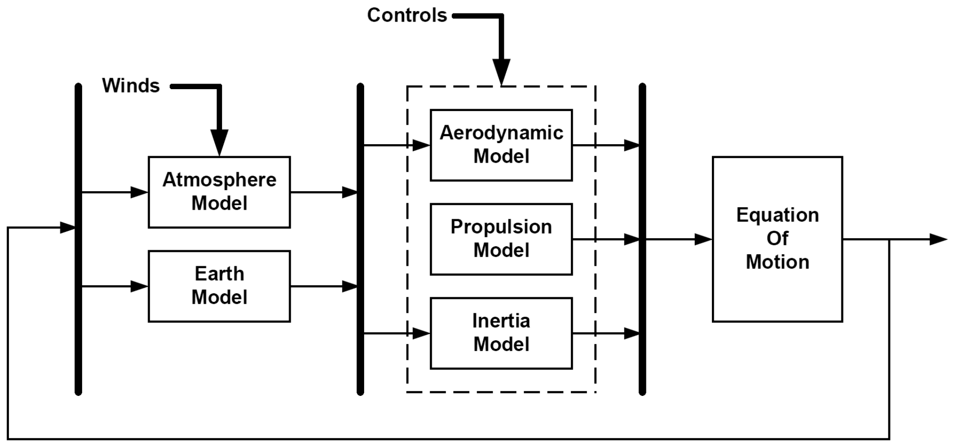

Figure 2.3: Simplified layout of Aerosim nonlinear 6-DOF aircraft model

Modification to the aerodynamics, propulsion and inertia Aerosonde UAV Simulink blocks had been performed and experiments have to be carried out to get the required physical aircraft parameters. The equation of motion, earth and atmosphere Simulink blocks are not modified since they are independent of the aircraft platform used. Actuator dynamics are also modeled into the simulation model to account for the actuator characteristics.

### 2.2.1 Aerodynamic Model

The dynamic model of an aircraft is commonly described by a six degrees of freedom equations which are derived from the $X$, $Y$ and $Z$ forces and $L$, $M$ and $N$ moment equations

[20]. Figure 2.4 shows the forces and moments description in the aircraft body axis.

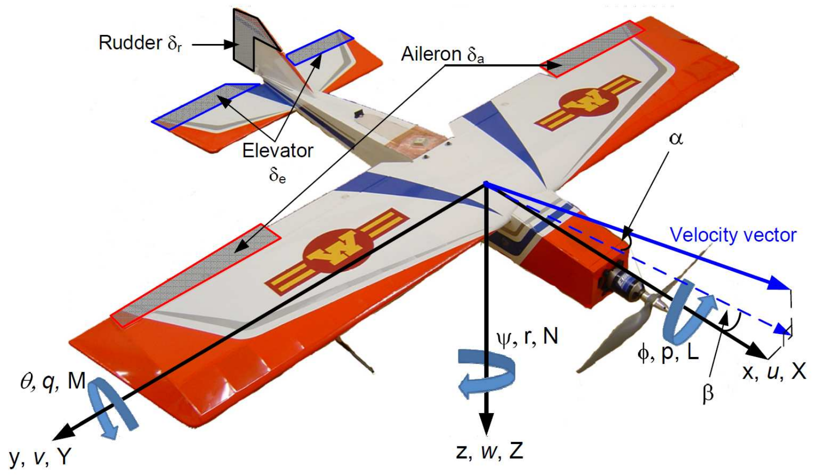

Figure 2.4: Forces and moments in aircraft body axis

### 2.2.1.1 Force Equations

The summation of the forces in body $x$, $y$ and $z$ axis gives linear velocity state equations [20]:

$$\begin{aligned}\dot{u} &= rv - qw + \frac{\bar{q}S}{m}C_X - gsin\theta + \frac{T}{m}\\ \dot{v} &= pw - ru + \frac{\bar{q}S}{m}C_Y - gcos\theta sin\phi\\ \dot{w} &= qu - pv + \frac{\bar{q}S}{m}C_Z - gcos\theta cos\phi\end{aligned}$$

where $u$ $(m/s)$, $v$ $(m/s)$ and $w$ $(m/s)$ are the body axis linear velocities, $p$ $(rad/s)$, $q$ $(rad/s)$ and $r$ $(rad/s)$ are the body axis angular rates, $\phi$ $(rad)$, $\theta$ $(rad)$ and $\psi$ $(rad)$ are the body attitude angles and $\bar{q}$ $(Pa)$ is the dynamic pressure. $C_X$, $C_Y$ and $C_Z$ are the aerodynamic force coefficients and are given by the following relationships:

$$\begin{aligned}C_X &= C_L sin\alpha - C_D cos\alpha\\ C_Z &= -C_D sin\alpha - C_L cos\alpha\\ C_Y &= C_{Y_\beta}\beta + C_{Y_{\delta r}}\delta r + \frac{b}{2V_a}(C_{Y_p}p + C_{Y_r}r) \qquad (2.1)\end{aligned}$$

where $\alpha$ $(rad)$ and $\beta$ $(rad)$ are angle of attack and sideslip angle of the aircraft in the wind axis. The forces in the body $x$, $y$ and $z$ axis are given by:

$$\begin{aligned} X &= \bar{q}SC_X \\ Y &= \bar{q}SC_Y \\ Z &= \bar{q}SC_Z \end{aligned}$$

The lift $(C_L)$ and drag $(C_D)$ coefficients are functions of the non-dimensional coefficients given by:

$$\begin{aligned} C_L &= C_{L_0} + C_{L_\alpha}\alpha + C_{L_{\delta e}}\delta e + \frac{c}{2V_a}(C_{L_{\dot{\alpha}}}\dot{\alpha} + C_{L_q}q) \\ C_D &= C_{D_0} + C_{D_{\delta e}}\delta e + C_{D_{\delta r}}\delta r + \frac{(C_L - C_{L_{min}})}{\pi.e.AR} \end{aligned}$$

In this case, small perturbation assumption is made and only linear terms are retained in the lift and drag coefficients and higher order terms such as $\alpha^2$, $\alpha^3$ etc are neglected.

#### 2.2.1.2 Moment Equations

Taking a moment about the aerodynamics center of the aircraft, the angular rate equations are given by:

$$\dot{p} - \frac{I_{xz}}{I_{xx}}\dot{r} = \frac{\bar{q}Sb}{I_{xx}}c_l - \frac{I_{zz} - I_{yy}}{I_{xx}}qr + \frac{I_{xz}}{I_{xx}}qp \tag{2.2}$$

$$\dot{q} = \frac{\bar{q}S\bar{c}}{I_{yy}}c_m - \frac{I_{xx} - I_{zz}}{I_{yy}}pr - \frac{I_{xz}}{I_{yy}}(p^2 - r^2) + \frac{I_p}{I_{yy}}\omega_p r \tag{2.3}$$

$$\dot{r} - \frac{I_{xz}}{I_{zz}}\dot{p} = \frac{\bar{q}Sb}{I_{zz}}c_n - \frac{I_{yy} - I_{xx}}{I_{zz}}pq - \frac{I_{xz}}{I_{zz}}qr - \frac{I_p}{I_{zz}}\omega_p q \tag{2.4}$$

where $\omega_p$ $(rad/s)$ is the propeller rotation speed, $I_{xx}$, $I_{yy}$, $I_{zz}$, $I_{xz}$ and $I_p$ are the moment of inertia coefficients for the aircraft and propulsion system respectively in $kgm^2$ and $c_l$, $c_m$

and $c_n$ are the non-dimensional moment coefficients. These coefficients are given by:

$$c_l = c_{l_\beta}\beta + c_{l_{\delta a}}\delta a + c_{l_{\delta r}}\delta r + \frac{b}{2V_a}(c_{l_p}p + c_{l_r}r) \tag{2.5}$$

$$c_m = c_{m_0} + c_{m_\alpha}\alpha + c_{m_{\delta e}}\delta e + \frac{\bar{c}}{2V_a}(c_{m_{\dot\alpha}}\dot\alpha + c_{m_q}q) \tag{2.6}$$

$$c_n = c_{n_\beta}\beta + c_{n_{\delta a}}\delta a + c_{n_{\delta r}}\delta r + \frac{b}{2V_a}(c_{n_p}p + c_{n_r}r) \tag{2.7}$$

The moments about the body $x$, $y$ and $z$ axis are given by:

$$\begin{aligned} L &= \bar{q}Sbc_l \\ M &= \bar{q}Sbc_m \\ N &= \bar{q}Sbc_n \end{aligned}$$

#### 2.2.1.3 Kinematic Equations

The kinematics of the aircraft rotation motion relating the body angular rates $p$, $q$ and $r$, Euler angles $\phi$, $\theta$ and $\psi$ and aerodynamics angles $\alpha$, $\beta$ and $\gamma$ are given by:

$$\begin{aligned} \dot\phi &= p + tan\theta(qsin\phi + rcos\phi) \\ \dot\theta &= qcos\phi - rsin\phi \\ \dot\psi &= \frac{qsin\phi + rcos\phi}{cos\theta} \\ \theta &= \gamma + \alpha cos\phi + \beta sin\phi \end{aligned}$$

#### 2.2.1.4 Determination of Aerodynamic Coefficients

The list of aerodynamic coefficients required to model the Ultrastick UAV using the modified AeroSim Aerosonde UAV nonlinear simulation model is summarized in Table 2.3. These coefficients can be obtained from wind tunnel testing [21], numerical computational method [22] or flight test parameter identification. The approach used to determine these aerodynamic coefficients is to first approximate these coefficient values using simulator parameters tuning approach with some of the initial coefficient values set to values from relevant work done by [23]. Subsequently, these coefficient values are refined using flight test parameter identification.

| Lift Force | Drag Force | Side Force | Roll moment | Pitch moment | Yaw moment |
|---|---|---|---|---|---|
| $C_{L_0}$ | $C_{D_0}$ | $C_{Y_\beta}$ | $c_{l_\beta}$ | $c_{m_0}$ | $c_{n_\beta}$ |
| $C_{L_\alpha}$ | $C_{D_{\delta e}}$ | $C_{Y_{\delta r}}$ | $c_{l_{\delta r}}$ | $c_{m_\alpha}$ | $c_{n_{\delta r}}$ |
| $C_{L_{\dot\alpha}}$ | $C_{D_{\delta r}}$ | $C_{Y_p}$ | $c_{l_p}$ | $c_{m_{\delta e}}$ | $c_{n_p}$ |
| $C_{L_q}$ |  | $C_{Y_r}$ | $c_{l_r}$ | $c_{m_{\dot\alpha}}$ | $c_{n_r}$ |
| $C_{L_{min}}$ |  |  | $c_{l_{\delta a}}$ | $c_{m_q}$ |  |

Table 2.3: Aerodynamic coefficients required for Ultrastick UAV modeling

**Simulator Parameter Tuning**

In simulator parameter tuning, estimate of aerodynamic coefficients are obtained using simulator flying by RC pilots using an iterative tuning process. Figure 2.5 shows the details of the tuning process. The joystick control box used in the simulator flying is the same radio control box used for actual flight test. Control signals are input to the nonlinear Simulink model that contains the initial guess aerodynamics coefficients from [23]. The outputs from the simulation model are the state responses of the vehicle which are used to drive FlightGear [24] simulator. The FlightGear simulator provides a visualization for the aircraft motions. Figure 2.6 shows the setup of simulator parameter tuning experiment.

Two RC pilots who have been flying the actual UAVs were tasked to fly with the simulator setup using different flight maneuvers. Based on their flight handling experiences with the actual UAV, the aerodynamic coefficients in the simulation model were tuned iteratively until they felt that the simulator model had similar handling qualities as the actual UAV flight. Appendix Table A.1 contains the aerodynamic coefficients that were obtained from the simulator tuning. These coefficients will be used as initial estimates for flight test parameter identification.

### 2.2.2 Inertia Model

The inertia model contains physical geometric information of the aircraft mass, center of gravity and moment of inertia coefficients. The aircraft moment of inertia is described by

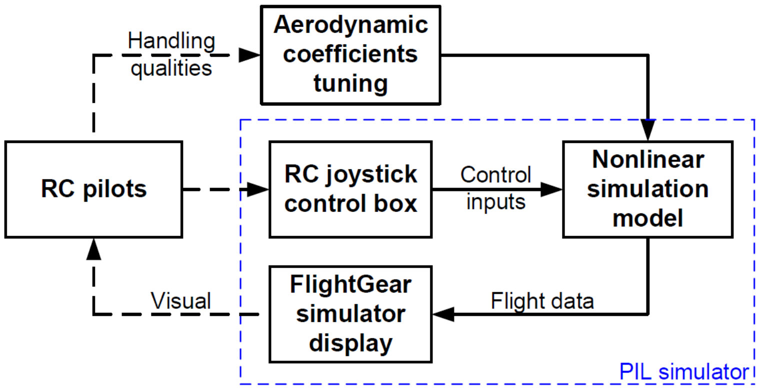

Figure 2.5: Simulator parameter tuning process

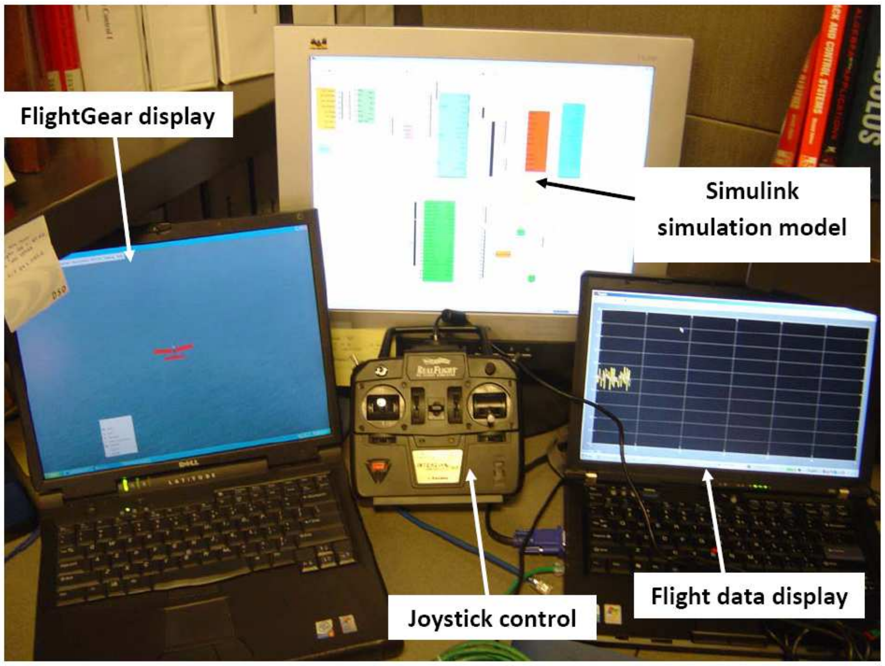

Figure 2.6: Setup for simulator parameter tuning

the moment of inertia matrix $I$:

$$I = \begin{bmatrix} I_{xx} & -I_{xy} & -I_{xz} \\ -I_{yx} & I_{yy} & -I_{yz} \\ -I_{zx} & -I_{zy} & I_{zz} \end{bmatrix}$$

The Ultrastick UAV is assumed to be symmetrical about the $xz$ plane. This simplifies the inertia matrix with $I_{xy} = I_{yx} = I_{xz} = I_{zy} = 0$. Hence the inertia matrix becomes:

$$I = \begin{bmatrix} I_{xx} & 0 & -I_{xz} \\ 0 & I_{yy} & 0 \\ -I_{zx} & 0 & I_{zz} \end{bmatrix}$$

Beside the aircraft moment of inertia matrix, propulsion system moment of inertia coefficient is required. These moment of inertia coefficients are determined using pendulum method described in Appendix A.2. The nominal, lower and upper bound values for the moment of inertia of the aircraft and the propulsion system obtained from the experiments are given in Appendix Table A.2.

### 2.2.3 Propulsion Model

The propulsion system models the interaction between electric motor and propeller dynamics. The rotation speed of propeller, $\omega_p$, is used to describe the dynamics of the propulsion system. Small UAVs (with propeller propulsion system) flight dynamics are sensitive to the propulsion system dynamics unlike the full-size aircraft. This is due to the large torque from the propulsion system coupling with the aircraft rigid body dynamics since the small UAV system is being propelled by a larger propeller relative to its aircraft size. Therefore the moment generated by the propeller is added to the total moment of the aircraft in the simulation model. Applying the conservation of angular momentum, the propulsion dynamics is given by:

$$(I_{motor} + I_{propeller})\dot{\omega}_p = T_{motor} - T_{propeller}$$

where:

$I_{motor}$ = moment of inertia of rotating motor body ($kgm^2$)

$I_{propeller}$ = moment of inertia of propeller with spinner hub attachment ($kgm^2$)

$T_{motor}$ = Output torque at motor shaft ($Nm$)

$T_{propeller}$ = Torque generated by propeller ($Nm$)

The moment of inertia for rotating motor body, $I_{motor}$, is included because the motor used is an outrunner motor in which the major part of the motor mass is rotating. This has a significant contribution to the total moment of inertia for the propulsion system, $I_p$ ($I_p = I_{motor} + I_{propeller}$).

#### 2.2.3.1 Propulsion Motor

The propulsion motor used is *E-flite Power 25 BL Outrunner Motor* [25]. The motor performance data is obtained from a commercial software, MotorCalc [26], since it is not available from the manufacturer. Figure 2.7 shows the plot for the relationship between throttle stick input ($\delta_T$) and output power at the motor shaft ($P_o$).

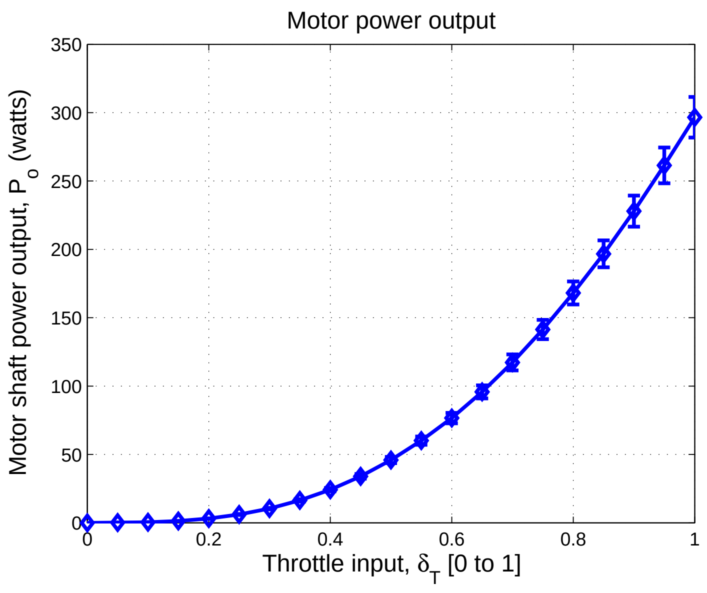

Figure 2.7: Motor power output

The motor shaft torque, $T_{motor}$ $(Nm)$, generated from the motor shaft output power $P_o$ is given by:

$$T_{motor} = \frac{P_o}{\omega_p}$$

#### 2.2.3.2 Propeller Characteristics

The thrust to propel the aircraft forward is generated by the rotating propeller using the torque generated at motor output shaft. The propeller rotation speed depends on both the input torque available and the speed of air flowing into the propeller disk. The propeller performance is generally characterized by 3 parameters [27]:

- Advance ratio, $J$, given by:
$$J = \frac{\pi V_a}{\omega_p R}$$
- Coefficient of Thrust, $C_T$, given by
$$C_T = \frac{F_p \pi^2}{4\rho R^4 {\omega_p}^2}$$
- Coefficient of Power, $C_P$, given by
$$C_P = \frac{T_p \pi^3}{4\rho R^5 {\omega_p}^2}$$

where $R$ $(m)$ is the diameter of the propeller, $F_p$ $(N)$ is the propeller thrust, $T_p$ $(Nm)$ is the propeller torque and $\rho$ $(kgm^{-3})$ is the air density.

The performance data of the propeller used is not available from manufacturer. Therefore, approximation is made on the propeller performance data based on experimental result published by [28] on an APC 12 x 8 propeller. In [28], the propulsion system thrust and torque generated were measured using a force-moment sensor in a wind tunnel with different propeller rotation speed and inflow airspeed. The coefficient of thrust and power obtained were plotted against advance ratio as shown in Figure 2.8. These data (Appendix Table A.3) are used as lookup tables in the nonlinear simulation model. This provides the propeller thrust $(F_p)$ and moment $(T_p)$ at different advance ratios condition during the simulation.

#### 2.2.3.3 Propulsion System Verification

The propulsion system model developed and implemented in the simulation model is verified using MotorCalc software [26]. The software program allows the specific motor, speed controller and propeller used in the Ultrastick UAV to be selected from the database so

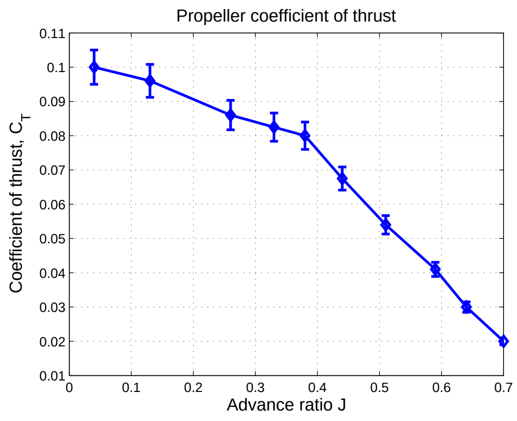

(a) Coefficient of thrust

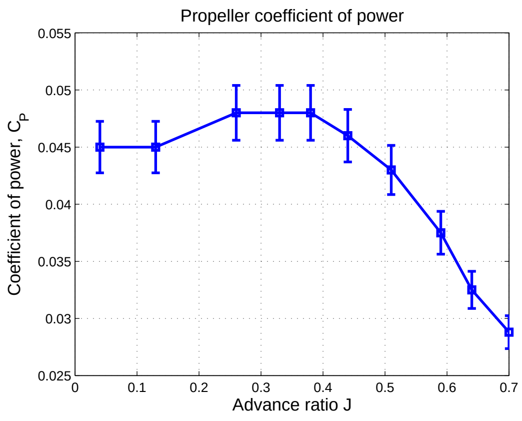

(b) Coefficient of power

Figure 2.8: Propeller performance for APC 12 x 8 propeller

that static and in-flight aircraft performance can be computed. A static flight condition, with zero airspeed, is chosen for the verification. In the verification, the throttle input to the simulation model and MotorCalc software are incrementally increased from 0 to 1 with a 0.1 step size. The propeller thrust and RPM obtained from the two system are compared. Figure 2.9 shows the comparison plots of propeller thrust and RPM. The plots show that the implemented propulsion system simulation model output responses have a close matching with the MotorCalc outputs. This verifies the propulsion system simulation model developed and the data used in our model implementation are realistic since it is able to match the results obtained from the commercial software.

### 2.2.4 Actuator Model

The UAV control surfaces are driven by *Hitec S*3108 micro servos using Pulse-Width Modulation (PWM) signal operating at 45 Hz. The servo rotation rate is 500 $deg/s$ at no load condition. The time delay for the servo actuator dynamics is approximated using a single period of PWM signal operating at 45 Hz frequency. This gives a time delay of 22 ms for the actuator delay. The actuators rotation angle saturation limits are limited to the maximum mechanical deflection angles of the control surfaces. These limits, given in Appendix Table A.4, are measured from the Ultrastick UAV.

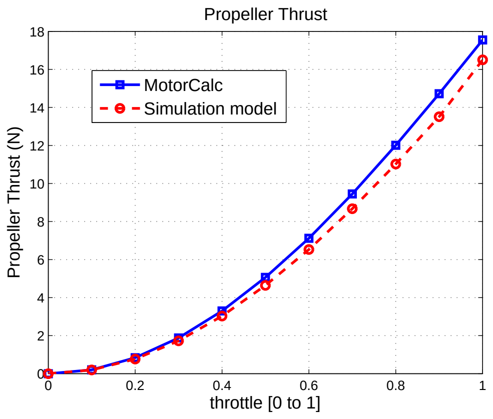

(a) Propeller thrust

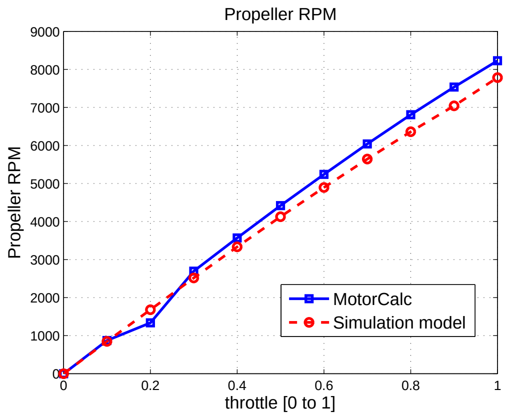

(b) Propeller RPM

Figure 2.9: Propulsion system verification at static flight condition

Chapter 3

# Flight Test System Identification

Flight test system identification is an important process used to develop, improve model fidelity and validate simulation models. The scope involved includes model parameters determination, validation and design of suitable identification experiments for collecting relevant inputs and outputs data. Aircraft parameters identification is mainly divided into two major approaches, time domain and frequency domain identification method. Both these two parameter identification methods have been widely used in many aircraft platform development programs [29–32]. The time domain parameter estimation method is used in this research since it is physically more intuitive and straight forward as the aircraft dynamics are mostly represented using time domain state-space models.

Flight test parameter identification is used to update aerodynamics coefficients in the nonlinear simulation model obtained from the simulator parameter tuning in Chapter 2. This chapter describes the approach and procedures used to update the aerodynamic coefficients in the nonlinear simulation model based on flight test data. This involves stability and control derivative parameters estimation of state-space model and converting these derivatives to dimensionless form. Figure 3.1 outlines the procedures involved.

## 3.1 Model Structure for Parameters Identification

The choice of an appropriate model structure is crucial for successful system identification. This must be made based on the understanding of system identification procedures,

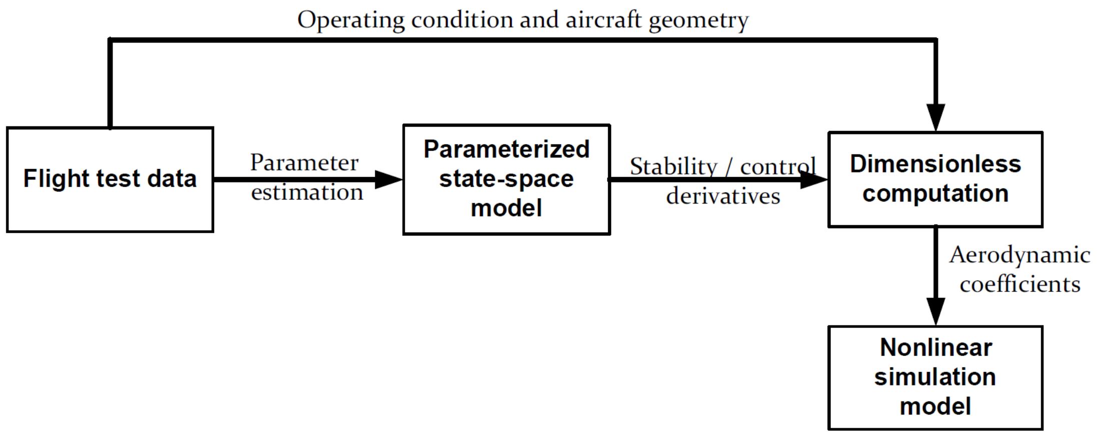
Operating condition and aircraft geometry
Flight test data
Parameter estimation
Parameterized state-space model
Stability / control derivatives
Dimensionless computation
Aerodynamic coefficients
Nonlinear simulation model

Figure 3.1: Procedures involved to update aerodynamic coefficients

knowledge of physical system to be identified and the intended use of the model [33]. The approach taken in this thesis is not to search for the "best" model structure (which is subjective) for the system identification, but to use a model structure that is suitable for the intended application with an understanding of the advantages and disadvantages associated with the selected model structure.

The model structure selected is a linear state-space model that is parameterized by physically meaningful stability and control derivatives. The reason for using this model structure is that the parameters in the state-space model are related to the nonlinear simulation model aerodynamic coefficients. Model parameter estimation from flight test data provides an update to the aerodynamic coefficients in the nonlinear simulation model used in the integrated framework. Hence the selection of the fixed model structure is used for the system identification. Furthermore, using a linear model structure in the system identification simplifies the identification problem as compared to using a nonlinear model structure even though the aerodynamic coefficients can be obtained directly with nonlinear model identification. Identifiability of the aerodynamic coefficients is closely related to the observability of each aerodynamic coefficient from the flight test data collected. Therefore, using a nonlinear model for system identification would require a more unique flight test input excitations and flight maneuvers which can be difficult for the RC pilots to execute.

### 3.1.1 Linear Decoupled Model

It is a common practice to decouple the linearized model into longitudinal and lateral-directional modes to simplify the problem in most of the flight dynamics and control analysis. The assumption made for decoupling the linearized model is that the cross-coupling effect between the two modes is negligible. This assumption is made for the Ultrastick UAV platform for the following reasons:

- It is designed with conventional aileron, rudder and elevator control surfaces that do not give significant cross-coupling control effects between the lateral-directional and longitudinal modes.
- The aircraft is symmetrical about the $xz$ plane in which the inertia cross-coupling (in $xy$ and $xz$ axes) resulting to cross-coupling effects between the lateral-directional and longitudinal modes is minimum.
- Flight test data collected from open loop UAV flights with individual control surface excitations shows no significant coupling between these longitudinal and lateral-directional modes.

To extract a linear decoupled model from the nonlinear simulation model, the nonlinear model is first linearized about trim operating point. This gives a linear model that contains the longitudinal, lateral-directional and other coupling modes. Next, the linearized model is decoupled into longitudinal and lateral-directional modes by extracting the states that are relevant in each of the modes. Figure 3.2 shows the procedures for deriving linear decoupled models from the nonlinear simulation model.

#### 3.1.1.1 Linearization of Nonlinear Model

Linear models of the Ultrastick UAV are obtained through numerical linearization of the nonlinear simulation model at trim operating point. The trim operating point is obtained from trimming the aircraft at a desired flight operating envelop. Table 3.1 gives the desired flight operating envelope for the UAV. The flight operating envelope is chosen based on the open loop flight test data with the Ultrastick UAV flying in a cruise flight condition. The

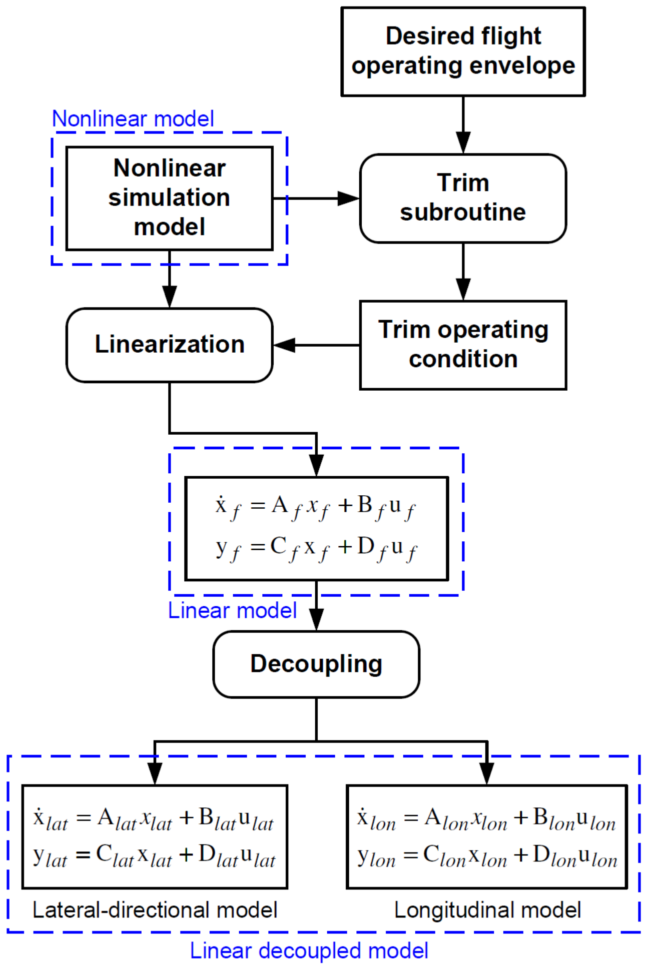
Desired flight operating envelope
Nonlinear model
Nonlinear simulation model
Trim subroutine
Linearization
Trim operating condition
$\dot{x}_f = A_f x_f + B_f u_f$
$y_f = C_f x_f + D_f u_f$
Linear model
Decoupling
$\dot{x}_{lat} = A_{lat} x_{lat} + B_{lat} u_{lat}$
$y_{lat} = C_{lat} x_{lat} + D_{lat} u_{lat}$
Lateral-directional model
$\dot{x}_{lon} = A_{lon} x_{lon} + B_{lon} u_{lon}$
$y_{lon} = C_{lon} x_{lon} + D_{lon} u_{lon}$
Longitudinal model
Linear decoupled model

Figure 3.2: Procedures for deriving linear decoupled models

trim operating point obtained from trimming at desired flight operating envelope is given in Appendix Table B.1. The linearized state-space model obtained from the numerical linearization is given by:

$$\begin{aligned} \dot{\mathbf{x}}_f &= \mathbf{A}_f \mathbf{x}_f + \mathbf{B}_f \mathbf{u}_f \\ \mathbf{y}_f &= \mathbf{C}_f \mathbf{x}_f + \mathbf{D}_f \mathbf{u}_f \end{aligned} \tag{3.1}$$

$\mathbf{x}_f$ is the state vector given by $[u \;\; v \;\; w \;\; \phi \;\; \theta \;\; \psi \;\; p \;\; q \;\; r \;\; h \;\; \omega]^T$ where $(u,\, v,\, w)$ are the body axis velocities in $(m/s)$, $(\phi,\, \theta,\, \psi)$ are the Euler angles in $(rad)$, $(p,\, q,\, r)$ are body axis angular rates in $(rad/s)$, $h$ is the altitude in $(m)$ and $\omega_p$ is the propeller rotation speed in $(rad/s)$. $\mathbf{u}_f$ is the control input vector consists of aileron, elevator, throttle and rudder control inputs in $(rad)$ given by $[\delta_e \;\; \delta_a \;\; \delta_T \; \delta_r]^T$. The output vector $\mathbf{y}_f$ is $[V_a \;\; \beta \;\; \alpha \;\; \phi \;\; \theta \;\; \psi \;\; h]^T$ where $V_a$ is the airspeed in $(m/s)$, $\beta$ is the sideslip angle in $(rad)$ and $\alpha$ is angle of attack in $(rad)$.

| Airspeed (m/s) | Altitude (m) | Throttle (%) |
|---|---|---|
| $16 \sim 18$ | $90 \sim 110$ | $45 \sim 60$ |

Table 3.1: Desired flight operating envelope

The details of $\mathbf{A}_f$, $\mathbf{B}_f$, $\mathbf{C}_f$ and $\mathbf{D}_f$ matrices obtained are given in Appendix B.2. The output variables $V_a$, $\beta$ and $\alpha$ are related to the body axis velocity $u$, $v$ and $w$ with the following relationships:

$$\alpha = \tan^{-1}\left(\frac{w}{u}\right) \tag{3.2}$$

$$\beta = \sin^{-1}\left(\frac{v}{V_a}\right) \tag{3.3}$$

$$V_a = \sqrt{u^2 + v^2 + w^2} \tag{3.4}$$

Doublet signals are applied to the elevator and rudder control input (Figure 3.3(f)) to the nonlinear simulation model and the linearized model obtained. This is to compare the matching of the linear model obtained with the nonlinear simulation model. Figure 3.3 shows the time history comparisons of the airspeed, AOA, roll angle, pitch angle and sideslip angle output responses between the linear model obtained and the nonlinear simulation model. All the output responses from the linear and nonlinear model have a good match. This shows that the linear model obtained represents the nonlinear simulation model well at this given trim operating point.

#### 3.1.1.2 Decoupling of Linearized Model

The longitudinal and lateral model of the UAV are obtained by decoupling the full linear model in Equation 3.1 through extracting control and stability derivatives from the full linear model that are relevant to each of the mode. The longitudinal model comprises of the body axis x and z direction velocities ($u$, $w$), pitch angular rate $q$, pitch angle $\theta$,

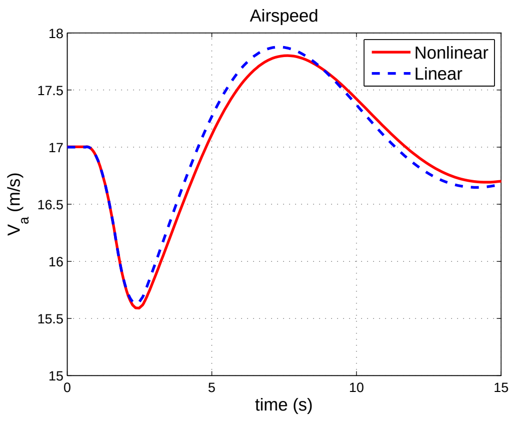

(a) Airspeed

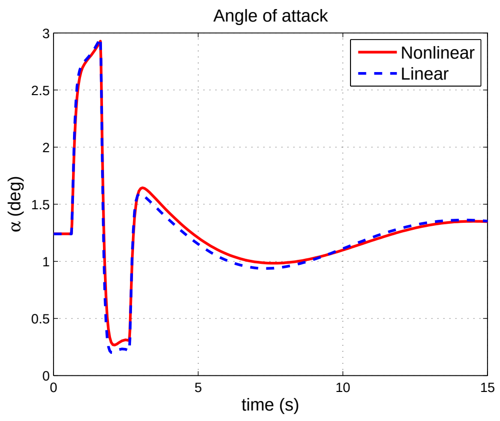

(b) Angle of attack

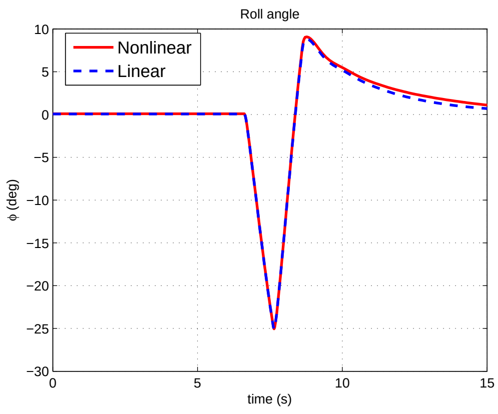

(c) Roll angle

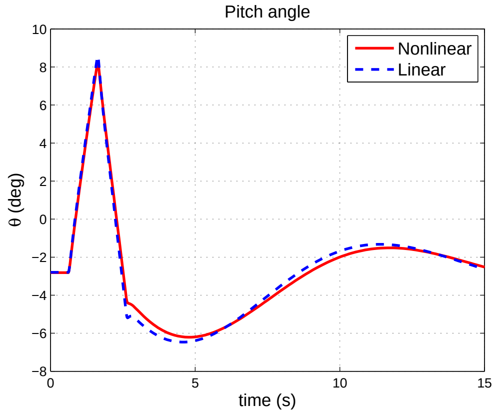

(d) Pitch angle

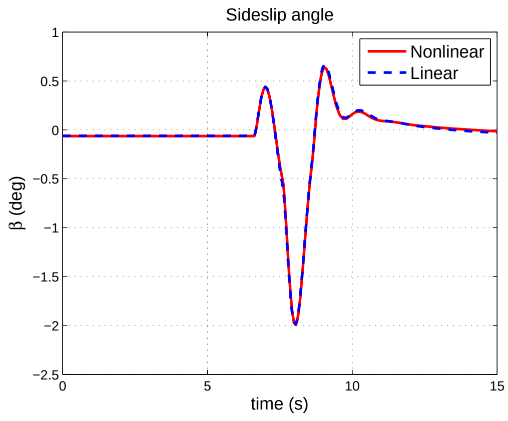

(e) Sideslip angle

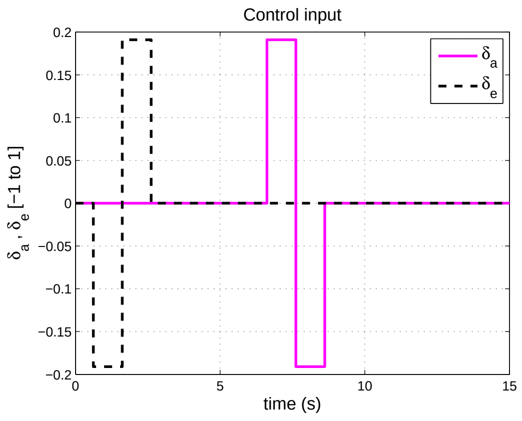

(f) Control input

Figure 3.3: Comparison of linear and nonlinear model output responses

altitude $h$ and propeller angular rotation $\omega_p$ state. Control inputs for the longitudinal model are elevator ($\delta_e$) and throttle ($\delta_T$) control. The measurement output variables for the longitudinal model are airspeed $V_a$, angle of attack $\alpha$, pitch rate $q$, pitch angle $\theta$ and altitude $h$. Equation 3.5 gives the state-space description for the longitudinal model.

$$\begin{aligned}
\dot{\mathbf{x}}_{lon} &= \mathbf{A}_{lon}\mathbf{x}_{lon} + \mathbf{B}_{lon}\mathbf{u}_{lon} \\
\mathbf{y}_{lon} &= \mathbf{C}_{lon}\mathbf{x}_{lon} + \mathbf{D}_{lon}\mathbf{u}_{lon} \\
where & \\
\mathbf{x}_{lon} &= [\begin{array}{cccccc} u & w & q & \theta & h & \omega \end{array}]^T \\
\mathbf{u}_{lon} &= [\begin{array}{cc} \delta_e & \delta_T \end{array}]^T \\
\mathbf{y}_{lon} &= [\begin{array}{ccccc} V_a & \alpha & q & \theta & h \end{array}]^T
\end{aligned} \tag{3.5}$$

The lateral model comprises of the body axis y direction velocity $v$, roll and yaw angular rate ($p$, $r$) and roll and yaw angle ($\phi$, $\psi$). Control inputs for the lateral model are aileron ($\delta_a$) and rudder ($\delta_r$) control. The measurement output variables for the lateral model are sideslip angle $\beta$, roll and yaw angular rate ($p$, $r$), roll and yaw angle ($\phi$, $\psi$). The lateral state-space model is given in Equation 3.6. The details of the matrices in the longitudinal and lateral model are given in Appendix B.3.

$$\begin{aligned}
\dot{\mathbf{x}}_{lat} &= \mathbf{A}_{lat}\mathbf{x}_{lat} + \mathbf{B}_{lat}\mathbf{u}_{lat} \\
\mathbf{y}_{lat} &= \mathbf{C}_{lat}\mathbf{x}_{lat} + \mathbf{D}_{lat}\mathbf{u}_{lat} \\
where & \\
\mathbf{x}_{lat} &= [\begin{array}{ccccc} v & p & r & \phi & \psi \end{array}]^T \\
\mathbf{u}_{lat} &= [\begin{array}{cc} \delta_a & \delta_r \end{array}]^T \\
\mathbf{y}_{lat} &= [\begin{array}{ccccc} \beta & p & r & \phi & \psi \end{array}]^T
\end{aligned} \tag{3.6}$$

Elevator control input ($\delta_e$ in Figure 3.4(f)) is applied to the linear decoupled longitudinal model in Equation 3.5 to obtain airspeed ($V_a$), angle of attack ($\alpha$) and pitch angle ($\theta$) output responses while aileron control input ($\delta_a$ in Figure 3.4(f)) is applied to the linear decoupled lateral model in Equation 3.6 to obtain roll ($\phi$) and yaw angle ($\psi$) output responses. The collective linear decoupled model output responses ($V_a$, $\alpha$, $\theta$, $\phi$, $\psi$) from the longitudinal and lateral models are compared with the full linear model in Equation 3.1 with the same elevator and aileron control input in Figure 3.4(f). Figure 3.4 shows the comparison plots between the full linear model and the decoupled models. The plots show that the decoupled linear models (longitudinal and lateral model) output responses match the full linear model well. This shows that the full linear model can be decoupled into longitudinal and lateral model and still provide similar output responses without degradation due to decoupling. This validates the assumption that the cross-coupling effect between the longitudinal and lateral-directional modes is negligible and the full linear model can be decoupled into these two modes.

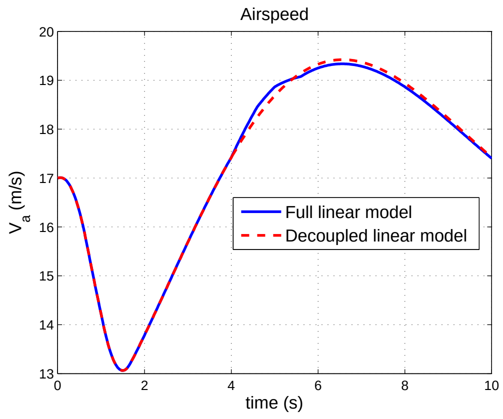

(a) Airspeed

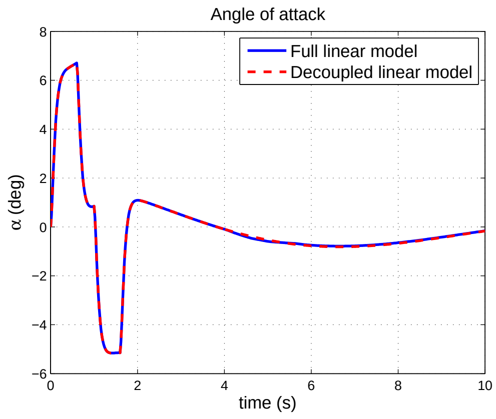

(b) Angle of attack

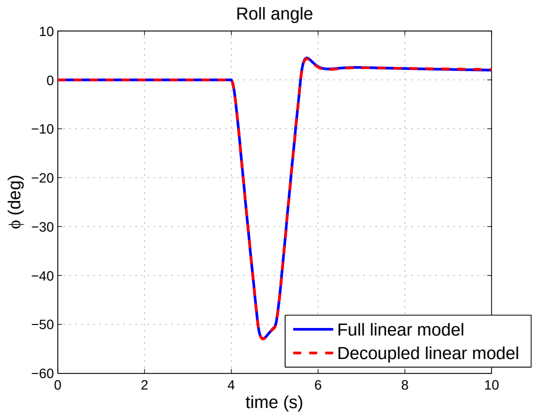

(c) Roll angle

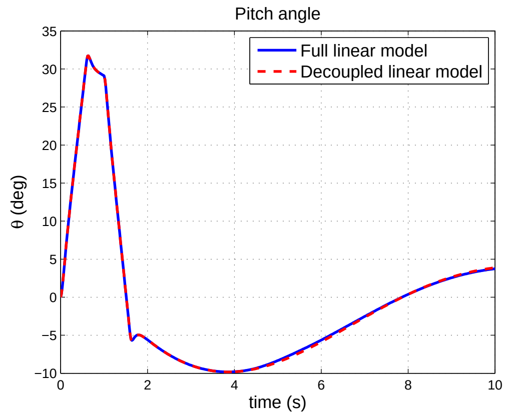

(d) Pitch angle

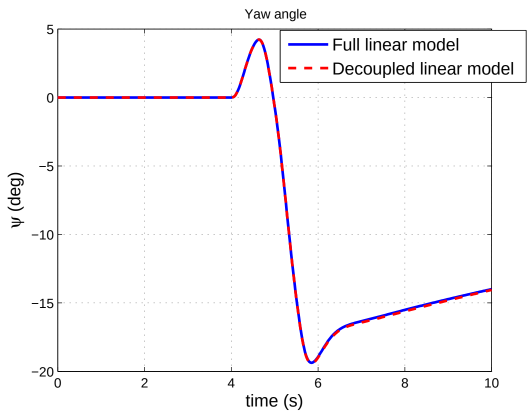

(e) Yaw angle

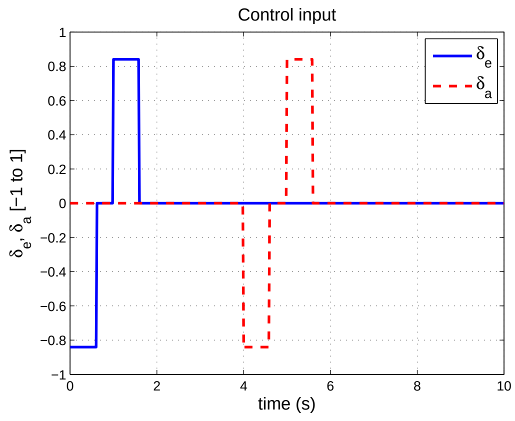

(f) Control input

Figure 3.4: Comparison of full linear and decoupled linear model output responses

### 3.1.2 Parameterized State-space Lateral Model

The results from Section 3.1.1.1 and 3.1.1.2 show that the decoupled models are able to provide almost similar matching response to that of the nonlinear model. Therefore, it is valid to use parameters identified from a linear decoupled model to update aerodynamic coefficients in the nonlinear simulation model. The linear decoupled lateral model from Equation 3.6 can be reduced to four states model (Equation 3.7) by removing yaw angle state, $\psi$, since it does not couple to other states and its dynamics is simply the yaw rate state $r$. The lateral model contains three basic lateral modes of the aircraft lateral motion. They are roll, Dutch-roll and spiral mode. These modes describe the roll, yaw and roll-yaw coupled angular motions of the aircraft. The stability matrix can be partition into four different parts where the two diagonal blocks provide pure yaw and roll dynamics while the remainder two blocks give the coupling effects for the pure roll and yaw angular dynamics. The Dutch-roll and spiral mode of the aircraft are due to the couplings of roll and yaw dynamics.

$$\begin{bmatrix} \dot{r} \\ \dot{v} \\ \dot{p} \\ \dot{\phi} \end{bmatrix} = \left[\begin{array}{cc|cc} \multicolumn{2}{c|}{\textit{yaw}} & \multicolumn{2}{c}{\textit{roll to yaw coupling}} \\ N_r & N_v & N_p & 0 \\ -(u_0 - Y_r) & Y_v & Y_p & Y_\phi \\ \hline L_r & L_v & L_p & 0 \\ 0 & 0 & 1 & 0 \\ \multicolumn{2}{c|}{\textit{yaw to roll coupling}} & \multicolumn{2}{c}{\textit{roll}} \end{array}\right] \begin{bmatrix} r \\ v \\ p \\ \phi \end{bmatrix} + \begin{bmatrix} N_{\delta_a} & N_{\delta_r} \\ 0 & Y_{\delta_r} \\ L_{\delta_a} & L_{\delta_r} \\ 0 & 0 \end{bmatrix} \begin{bmatrix} \delta_a \\ \delta_r \end{bmatrix} \tag{3.7}$$

Due to the limitations of the IMU/GPS sensor and sensor fusion algorithm used in the current stage of the project development, the lateral velocity $v$ obtained from the sensor has poor accuracy with low sampling rate. The lateral velocity measurement data will not be used for this research due to its poor quality, hence no lateral velocity state data is available for lateral model parameter identification and it is removed from the state-space model in Equation 3.7. The yaw dynamics has $N_v$ eliminated and the roll dynamics has $L_v$ eliminated, resulting in a three-state model (Equation 3.8). The three-state lateral model is able to capture the immediate roll and yaw rate dynamics but not the Dutch-roll and spiral modes.

$$\begin{bmatrix} \dot{p} \\ \dot{r} \\ \dot{\phi} \end{bmatrix} = \begin{bmatrix} L_p & L_r & 0 \\ N_p & N_r & 0 \\ 1 & 0 & 0 \end{bmatrix} \begin{bmatrix} p \\ r \\ \phi \end{bmatrix} + \begin{bmatrix} L_{\delta_a} & L_{\delta_r} \\ N_{\delta_a} & N_{\delta_r} \\ 0 & 0 \end{bmatrix} \begin{bmatrix} \delta_a \\ \delta_r \end{bmatrix} \tag{3.8}$$

For flight test parameter identification, the three-state model is further reduced to a two-state model since the roll angle dynamics $\dot{\phi}$ is simply equal to the roll rate $p$ and is eliminated from the three-state model. The final form of the parameterized state-space model used for parameter identification is given by:

$$\begin{bmatrix} \dot{p} \\ \dot{r} \end{bmatrix} = \begin{bmatrix} L_p & L_r \\ N_p & N_r \end{bmatrix} \begin{bmatrix} p \\ r \end{bmatrix} + \begin{bmatrix} L_{\delta_a} & L_{\delta_r} \\ N_{\delta_a} & N_{\delta_r} \end{bmatrix} \begin{bmatrix} \delta_a \\ \delta_r \end{bmatrix} \tag{3.9}$$

Using a two-state lateral model for parameter identification has its drawbacks. The effect on the two-state lateral model fidelity will be addressed and subsequently, its impact on aerodynamic coefficients updating will be analyzed.

#### 3.1.2.1 Limitations of Two State Lateral Model Structure

The plots in Figure 3.5 show the open loop experimental flight test responses of the Ultra-stick UAV with separate doublet signal excitation applied to the aileron and rudder control inputs at trim flight condition. The aircraft has a primary roll rate motion (roll mode) and a small yaw rate coupled motion with aileron doublet input (Figure 3.5(a)). The coupled yaw rate is in the opposite direction of the roll motion, which is commonly known as adverse yaw rate effect. The aircraft shows primary yaw rate motion first and subsequently, a large roll and yaw rate oscillations are observed with rudder control input (Figure 3.5(b)), even though there is no aileron control input applied. This is due to aircraft sideslipping with the rudder control input. The whole sequence of oscillations is Dutch-roll motion, which corresponds to coupled motion between the roll and yaw rate. In summary,

- The two-state model is able to capture the dynamics (roll mode and adverse yaw rate) due to aileron control input. Hence, good parameter estimates, $L_p$, $L_{\delta_a}$ and $N_{\delta_a}$, should be obtained with aileron perturbation input.

- The two-state model can only capture the primary yaw rate response and not the complete Dutch-roll mode response with rudder control input. This will result in poor parameter estimates of $L_{\delta_r}$, $L_{\delta_r}$, $L_r$ and $N_p$ which are related to the rudder control input coupling mode. Parameter estimates for $N_r$ and $N_{\delta_r}$ should be accurate since they are primary associated with yaw motion.

- To be able to capture all the three lateral modes, the lateral velocity state $v$ has to be included in the state-space model. This is the limitation for the proposed two-state lateral model structure.

## 3.2 Design of Experiment

The task of collecting "good data" is crucial to parameter identification. The term "good data" implies that the data collected contains information on the aircraft dynamics within the operating range of interest. Thus the parameter identification can extract accurate parameter estimates. Therefore, it is important to design and conduct appropriate flight test experiments to collect data for parameter identification. The design of experiment consists of two different aspects which are associated with flight tests, input signal design and data acquisition.

### 3.2.1 Flight Tests

The objective of flight tests is to identify parameters in the reduced lateral model in Equation 3.9 at a trim, straight and leveled flight condition operating under cruise flight condition given in Table 3.1. The parameters to identify consist of roll and yaw rate stability derivatives and aileron and rudder control derivatives. To identify these parameters, aileron and rudder control inputs have to be applied to excite the lateral dynamics. Based on knowledge of aircraft flight dynamics, an aileron control input will result in bank-to-bank roll motion while rudder control input will result in Dutch-roll motion. An aileron or rudder control input will cause the aircraft to roll. However, the aileron control input will produce a larger roll rate response when compared to a rudder control input. The aileron control and rudder control inputs are applied in a separate time window during the flight maneuvers to capture the different dynamics produced by these two lateral control inputs.

### 3.2.2 Input Signal Design

The control input signals for parameter identification have to be designed to excite the aircraft dynamics in the frequency range of interest. In addition, practical constraints have

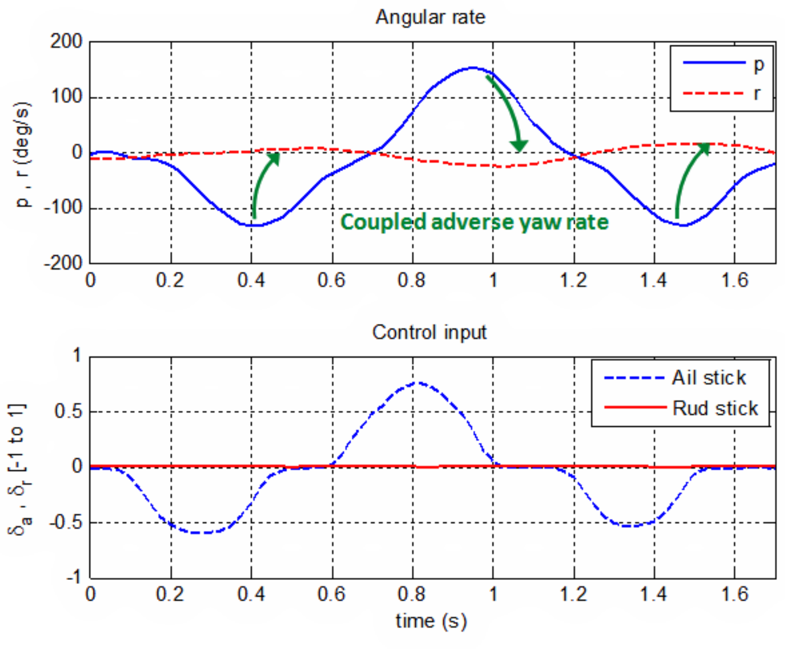

(a) Aileron control input

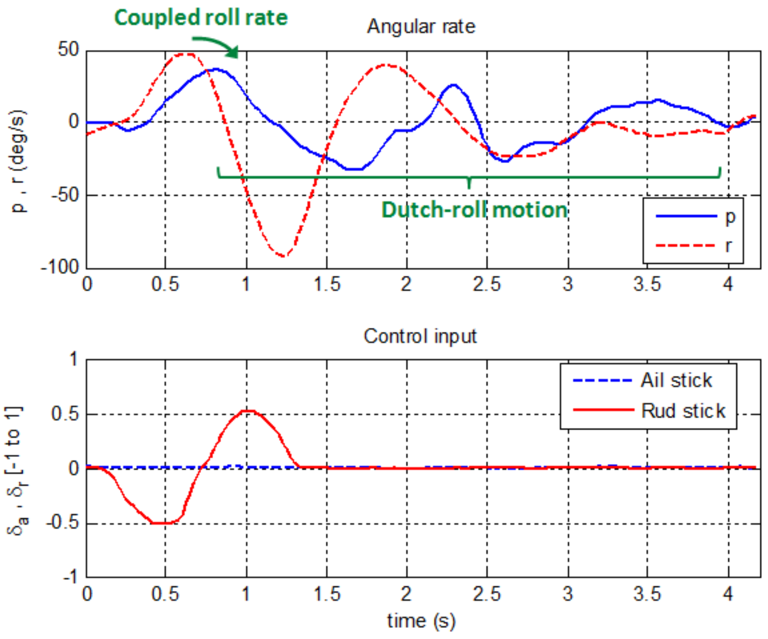

(b) Rudder control input

Figure 3.5: Open-loop experimental flight test responses

to be imposed on the feasibility of the excitation signals for flight testing. In the open-loop identification experiment, control input excitations are executed by RC pilot using the RC joystick box from the ground within visual range from the aircraft. This imposed a constraint on the type and frequency of control input signal that can be generated. The input signal design described is not based on an optimal input design approach such as in [34] but rather based on practical flight test constraints.

The doublet excitation signal (Figure 3.6(a)) has been widely used in aircraft system identification due to its simplicity in design and its ease of execution. It is a symmetrical signal pulse obtained by applying control input stick abruptly in each of the opposite direction and holding fixed for a period of $\triangle_t$ and returning back to neutral stick position. The design variable for the doublet input signal design is the period $\triangle_t$. The period is selected such that the dominant frequency of the input signal is close to the frequency range of interest ($\omega_m$) for the aircraft dynamics to be excited. This is approximated by [31]:

$$\triangle_t = \frac{2.3}{\omega_m} \tag{3.10}$$

The amplitude of the doublet input is selected such that the aircraft dynamic response is large enough to provide good signal-to-noise response data to capture the flight dynamics but not too large for the aircraft to get out of its operating regime of interest in which the parameters identified are assumed to be constant.

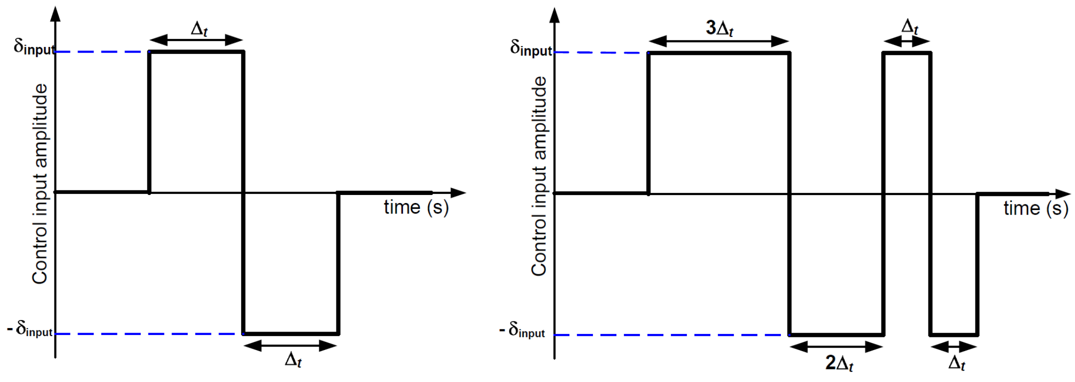

(a) Doublet control input (b) 3-2-1-1 control input

Figure 3.6: Control input signals for parameter identification

A multistep 3-2-1-1 signal is used (Figure 3.6(b)) to increase the frequency range of input signal excitation. The 3-2-1-1 input is similar to doublet signal except that it has two more pulses of different widths. The 3, 2 and 1 represent the ratio of period $\triangle_t$ used in the multistep signal where the 3 and 1 signal give the upper and lower frequency bounds for the range of input frequencies excitation. The advantage of using 3-2-1-1 signal is it provides a richer frequency excitation signal than the doublet signal. However, this requires a longer flight maneuver time which can be a constraint during flight test execution.

### 3.2.3 Data Acquisition System

The data acquisition system measures and records sensor measurement time history data for parameter identification. Figure 3.7 shows the schematic layout of the data acquisition system. The IMU/GPS sensor data (refer to Section 2.1.2) is sampled at 50 Hz. The control input signals acquired from the RC receiver to control the servo actuators are also sampled at 50 Hz. The data are recorded on first channel of the dual channels datalogger. The IMU/GPS sensor does not output attitude angles ($\phi$, $\theta$ and $\psi$) data, hence the flight computer is used to perform real-time attitude determination. The attitude angles computed are datalogged on second channel of the datalogger at 20 Hz. The attitude angles are recorded at a lower sampling rate due to the limitation of the flight computer in outputting the data through the second serial port at a high data rate. Important flight condition data such as airspeed and altitude information are sent in real-time to the ground monitoring station through wireless data modem during flight test. This provides real-time information for monitoring the flight test to ensure that it is conducted at the required operating condition.

The sampling of measurement data at 50 Hz imposed a limit on the frequency range for parameter identification without falling into aliasing problem where higher frequencies signal distort the lower frequencies data. From Nyquist-Shannon sampling theorem, aliasing can be avoided by limiting the frequency range to be below the Nyquist frequency, which is half of the sampling frequency. The IMU/GPS sensor limits the maximum data output rate to 50 Hz. The Nyquist frequency provides a theoretical maximum frequency without aliasing problem. For good engineering practice, a lower limit on the useful measured data frequency range is adopted. The limit is set to be 1/4 of the sampling frequency of 12.5

Hz.

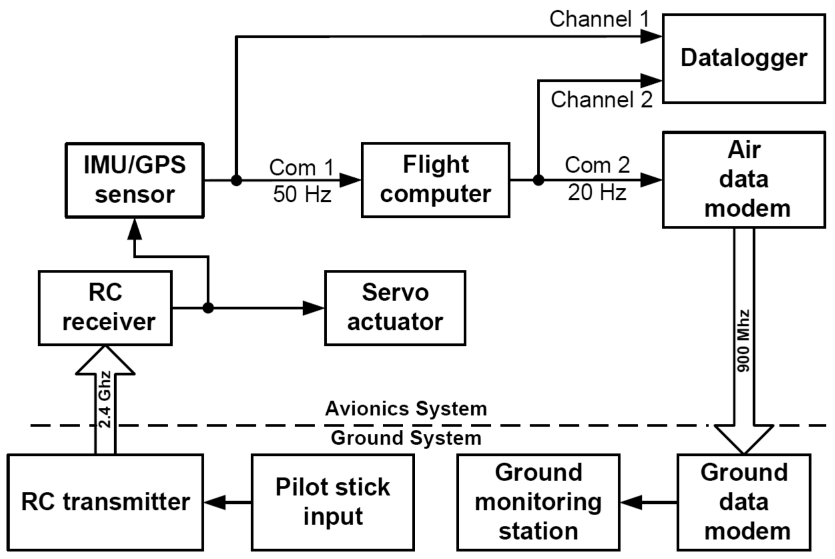

Figure 3.7: Data acquisition system for open-loop parameter identification

## 3.3 Flight Test Execution

Open-loop parameter identification flight tests are executed with an RC pilot. First, the aircraft is flown to the required trim operating condition (in Table 3.1). Before the start of each maneuver for a given trim flight condition, a 2 to 3 seconds steady flight is maintained before executing the required control inputs excitation for the maneuver. After the completion of control inputs execution, sufficient time is given for the aircraft to response so that the natural dynamics of aircraft can be captured by the sensor. The procedures for the open-loop parameter identification flight testing is summarized in Figure 3.8.

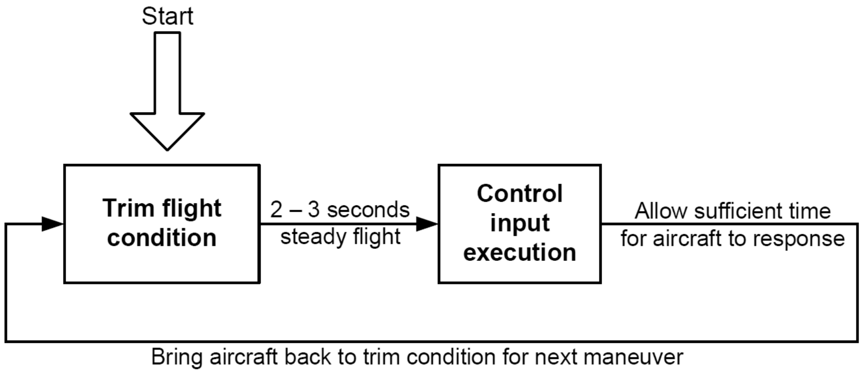
Start
Trim flight condition
2 – 3 seconds steady flight
Control input execution
Allow sufficient time for aircraft to response
Bring aircraft back to trim condition for next maneuver

Figure 3.8: Flight test procedures for open-loop parameter identification

In bank-to-bank roll maneuver, a doublet/3-2-1-1 control input signal is applied to the aileron control to give an approximate $\pm$ 10 degrees variation in roll angle from the trim position. During the maneuver, the RC pilot has to maintain the longitudinal trim of the aircraft using the throttle and elevator control inputs. For the Dutch roll maneuver, doublet/3-2-1-1 signal is applied to the rudder control stick to give an approximate $\pm$ 15 degrees variation in heading angle from the trim position while the longitudinal trim is maintained using throttle and elevator control inputs. Each flight maneuver is repeated for at least 4 times to collect sufficient data for parameter identification and validation.

The main difficulty facing the RC pilot executing the control inputs excitation is to maintain longitudinal trim of the aircraft during the maneuvers. Timing the inputs precisely while commanding roll and yaw angle to the required perturbation angles from the trim position at the same time using only visual contact on the small aircraft can be challenging.

## 3.4 Parameter Identification Technique

The method used for parameter identification is output error method. This method iteratively adjusts the parameter estimates in order to minimize the difference between measured flight test data and output response of the estimated model in each of the iteration. Since its introduction in 1960s, output error method is the most widely applied time-domain flight test parameter estimation method [31]. In recent years, maximum likelihood parameter estimation method has been one of the most popular methods used for minimization of residual error. The reason for its popularity is due to its desirable statistical properties such as asymptotically unbiased and consistent estimates. This is very useful for flight test parameter identification since flight test data contains measurement errors [35].

The maximum likelihood parameter estimation method finds the best parameter estimate for the model by maximizing a likelihood function. The likelihood function for a sequence of measurement $Z_N = [z_1 \ z_2 : : : z_n]^T$ with unknown parameter vector $\hat{\mathbf{x}}$ is given by equation:

$$L(Z|\hat{\mathbf{x}}) = \frac{1}{[(2\pi)^n |R|]^{0.5}} exp\left\{-\frac{1}{2}[z_i - h_i(\hat{\mathbf{x}})]^T R^{-1} [z_i - h_i(\hat{\mathbf{x}})]\right\} \tag{3.11}$$

The likelihood function represents the probability density function of the measured variable $Z_N$ and not $\hat{\mathbf{x}}$ parameter. The main objective is to maximize $L(Z|\hat{\mathbf{x}})$ with the selection of $\hat{\mathbf{x}}$ parameter. Maximization of the likelihood function to obtain the maximum likelihood estimate leads to a minimization of a weighted least-square function on the residual given by:

$$f(\hat{\mathbf{x}}) = \frac{1}{2}\sum_{i=1}^{N}[z_i - h_i(\hat{\mathbf{x}})]^T R^{-1} [z_i - h_i(\hat{\mathbf{x}})] \tag{3.12}$$

Details of the derivations are not given but can be found in [31, 32, 35]. This leads to a nonlinear optimization problem due to the nonlinear connection between the parameter estimates and model outputs. Figure 3.9 shows the schematic of the maximum likelihood parameter identification.

The software toolbox **SIDPAC** (**S**ystem **ID**entification **P**rograms for **A**ir**C**raft) developed in [32] is used for the maximum likelihood parameter identification of the lateral UAV model. In the problem formulation, the assumption of no process noise is made. Since process noise is neglected, the state can be computed deterministically by direct numerical integration. Hence it is important to perform flight tests on days with calm air so that the process noise is negligible.

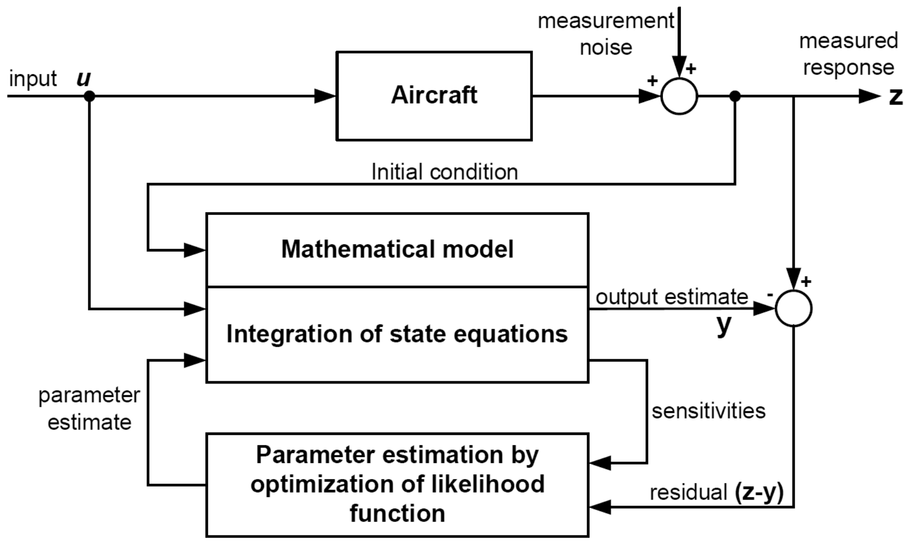

Figure 3.9: Schematic for output error parameter identification

### 3.4.1 Parameter Identification Setup

The maximum likelihood parameter estimation is done using **SIDPAC** Matlab script file. Figure 3.10 shows the flow diagram of **SIDPAC** parameter estimation process for the parameter identification setup. The details of the estimation process and setup are as follows:

- The parameterized state-space model in Equation 3.9 provides the model structure with unknown parameters to be identified.

- The initial guess of the parameter estimates have to be provided. These values cannot be arbitrary since output error maximum likelihood method is sensitive to initial guess value. Using initial guess values that are far from the minimum optimization cost function value will result in a longer iteration cycle time for convergence. The initial guess values used are from the result obtained from simulator parameter tuning in Section 2.2.1.4. They provide a good initial guess values for the parameter identification.

- Convergence criteria have to be provided as pass/fail criteria to determine if the parameter estimates have converged to give a solution that maximized the likelihood function. The convergence criteria are:

  1. Negligible change of cost of likelihood function
  2. Negligible change of parameter estimate value
  3. Negligible change of parameter estimate covariance value
  4. Absolute value of the cost gradient

  Once the convergence criteria have been satisfied (optimization has converged to a solution), this will give the converged parameter estimates and covariance solution.

- A modified Newton-Raphson method performs the optimization of likelihood function using both the residual of the difference between flight data and model output response and the sensitivity of the output response to the change in parameter estimates.

- Numerical integration (Runge-Kutta method) and partial derivative (central finite difference method) approaches are used to compute the output estimates and sensitivities. The initial condition used for parameter identification is the first value of the flight data time history.

### 3.4.2 Procedure

Parameter estimation of the lateral model is performed in three steps based on the understanding of the lateral mode dynamics and the two-state lateral model structure limitations discussed in Section 3.1.2. The 3 steps are:

- **Step 1**: Identification of primary yaw dynamics based on short data time history (before the Dutch-roll mode starts) with rudder control input excitation. The parameters to be identified are $N_r$ and $N_{\delta_r}$.

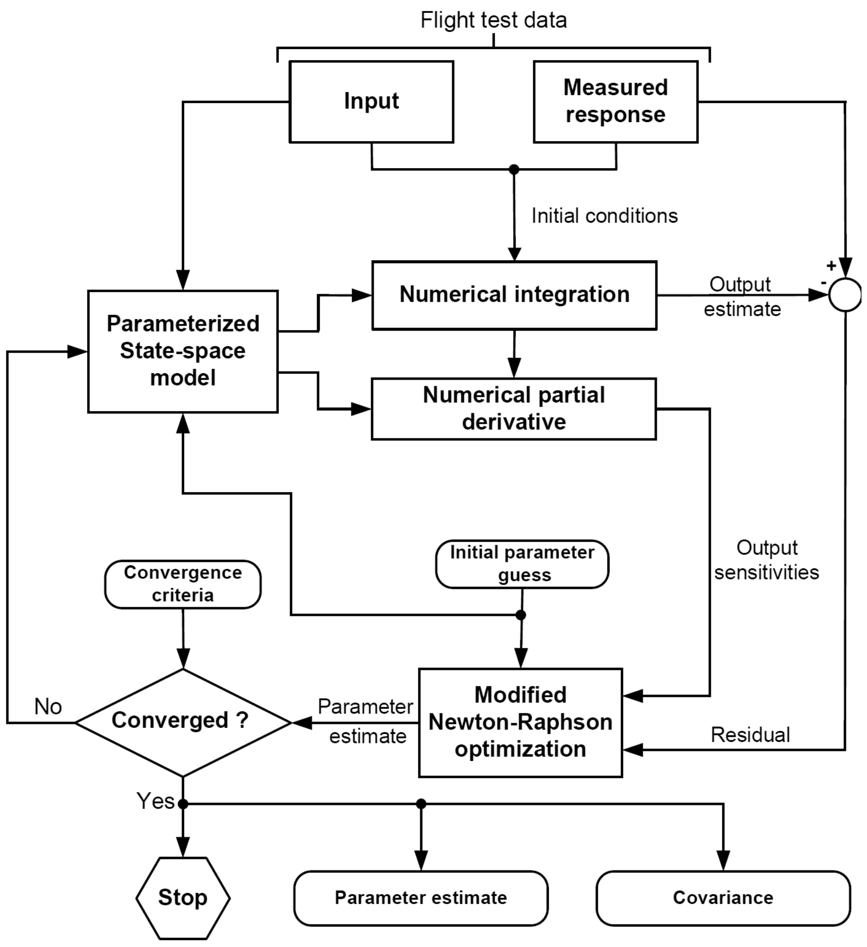

Figure 3.10: **SIDPAC** parameter estimation process

- **Step 2**: Identification of the primary roll and roll to yaw coupling dynamics with aileron control input excitation. The coefficients $N_r$ and $N_{\delta_r}$ previously identified are used in the model. The parameters to be identified are $L_p$, $N_p$, $L_{\delta_a}$ and $N_{\delta_a}$.

- **Step 3**: Identification of yaw to roll coupling dynamics using a longer time history data with rudder control input excitation with the rest of the identified parameters from Step 1 and 2. The parameters to be identified are $L_r$ and $L_{\delta_r}$.

## 3.5 Result

Flight test data was collected with RC pilot providing doublet and 3-2-1-1 input excitation with period $\triangle_t$ of approximately 0.6 seconds. Figure 3.11 shows the first set of flight test data used for parameter identification. This set of data is used to illustrate the 3 steps used for the parameter estimation procedure.

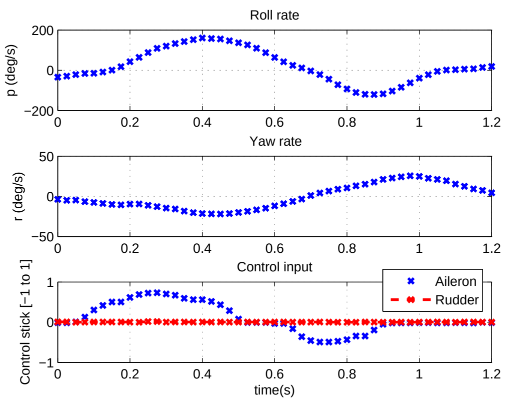

(a) Aileron control input excitation

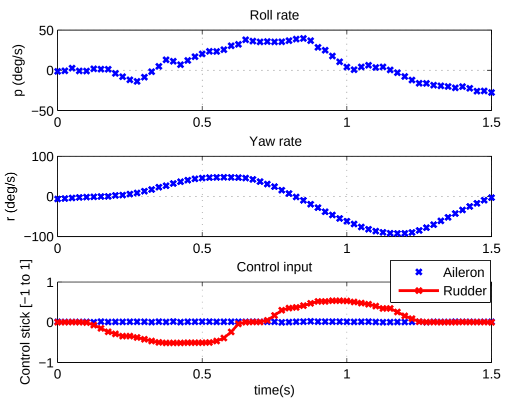

(b) Rudder control input excitation

Figure 3.11: Flight test data for model 1 parameter identification

- **Step 1**:

  Step 1 uses the rudder input excitation with short time history data of yaw rate to identify the primary yaw dynamics. Figure 3.12(a) shows the matching of the identification result. The parameters obtained are:

$$N_r = \text{-8.48 } s^{-1},\ N_{\delta_r} = \text{-17.5 } s^{-2}$$

- **Step 2:**

  Step 2 uses the aileron input excitation with roll and yaw rate responses to identify the primary roll and roll to yaw coupling dynamics. Figure 3.12(b) shows the matching of the identification result. The parameters obtained are:

$$L_p = \text{-12.0 } s^{-1},\ N_p = 0.294\ s^{-1},\ L_{\delta_a} = 58.1\ s^{-2},\ N_{\delta_a} = \text{-6.58 } s^{-2}$$

- **Step 3:**

  Step 3 uses the full time history rudder input excitation with roll and yaw rate responses to identify the yaw to roll coupling dynamics. Figure 3.12(c) shows the matching of the identification result. The parameters obtained are:

$$L_r = 12.7\ s^{-1},\ L_{\delta_r} = 13.6\ s^{-2}$$

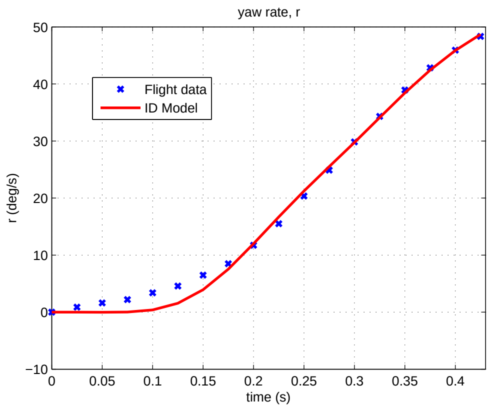

(a) Step 1

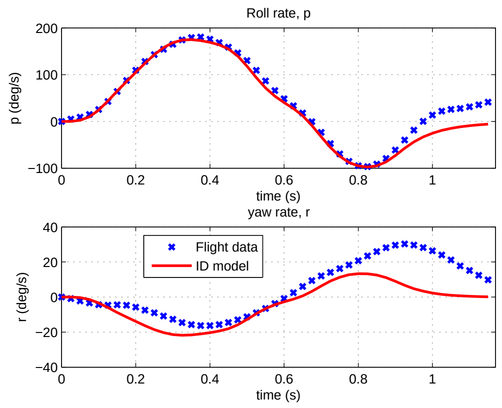

(b) Step 2

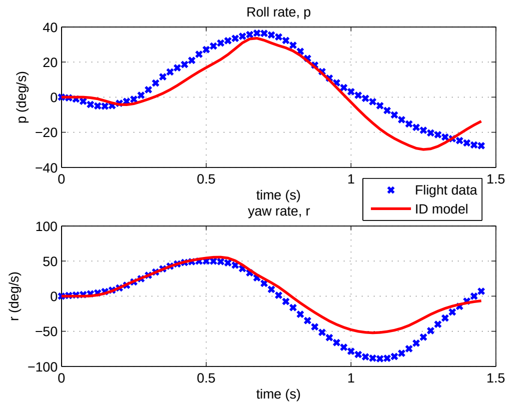

(c) Step 3

Figure 3.12: Model 1 parameter identification

The same parameter estimation procedure is being applied to two other sets of flight test data and the plots for the parameter estimation can be found in Appendix B.4. Table 3.2 gives a summary of parameters estimation results for the three sets of data.

| Derivatives | ID model 1 | ID model 2 | ID model 3 |
|---|---|---|---|
| $L_p(s^{-1})$ | -12.0 | -12.8 | -11.1 |
| $L_r(s^{-1})$ | 12.7 | 14.4 | 8.62 |
| $N_p(s^{-1})$ | 0.294 | -0.448 | 0.687 |
| $N_r(s^{-1})$ | -8.48 | -6.08 | -4.62 |
| $L_{\delta_a}(s^{-2})$ | 58.1 | 61.4 | 43.3 |
| $L_{\delta_r}(s^{-2})$ | 13.6 | 12.4 | 8.99 |
| $N_{\delta_a}(s^{-2})$ | -6.58 | -3.67 | -4.76 |
| $N_{\delta_r}(s^{-2})$ | -17.5 | -15.0 | -11.9 |

Table 3.2: Summary of estimated parameters from flight test data

|  | ID Model 1 | ID Model 2 | ID model 3 |
|---|---|---|---|
| $\tau_{roll}$ $(s)$ | 0.083 | 0.078 | 0.090 |

Table 3.3: Identified models roll mode time constant

### 3.5.1 Stability Derivatives

#### 3.5.1.1 Primary Roll Dynamics

The aircraft primary roll mode is captured by the $L_p$ derivative. This gives the time constant for the pure roll mode, $\tau_{roll}$ $(s)$, of the aircraft [20]:

$$\tau_{roll} = -\frac{1}{L_p} \tag{3.13}$$

The time constants of the three identified models are calculated using the identified models in Table 3.2. This is given in Table 3.3. The three identified models roll mode time constants are close to each other. Results published on the similar small-scale UAVs in [36] have roll mode time constants of 0.10, 0.06 and 0.09 seconds. This is very similar to our results obtained. This shows that the primary roll mode is well captured and identified from the flight test system identification. It is essential to identify $L_p$ parameter accurately because it is an important parameter in the lateral model dynamics for the roll angle controller synthesis.

### 3.5.2 Yaw and Coupled Roll-yaw Dynamics

The primary yaw mode dynamics is described by $N_r$ parameter and the identified values in Table 3.2 show that the three identified values are reasonably close and have the correct negative sign. The negative sign in $N_r$ means that a positive yaw rate produces a positive side force on the vertical tail. This produces a negative yawing moment and opposes the yaw rate motion, which provides yaw damping for the aircraft.

The $L_r$ parameter captures the aircraft roll to yaw coupling dynamics. A close agreement of the identified $L_r$ values is obtained from the three identified models (in Table 3.2) and this will provide a reasonably good description of the roll to yaw coupling dynamics from the identified models. On the other hand, the $N_p$ parameter which captures the aircraft yaw to roll coupling dynamics has a large variation. This poor matching of the three $N_p$ values obtained from the flight test identification in Table 3.2 indicates that the yaw to roll dynamics is not well captured. Part of the reason for this poor matching is the due to the limitation of the two-state model structure used in the lateral-directional mode identification described in Section 3.1.2.1.

### 3.5.3 Control Derivatives

The $L_{\delta a}$, $L_{\delta r}$, $N_{\delta a}$ and $N_{\delta r}$ control derivatives identified provide a measure of input sensitivities of the aileron and rudder control to the roll ($L$) and yaw ($N$) moment of the aircraft. The ratio of $L_{\delta a}$ to $L_{\delta r}$ and $N_{\delta r}$ to $N_{\delta a}$ provide the relative magnitude of each control derivative to the roll and yaw moment. Table 3.4 contains these ratios derived from the three identified models in Table 3.2.

The relative magnitude of $L_{\delta a}$ to $L_{\delta r}$ contribution to the aircraft roll moment ($4:1$ from Table 3.4) makes sense as the aircraft primary roll moment is obtained from aileron control input and smaller roll moment is obtained with rudder input. A ratio of approximately 0.2 for $L_{\delta r}/L_{\delta a}$ from the three identified models in Table 3.4 indicates good consistency of roll control derivatives identified from aileron and rudder inputs. However, for the yaw moment, the ratios of $N_{\delta a}$ to $N_{\delta r}$ have a variation between 0.25 to 0.40 (Table 3.4). This indicates that the yaw control derivatives identified have poor matching result within the three identified models.

|  | ID Model 1 | ID Model 2 | ID model 3 |
|---|---|---|---|
| $\frac{L_{\delta r}}{L_{\delta a}}$ | 0.234 | 0.202 | 0.208 |
| $\frac{N_{\delta a}}{N_{\delta r}}$ | 0.376 | 0.245 | 0.400 |

Table 3.4: Control derivatives ratio

## 3.6 Model Verification

### 3.6.1 Time Domain Model Verification

Time domain verification of the three identified models is performed by comparing the identified models with a longer time history flight test data not used in the parameter estimation process. The time history plots of the identified models were obtained using the measured control inputs from the model verification data. Figure 3.13 shows the comparison plots for the identified models and verification data. With aileron control input (Figure 3.13(a)), the identified models show good matching in the roll rate response and poor matching in the coupled yaw rate response. The good matching of the roll rate response with aileron control input is due to good parameter identification results for $L_p$, $L_r$ and $L_{\delta a}$ parameters. The poor yaw rate response matching in the time domain validation is due to poor $N_p$ and $N_{\delta_a}$ parameter identification results described in Section 3.5.

With rudder control input (Figure 3.13(b)), again, the roll rate response from the identified model shows good matching with the flight test data but not the yaw rate response. However, during the initial short time period when the rudder control input is applied, the yaw rate response from the identified models are able to match the flight test data well. However when the Dutch-roll mode kicks in, the identified models responses are not able to match the flight test data results. Again, this is mainly due to the limitation of the two-state state-space model used.

### 3.6.2 Frequency Domain Model Verification

The same set of validation data used in the time domain verification (Figure 3.13) is used for frequency domain model verification. Discrete Fourier transform is used to transform the time domain verification data to frequency domain. In the frequency domain model

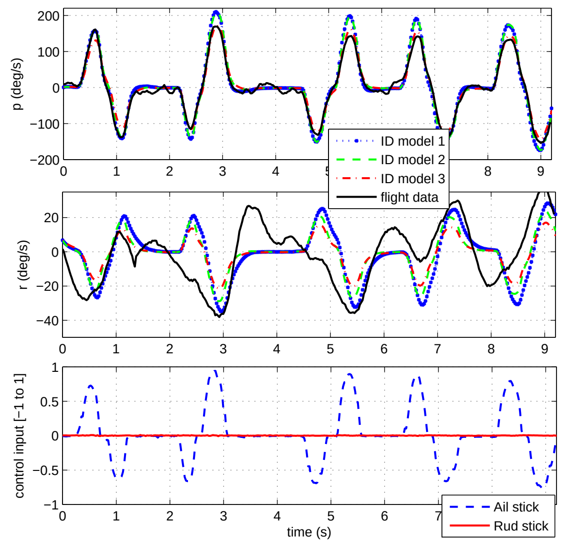

(a) Aileron control input

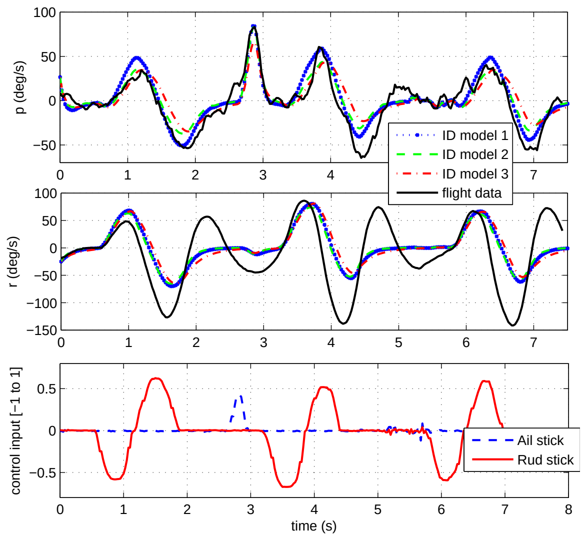

(b) Rudder control input

Figure 3.13: Time domain verification of identified models

verification analysis, the relevant frequency range of interest is limited by the control input signals excitation frequency and data sampling rate. Since a data sampling rate of 50 Hz is used, frequency domain data above 79 $rad/s$ is not useful for the verification analysis (cutoff frequency is selected to be 1/4 of the data sampling rate). In addition, the frequency response of the validation data is representative of the aircraft dynamics within the range of control input excitation frequencies.

Figure 3.14 shows the FFT plots for the input and output data sets used in the the model validation. In Figure 3.14(a), the FFT of roll rate output response is plotted together with aileron control input signal applied. In Figure 3.14(b), the FFT of yaw rate output response is plotted together with rudder control input signal applied. The two plots in Figure 3.14 show a good matching magnitude across the frequencies for the control input signals to excite the aircraft angular rate dynamics within the same frequencies range. The aileron and rudder control input excitation frequency range, $\omega_R$, are approximately between 1 to 8 $rad/s$ in both of the plots in Figures 3.14(a) and 3.14(b). The frequency domain model verification is only valid within the $\omega_R$ frequency range.

Figure 3.15 shows frequency response plots of the identified models with the verification

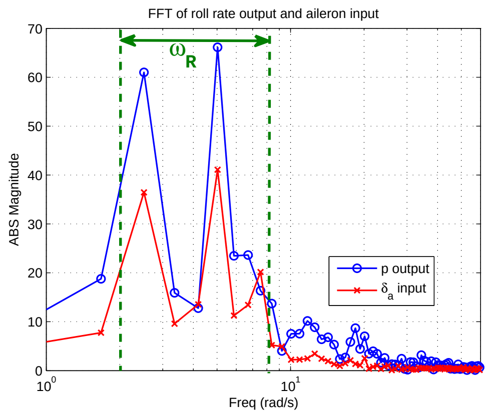

(a) Aileron input excitation

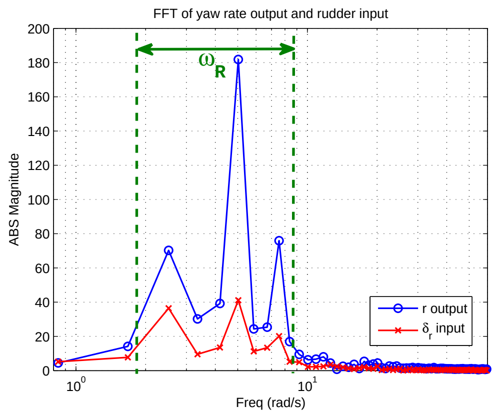

(b) Rudder input excitation

Figure 3.14: FFT of input and output flight test data used in model validation

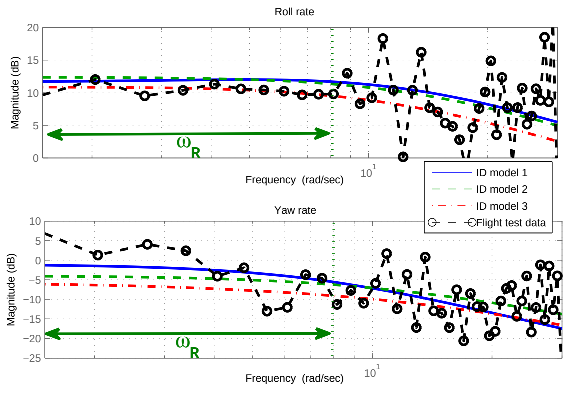

(a) Aileron input excitation

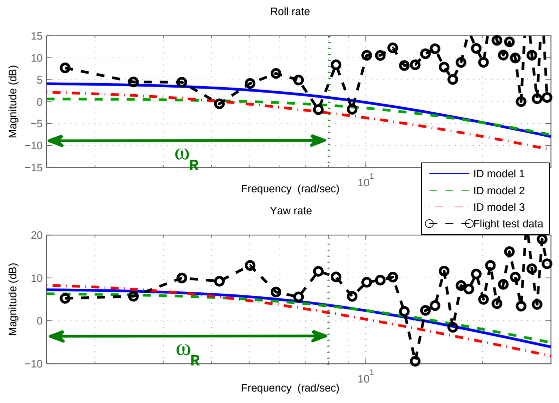

(b) Rudder input excitation

Figure 3.15: Frequency domain model verification

data for both aileron and rudder control input excitations. The frequency range of interest is limited to be within the input excitation frequency range ($\omega_R$) specified in the plots. The plots show consistent result with the time domain verification where the identified models have a good matching with the roll rate response with aileron control input but not with the rudder control input.

## 3.7 Updating of Aerodynamic coefficients in Nonlinear Model

The lateral state-space model identified is used to update the lateral aerodynamic coefficients in the nonlinear simulation model. This section will show the approach and procedure used to update the dimensionless aerodynamic coefficients in the nonlinear simulation model.

### 3.7.1 Nominal Identified Model

From Section 3.5, the three different flight test data sets produce three different identified models. However, only one of the identified models can be used to update the nonlinear simulation model. The approach taken is to compute a nominal model and an overbound from the three identified models to update the nonlinear simulation model. The overbound uses a combination of the computed nominal model and real parameter variation from the nominal model which will be covered in uncertainty modeling in Chapter 4.2.

The nominal model is obtained by using the mid-point value between the minimum and maximum value for each of the identified derivatives in the three identified models. Appendix B.5 Table B.2 presents the nominal model parameters with upper and lower bound values. Figure 3.16 shows the Bode magnitude plot for the nominal model with the three identified models. The plot shows that the nominal model frequency response lies between the three identified models frequency response. This has the benefit of reducing the size of the uncertainty bounds from the nominal model.

### 3.7.2 Aerodynamic Coefficients Computation

The nonlinear aerodynamic equations for side force, roll and yaw moment from Section 2.2.1 are given by Equations 2.1, 2.5 and 2.7:

$$C_Y = C_{Y_\beta}\beta + C_{Y_{\delta r}}\delta r + \frac{b}{2V_a}(C_{Y_p}p + C_{Y_r}r) \tag{3.14}$$

$$c_l = c_{l_\beta}\beta + c_{l_{\delta a}}\delta a + c_{l_{\delta r}}\delta r + \frac{b}{2V_a}(c_{l_p}p + c_{l_r}r) \tag{3.15}$$

$$c_n = c_{n_\beta}\beta + c_{n_{\delta a}}\delta a + c_{n_{\delta r}}\delta r + \frac{b}{2V_a}(c_{n_p}p + c_{n_r}r) \tag{3.16}$$

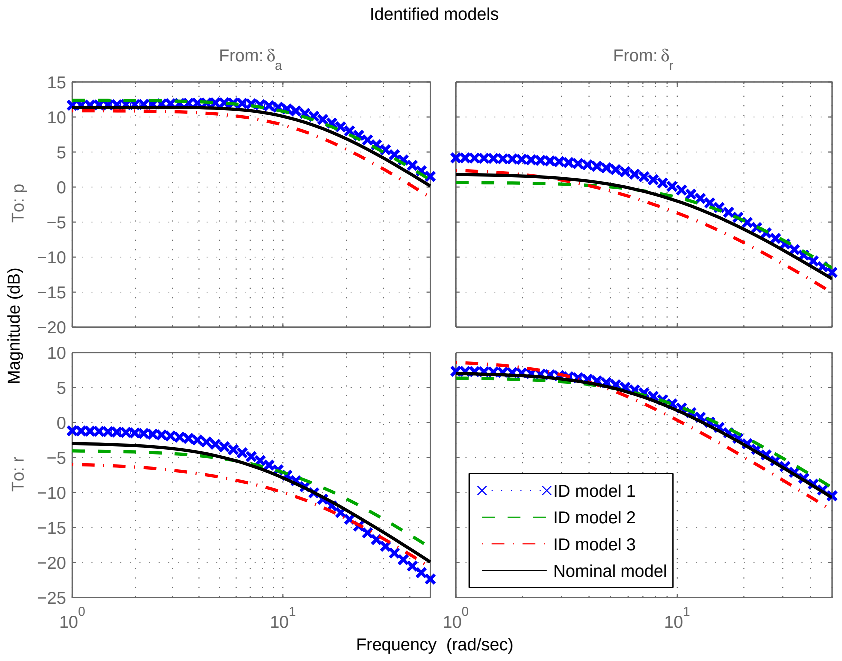

Figure 3.16: Bode magnitude plot of identified models

where $C_{Y_p}$, $C_{Y_r}$, $c_{l_p}$, $c_{l_r}$, $c_{n_p}$ and $c_{n_r}$ are dynamic aerodynamic coefficients and $C_{Y_\beta}$, $C_{Y_{\delta r}}$, $c_{l_\beta}$, $c_{l_{\delta r}}$, $c_{l_{\delta a}}$, $c_{n_\beta}$, $c_{n_{\delta r}}$ and $c_{n_{\delta a}}$ are static aerodynamic coefficients. The dynamic aerodynamic coefficients, unlike the static aerodynamic coefficients, cannot be obtained from static wind tunnel testing. They account for dampings in the aircraft dynamics and are commonly known as damping coefficients. Flight test system identification is usually used to obtain these dynamic coefficients through excitation of the aircraft dynamic modes.

The aerodynamic coefficients are the dimensionless forms of the stability and control derivatives in the state-space model in Equation 3.7. Hence the aerodynamic coefficients can be computed by removing the dimensional dependent of the identified parameters. The relationships for dimensionless computation of the aerodynamic coefficients from the identified stability and control derivatives are given in Table 3.5. In this thesis, the aerodynamic coefficients related to $\beta$ and $C_Y$ derivatives will not be updated using flight test identification results due to the limitation of the two-state state-space model used. Hence only the identified stability and control derivatives are used to update the aerodynamic coefficients ($c_{l_p}$, $c_{l_r}$, $c_{n_p}$, $c_{n_r}$, $c_{l_{\delta r}}$, $c_{l_{\delta a}}$, $c_{n_{\delta r}}$ and $c_{n_{\delta a}}$) while the rest of the aerodynamic coefficients ($C_{Y_p}$,

$C_{Y_r}$, $C_{Y_\beta}$, $C_{Y_{\delta r}}$, $c_{n_\beta}$ and $c_{l_\beta}$) are kept at the values obtained from the simulator parameter tuning (Appendix Table A.1).

| Roll moment | $c_{l_\beta}$ | $\mathbf{c_{l_{\delta a}}}$ | $\mathbf{c_{l_{\delta r}}}$ | $\mathbf{c_{l_p}}$ | $\mathbf{c_{l_r}}$ |
|---|---|---|---|---|---|
| | $\frac{I_{xx}L_\beta}{\bar{q}Sb}$ | $\frac{I_{xx}L_{\delta a}}{\bar{q}Sb}$ | $\frac{I_{xx}L_{\delta r}}{\bar{q}Sb}$ | $\frac{2I_{xx}u_0L_p}{\bar{q}Sb^2}$ | $\frac{2I_{xx}u_0L_r}{\bar{q}Sb^2}$ |
| **Yaw moment** | $c_{n_\beta}$ | $\mathbf{c_{n_{\delta a}}}$ | $\mathbf{c_{n_{\delta r}}}$ | $\mathbf{c_{n_p}}$ | $\mathbf{c_{n_r}}$ |
| | $\frac{I_{zz}N_\beta}{\bar{q}Sb}$ | $\frac{I_{zz}N_{\delta a}}{\bar{q}Sb}$ | $\frac{I_{zz}N_{\delta r}}{\bar{q}Sb}$ | $\frac{2I_{zz}u_0N_p}{\bar{q}Sb^2}$ | $\frac{2I_{zz}u_0N_r}{\bar{q}Sb^2}$ |
| **Side force** | $C_{Y_\beta}$ | $C_{Y_{\delta r}}$ | $C_{Y_p}$ | $C_{Y_r}$ | |
| | $\frac{Y_\beta m}{\bar{q}S}$ | $\frac{Y_{\delta r}m}{\bar{q}S}$ | $\frac{2mu_0Y_p}{\bar{q}Sb}$ | $\frac{2mu_0Y_r}{\bar{q}Sb}$ | |

Table 3.5: Relationships between dimensionless aerodynamic coefficients and dimensional derivatives

The four-state lateral model in Equation 3.7 uses lateral velocity state $v$ instead of $\beta$ state. However, under small angle approximation about the trim point, approximation can be made between $v$ and $\beta$ from relationship given in Equation 3.3:

$$\begin{aligned}\beta &= \sin^{-1}\left(\frac{v}{V_a}\right)\\ &= \tan^{-1}\left(\frac{v}{u_0}\right)\end{aligned}$$

For small $\beta$ angle, $\beta \approx v/u_0$. Since $u_0$ is constant, $\dot{\beta} = \dot{v}/u_0$. Replacing $v$ and $\dot{v}$ in Equation 3.7 with $\beta$ and $\dot{\beta}$, the 4 states lateral model with $\beta$ state is given by:

$$\begin{bmatrix}\dot{r}\\ \dot{\beta}\\ \dot{p}\\ \dot{\phi}\end{bmatrix} = \begin{bmatrix} N_r & \mathbf{N}_\beta & N_p & 0\\ -\left(1-\frac{\mathbf{Y_r}}{u_0}\right) & \frac{\mathbf{Y}_\beta}{u_0} & \frac{\mathbf{Y_p}}{u_0} & \frac{g\cos\theta_0}{u_0}\\ L_r & \mathbf{L}_\beta & L_p & 0\\ 0 & 0 & 1 & 0\end{bmatrix}\begin{bmatrix} r\\ \beta\\ p\\ \phi\end{bmatrix} + \begin{bmatrix} N_{\delta_a} & N_{\delta_r}\\ 0 & \frac{\mathbf{Y_{\delta r}}}{u_0}\\ L_{\delta_a} & L_{\delta_r}\\ 0 & 0\end{bmatrix}\begin{bmatrix}\delta_a\\ \delta_r\end{bmatrix} \tag{3.17}$$

where $Y_\beta = Y_v u_0$, $L_\beta = L_v u_0$ and $N_\beta = N_v u_0$. Equation 3.7 and 3.17 are equivalent to each other under small $\beta$ angle approximation. Equation 3.7 is preferred over Equation 3.17 in controller design, parameter estimation and implementation since $v$ measurement is available from the IMU/GPS sensor but not the $\beta$ angle. Equation 3.17 is derived because its parameters are directly related to the dimensionless aerodynamic coefficients in Equations 3.14, 3.15 and 3.16 which are being updated.

Dimensionless aerodynamic coefficients (coefficients in bold, Table 3.5) are computed using derivatives from the computed nominal identified model. Control and stability derivatives (derivatives in bold) in Equation 3.17 are computed from aerodynamic coefficients obtained from simulator parameter tuning. Table 3.6 gives the results of the computation.

The aerodynamic coefficients are updated using identified state-space model parameters to provide the nonlinear simulation model with the same dynamic response similar to the identified state-space model that captures the real aircraft dynamics from system identification flight testing. Comparison of the output responses from the updated nonlinear model against the identified state-space model used for updating the nonlinear simulation model will provide verification on accuracy of this approach. Figure 3.17 shows the roll and yaw rate output response comparisons of the updated nonlinear model with the four-state parameterized state-space model (augmented ID model) from Equation 3.17. The aileron and rudder control inputs used are from the validation data in Figure 3.13. The plots show that the updated nonlinear model responses have very good matching with the parameterized state-space model that was being used to update the aerodynamic coefficients. This verifies the proposed approach used to update the aerodynamic coefficients to the nonlinear model works well. Figure 3.18 shows the comparison of the updated nonlinear model with the flight test validation data from Figure 3.13. The updated nonlinear model and the validation flight test data responses are very similar to the time verification plots in Figure 3.13. This is expected since the updated nonlinear model has its aerodynamic coefficients computed from the identified state-space models. Hence for the nonlinear model to predict the actual UAV flight dynamics, it is important to get good flight test parameter identification result.

| Derivatives from identification | | Aerodynamic coefficients computed | |
|---|---|---|---|
| $L_p$ | $-1.28 \times 10^1$ | $c_{l_p}$ | $-4.43 \times 10^{-1}$ |
| $L_r$ | $1.44 \times 10^1$ | $c_{l_r}$ | $4.99 \times 10^{-1}$ |
| $N_p$ | $-4.48 \times 10^{-1}$ | $c_{n_p}$ | $-2.81 \times 10^{-2}$ |
| $N_r$ | $-6.08$ | $c_{n_r}$ | $-3.82 \times 10^{-1}$ |
| $L_{\delta_a}$ | $6.14 \times 10^1$ | $c_{l_{\delta_a}}$ | $7.94 \times 10^{-2}$ |
| $L_{\delta_r}$ | $1.24 \times 10^1$ | $c_{l_{\delta_r}}$ | $1.60 \times 10^{-2}$ |
| $N_{\delta_a}$ | $-3.67$ | $c_{n_{\delta_a}}$ | $-8.60 \times 10^{-3}$ |
| $N_{\delta_r}$ | $-1.50 \times 10^1$ | $c_{n_{\delta_r}}$ | $-3.52 \times 10^{-2}$ |
| Derivatives computed | | Aerodynamic coefficients from simulator tuning | |
| $Y_\beta$ | $-2.38 \times 10^1$ | $C_{y_\beta}$ | $-8.30 \times 10^{-1}$ |
| $L_\beta$ | $-3.09 \times 10^1$ | $C_{l_\beta}$ | $-4.00 \times 10^{-2}$ |
| $N_\beta$ | $1.47 \times 10^1$ | $C_{n_\beta}$ | $3.44 \times 10^{-2}$ |
| $Y_p$ | 0.00 | $C_{Y_p}$ | 0.00 |
| $Y_r$ | 0.00 | $C_{Y_r}$ | 0.00 |
| $Y_{\delta_r}$ | $1.26 \times 10^1$ | $C_{Y_{\delta_r}}$ | $1.91 \times 10^{-1}$ |

Table 3.6: Dimensional and dimensionless aerodynamic coefficients

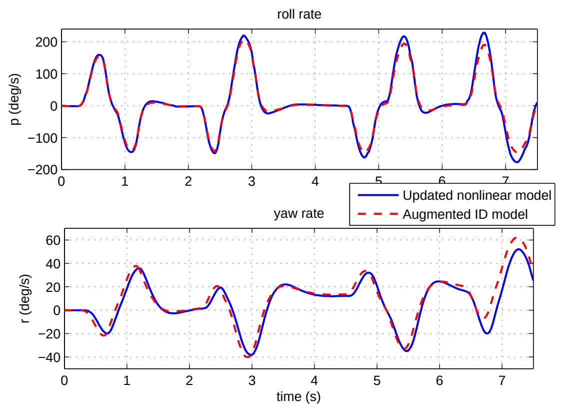

(a) Aileron input excitation

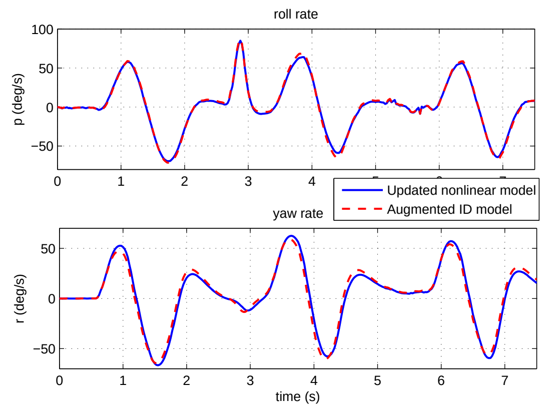

(b) Rudder input excitation

Figure 3.17: Comparison of updated nonlinear model with augmented identified model

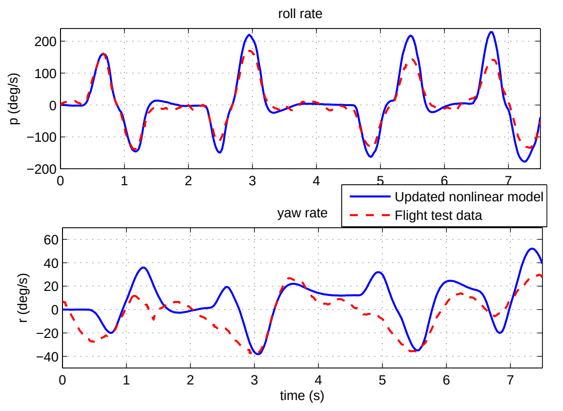

(a) Aileron input excitation

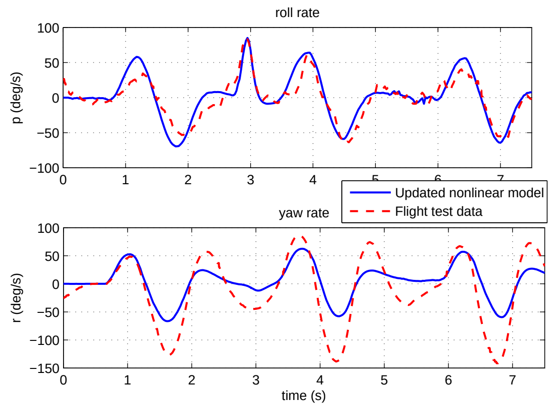

(b) Rudder input excitation

Figure 3.18: Comparison of updated nonlinear model with flight test data

# Chapter 4

# Uncertainty Models Modeling, Synthesis and Analysis

The nonlinear UAV simulation model developed in Chapter 2 is only useful if it is able to predict the actual vehicle flight dynamics response accurately. However, modeling is an approximation of the actual physical system and this results in uncertainty predicting the actual system response using the model developed. Hence it is important to include model uncertainty in the nonlinear simulation model so that it gives a confidence level as well as a bound in predicting the actual system response.

The model uncertainty description formulation for robust control problems are generally classified in two categories, structured and unstructured uncertainty [37]. The parametric uncertainty is a structured uncertainty model where the model and its order are known. The only unknown is in the value of the parameter, which is uncertain. The parametric uncertainty model structure is important as it provides parameter variations associated with the physical parameters of the system model. Therefore a systematic procedure is needed for accurate uncertainty modeling of real parameter variation. However, parametric uncertainty structure can be extremely complicated for practical interest. This is because uncertainties associated with the system physical parameters can enter into the model as nonlinear multivariate functions that are difficult to separate into nominal and uncertain components [38]. On the other hand, the unstructured uncertainty are used to model dynamics of uncertainty which are not known or neglected and is usually quantified using frequency bounding functions to characterize the level of uncertainty to be considered over various frequency ranges of interest.

The uncertain linear model order and structure used in controller synthesis are important because using a conservative uncertain model can result in poor closed-loop performance. Similarly using a uncertain model with complicated uncertainty structure may result in high order controller obtained from the controller synthesis process. Analysis of the model uncertainty can help to reduce uncertainty model order and complexity with minimum effect in the controller synthesis.

This chapter provides a systematic approach to modeling and inclusion of modeling errors into the nonlinear simulation model. To use the uncertain nonlinear model for robust control design and analysis with existing linear design and analysis tools, uncertain linear model need to be extracted from the uncertain nonlinear simulation model. A new approach for uncertain linear model realization from uncertain nonlinear simulation model is presented. This approach provides a physically meaningful Linear Fractional Transformation (LFT) model. The LFT model realization approach is applied to the nonlinear UAV simulation model. An approach to simplification of the LFT is also presented using the realized UAV LFT model.

## 4.1 Parametric Uncertainty Modeling

The physical parameters determined from various experiments (Chapter 2 and 3) for the nonlinear UAV modeling contain uncertainties due to imprecise nature of experimentation and limitation of physical system modeling. Estimated physical parameters are modeled as real parameter uncertainties with each parameter described by a nominal value and a lower and upper bound. A systematic approach is used to include these parameters into the nonlinear simulation model. The resulting uncertain nonlinear simulation model is used subsequently in linearization process for deriving uncertain linear model.

### 4.1.1 Parametric Uncertainty Representation

A parametric uncertainty set $P_\triangle$ for an uncertain parameter $P$ bounded within a region bounded by $[P_{\min}, P_{\max}]$ can be expressed in the form:

$$P_\triangle = \bar{P}(1 + W_P\delta) \tag{4.1}$$

where $\bar{P}$ is the nominal parameter value, $\delta$ is any real scalar satisfying $|\delta| \leq 1$ and $W_P$ is the relative uncertainty (weight) used to scale $\delta$ to norm size of 1 given by:

$$W_P = \frac{P_{\max} - P_{\min}}{P_{\max} + P_{\min}}$$

#### 4.1.1.1 Parametric Uncertainty Implementation Procedure

Parametric uncertainty is included into the Simulink model via a multiplicative or inverse multiplicative uncertainty structure using the *USS System* (Uncertain State-Space) block from Robust Control Toolbox [39]. The details of the implementation is illustrated using a simple example. This procedure is used to include parametric uncertainties in the UAV nonlinear simulation model.

In this example, consider a system with two inputs $u_{1,2}$, single output $y$ and three real parametric uncertainties $a_\Delta$, $b_\Delta$ and $c_\Delta$ given by the equation:

$$y = \left[\left(\frac{a_\Delta}{b_\Delta}\right) u_1 + c_\Delta\right] u_2$$

where

$$\begin{aligned} a_{min} &\leq a_\Delta \leq a_{max} \\ b_{min} &\leq b_\Delta \leq b_{max} \\ c_{min} &\leq c_\Delta \leq c_{max} \end{aligned}$$

The nominal system implemented using Simulink blocks is shown in Figure 4.1.

With parametric uncertainties, parameters $a_\Delta$ and $c_\Delta$ are expressed as multiplicative

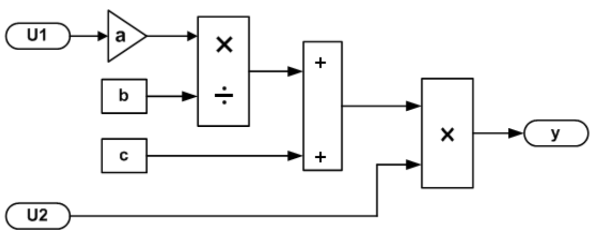

Figure 4.1: Simulink diagram for nominal system

uncertainty while $1/b_\Delta$ is expressed as inverse multiplicative uncertainty given by:

$$\begin{aligned} a_\Delta &= a(1+r_a\delta) \\ \frac{1}{b_\Delta} &= \left(\frac{1}{b}\right)\left(\frac{1}{1+r_b\delta}\right) \\ c_\Delta &= c(1+r_c\delta) \end{aligned} \quad (4.2)$$

where

- $a$, $b$ and $c$ are the nominal values of the uncertain parameters.
- $r_a$, $r_b$ and $r_c$ are weights used to scale $\delta$ to norm size of 1.
- $\delta$ is defined as real scalar satisfying $-1 \leq \delta \leq 1$.

Each $r_a\delta$, $r_b\delta$ and $r_c\delta$ is modeled as a USS System Simulink block with a *ureal* (Uncertain real parameter object in Robust Control Toolbox) object that has a zero nominal value and a weighted range of real value variation from $(k - k_{min})/k$ to $(k_{max} - k)/k$ where $k = a$, $b$ and $c$. The $c_\Delta$ parameter is relocated before output $y$ so that the uncertain parameter has multiplication with the input signal $u_2$. The reason for this modification will be explained in section 4.2.3. Figure 4.2 shows the Simulink diagram with the parametric uncertainties implemented.

### 4.1.2 Example

This section will illustrate an example of implementing parametric uncertainty into the nonlinear UAV simulation model using the aerodynamic coefficients obtained from flight test

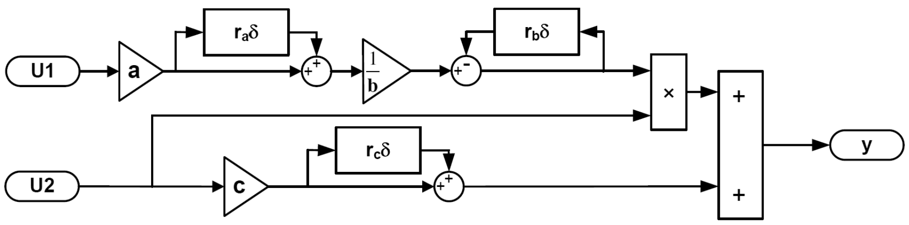

Figure 4.2: Simulink model with real parametric uncertainties

parameter identification in Section 3.5. Using the relationships for aerodynamic coefficients computation in Section 3.7, the aerodynamic coefficients computed from the nominal model with lower and upper bound values are given in Appendix Table C.1.These aerodynamic coefficients with parametric uncertainties are modeled in the nonlinear simulation model using the described technique in Section 4.1. An example of the actual Ultrastick UAV nonlinear Simulink model block diagram implemented with parametric uncertainties, the dimensionless roll moment coefficient ($c_l$) equation, is given in Appendix C.1.

With the parametric uncertainties implemented into the nonlinear simulation model, a verification is done to check the updated uncertain nonlinear simulation model produces output responses that overbound the set of responses from the flight test identified models that are used for updating the nonlinear simulation model. In the setup, 100 simulation runs are performed with random sampling of the parametric uncertainties in each of the run. A single doublet input signal is applied to both aileron and rudder control inputs to excite the uncertain nonlinear simulation model from the trim condition used in Section 3.7. Figure 4.3 shows the roll and yaw rate responses obtained from 100 simulation runs (in grey - -) from the uncertain nonlinear simulation model. In addition, three additional simulations are performed with the parametric uncertainty set to the aerodynamic coefficients obtained from identified models 1 to 3. The plot in Figure 4.3 shows that the range of roll and yaw rate time response variations with parametric uncertainty perturbations from the uncertain nonlinear simulation model covers the set of output responses from the three identified models. The implemented parametric uncertainties in the nonlinear simulation model provides an accurate description of the system output responses that contain the three flight test identified models responses.

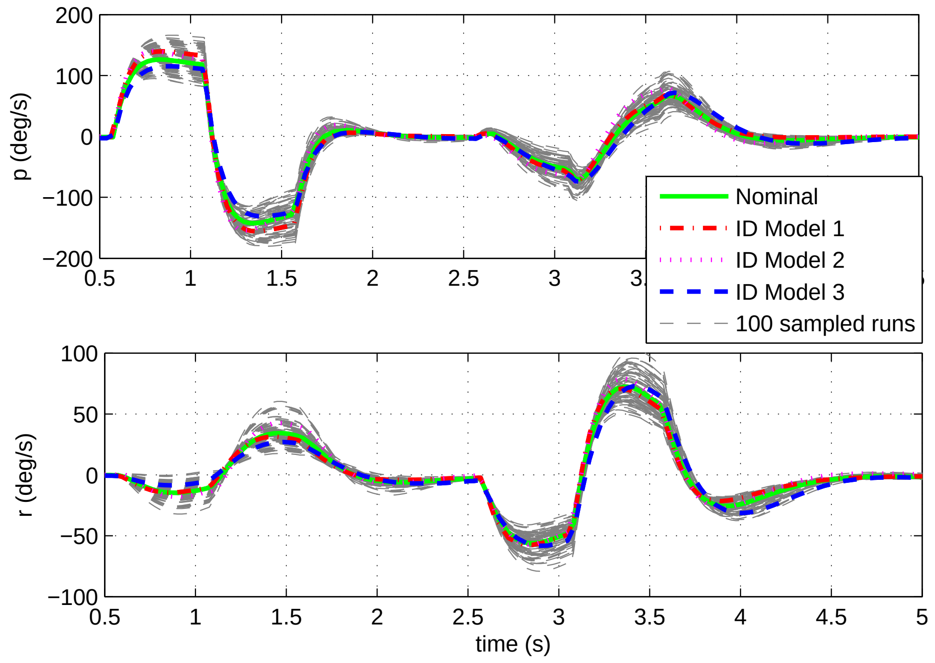

Figure 4.3: Uncertain nonlinear simulation model Monte-Carlo runs

## 4.2 Linear Fractional Transformation

The uncertain nonlinear simulation model describes a wide variation of dynamic behavior with multiple sources of parametric uncertainty perturbation. To use this model for robust control design and analysis with existing design and analysis tools from robust control theory, the uncertain nonlinear model needs to be linearized with the parametric uncertainties included in a Linear Fractional Transformation (LFT) model representation (Figure 4.4). This is the most general form for $H_\infty$ controller synthesis and robustness analysis using structured singular value. This section introduces new software tools to linearize the uncertain nonlinear simulation model developed for obtaining a physically meaningful LFT model.

The LFT is a matrix function that is a very powerful approach to realization of an uncertain model which separates what is known from what is unknown in a feedback-like connection. This is comparable to the realization of a state-space system where it provides

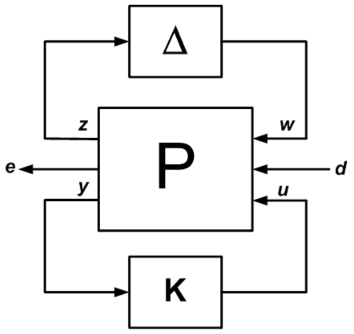

Figure 4.4: General LFT representation for robust control synthesis and analysis

an easier manipulation and computation of a linear system, except that the LFT model is capable of handling an uncertain system. For example, consider the uncertain system shown in Figure 4.5, where $M$ represents the known part of the uncertain system and $\Delta$ represents the uncertainty in the uncertain system, it can be written as an upper LFT:

$$\begin{aligned} y &= F_u(M, \Delta) \\ &= (M_{22} + M_{21}\Delta(I - M_{11}\Delta)^{-1}M_{12})u \end{aligned}$$

where $M$ matrix is compatibly partitioned with the $\Delta$ matrix for a given input and output signals of the system. The matrix $M$ can be partitioned into smaller sub-matrices (as shown

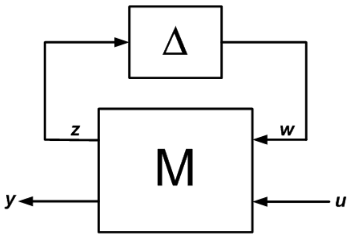

Figure 4.5: M-Δ interconnection

in Figure 4.6) according to the following input and output state equations:

$$\begin{aligned} \dot{x} &= Ax + B_1 w + B_2 u \\ z &= C_1 x + D_{11} w + D_{12} u \\ y &= C_2 x + D_{21} w + D_{22} u \end{aligned}$$

The $M$ matrix above is partitioned to:

$$\begin{aligned} M_{11} &= \begin{bmatrix} A & B_1 \\ C_1 & D_{11} \end{bmatrix} \\ M_{12} &= \begin{bmatrix} B_2 \\ D_{12} \end{bmatrix} \\ M_{21} &= \begin{bmatrix} C_2 & D_{21} \end{bmatrix} \\ M_{22} &= D_{22} \end{aligned}$$

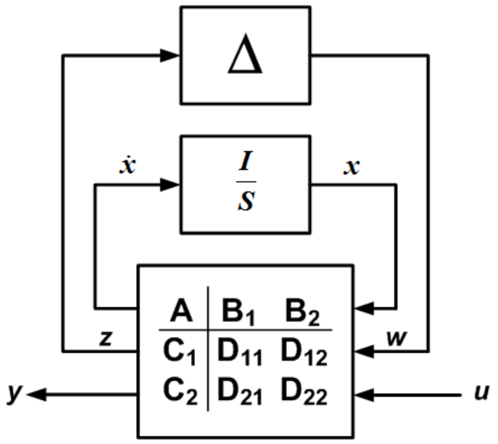

Figure 4.6: $M$-$\Delta$ structure with $M$ partitioned

### 4.2.1 Method of LFT Model Realization

A realization of the LFT model involves the extraction or derivation of the $M$ and $\Delta$ matrices from the uncertain nonlinear simulation model. Various papers [38, 40–45] have been published to address the topic for the LFT model realization. However, this area of research still remain as an open and unsolved problem as the key issue of the LFT modeling still remain in getting a minimum size $\Delta$ description for the system. None of the methods presented is able to guarantee a model with an unique minimum-order LFT model and this problem is not part of this research work. The main focus is to provide a systematic approach for LFT model realization that exploits on the advantage of the integrated framework in Matlab/Simulink environment.

An LFRT toolbox in [46,47] is a toolbox that works with Matlab/Simulink environment and requires uncertain Simulink blocks to be modeled using a special Simulink block object representations. This requires additional effort to convert the existing uncertain nonlinear simulation models into the Linear Fractional Representation (LFR) object representation. The approach taken here is similar, though uses the existing uncertain nonlinear simulation model and the tools from the Matlab Robust Control Toolbox for the LFT model realization. The principle of this method is based on linearization of the uncertain nonlinear Simulink model which is very similar to the approach taken by [48–50] and the block linearize commands in Simulink. This method of LFT model realization from the uncertain nonlinear model is called *ulinearize*.

### 4.2.2 ulinearize Principles and Procedure

The ulinearize procedure performs linearization of an uncertain nonlinear Simulink model at a specific operating point. The inputs to ulinearize are the name of the uncertain nonlinear Simulink model that is to be linearized and an operating point object in which the linearization is to be performed. This procedure relies on the Matlab ***linearize*** function used for linearizing nonlinear Simulink model.

The ulinearize function performs the following:

- Finds all the USS System blocks in the Simulink model and creates an input and output for the linearization by breaking the loop associated with the USS blocks. The output of the USS System block will be an input for the linearization and the input to the USS System block will be the linearization output (shown in Figure 4.7).

- Finds and creates input and output linearization Input-Output (IO) objects which associates an input signal with each of the inport block and output signal with each of the outport block.

- Creates a block diagonal $\Delta$ matrix with each uncertainty object on the diagonal of $\Delta$ matrix and associates each of the input and output linearization IO that has been

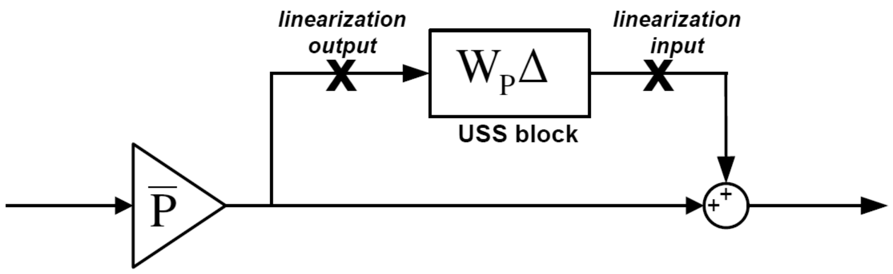

Figure 4.7: Creating linearization input and output at the USS System block (Equation 4.1)

created.

- Linearizes of all the IO blocks that have been created previously for the linearization using the specified operation point object. This will generate a state-space model that contains all the inputs and outputs of the IO.
- Connects the $\Delta$ matrix and state-space model obtained from linearization via a linear fractional transformation to generate an uncertain linear system.

A flow chart for the ulinearize function procedure is given in Figure 4.8.

### 4.2.3 Limitations of ulinearize

Linearization of the uncertain nonlinear model is a simple and intuitive approach for LFT realization to generate physically meaningful LFT representations of the uncertain system. A drawback of this approach is that it tends to produce $\Delta$ matrix with many repeated parametric uncertain parameters. This is due to each of the uncertainty is "pulled-out" and modeled individually even if they are the same parametric uncertainty that appear in multiple locations in the nonlinear simulation model. Although this can be avoided by smart manipulation of the modeling block diagrams, it becomes difficult with very complex system. Unnecessary repeated uncertain parameters are undesirable as they increase the computation effort required for robust analysis and may lead to a more conservative analysis results.

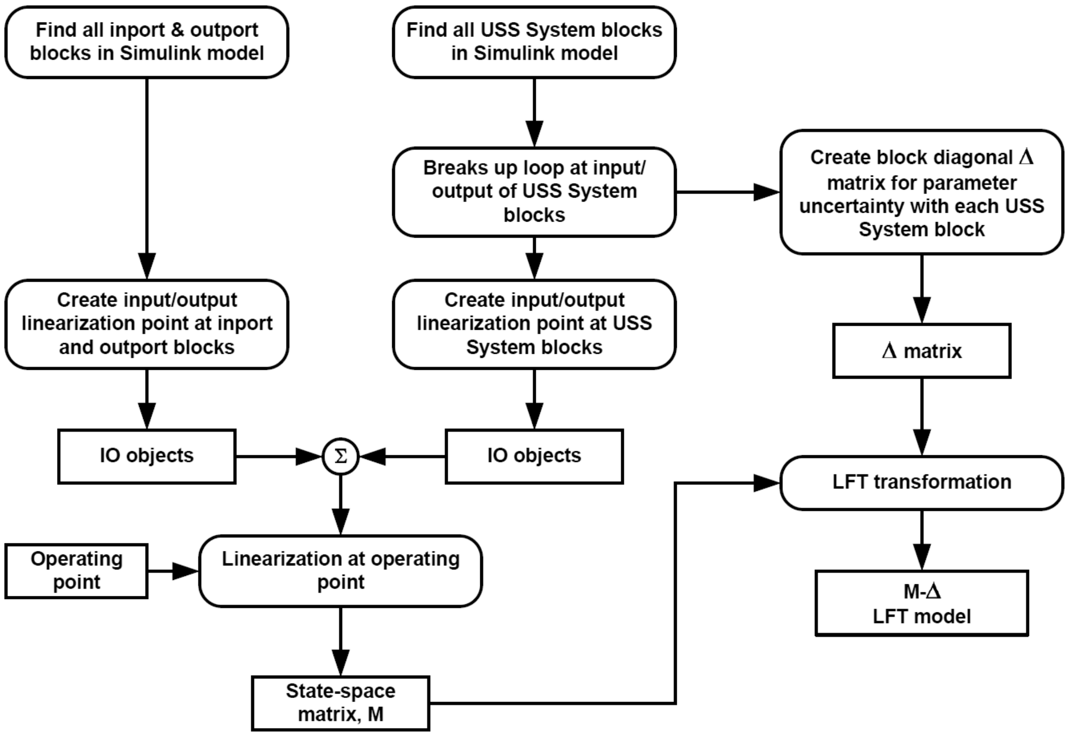
Find all inport & outport blocks in Simulink model
Find all USS System blocks in Simulink model
Breaks up loop at input/ output of USS System blocks
Create block diagonal Δ matrix for parameter uncertainty with each USS System block
Create input/output linearization point at inport and outport blocks
Create input/output linearization point at USS System blocks
Δ matrix
IO objects
Σ
IO objects
LFT transformation
Operating point
Linearization at operating point
M-Δ LFT model
State-space matrix, M

Figure 4.8: Flow chart of ulinearize function procedure

The parametric uncertainties in the nonlinear simulation model have to be implemented using either a multiplicative or an inverse multiplicative uncertainty that has a multiplication with an input signal. Any constant uncertainty has to be manipulated so that it has a multiplication with an input signal. Linearization of the uncertain nonlinear simulation model requires breaking of the loop associated with the USS block to form an input/output pair for linearization. During the linearization, an exogenous signal is required from the input to output point of the linearization so that the transfer function seen by the uncertain parameter can be computed. Hence, for a constant uncertainty block that is not multiplied with an input signal, the numerical linearization will not work and no input to output transfer function relationship can be obtained. This will result in the constant block uncertain parameter not showing up in the LFT model realization. The LFRT toolbox from [46] has the same limitation since it makes use of Matlab ***linmod*** function for linearization in the LFT model realization.

In addition, even if an input multiplication signal is available at the USS System block, the input signal must be non-zero. This may seem trivial but it can happen when the input signal to the USS System block is from a state variable signal that has been trimmed to zero with zero initial condition. However this problem can be easily overcome by setting a very small initial condition on the state ($10^{-5}$ times of an unit value of the state variable) so that the linearization will be performed correctly. The trimmed state variable will not significantly differ from a perfect zero initial condition.

### 4.2.4 Effect of Trim Point

In the realization of LFT model using ulinearize, numerical linearization of uncertain nonlinear model is performed using specific operating point (as shown in Figure 4.9). To find the operating point, a trim operating condition is first obtained through trimming of the nominal nonlinear model at the desired trim operating condition. Subsequently, the structure of the operating point for the nonlinear simulation model is created. With the trim operating condition and the structure of the operating point, the operating point object for the trim condition is created for the LFT realization. Hence, any perturbation of uncertainties in the nonlinear model will affect the trim point and operating point and this can be important as it affects the validity of the LFT model obtained using this approach.

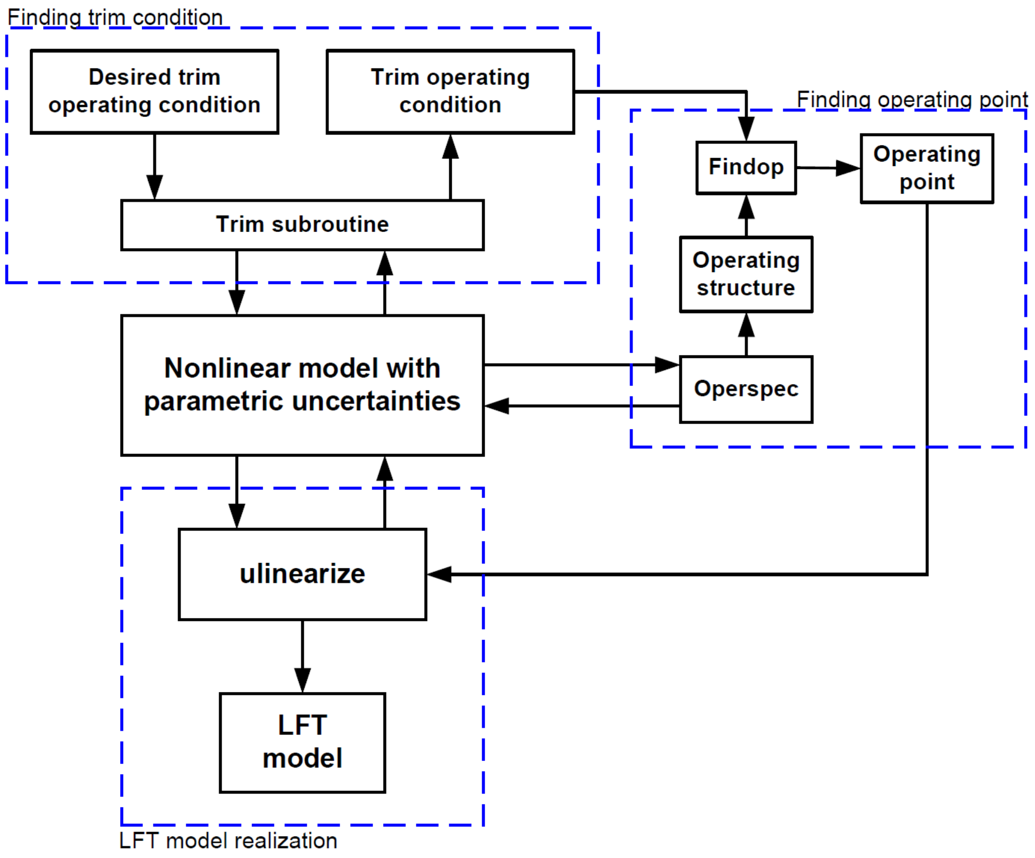

Figure 4.9: Procedure in obtaining operating point for ulinearize

## 4.3 UAV LFT Model Realization

A comprehensive list of parametric uncertainties are modeled into the LFT model realization. The list of parametric uncertainties (in Appendix Table C.2) included in the nonlinear UAV simulation model are based on the following experimental data:

- Moment of inertia data (Appendix Table A.2)
- Flight test identified aerodynamics coefficients (Appendix Table C.1)
- Simulator tuned aerodynamics coefficients (Appendix Table A.1) with ±5 % uncertainty variation from these values.
- Propulsion system coefficients (Appendix Table A.3) with ±5 % uncertainty variation from these values.

The ulinearize algorithm is applied to the nonlinear simulation model with parametric uncertainties using trim operating point condition in Appendix Table B.1. In the uncertain linearization setup, the angular rate velocity integrator initial condition (refer to Appendix Figure C.2) is set to a very small numerical value ($10^{-9}$) so that angular rates $p$, $q$ and $r$ are not zero. This is important since these angular rates are fed back to the input of moment of inertia uncertainty blocks. As previously discussed, a zero input to a USS block will result in a zero input and give a zero input to output linearization relationship. This will result in the parametric uncertainties not showing up in the realized LFT model.

Another modification was made to Simulink derivative block linearization time constant to a large number ($10^{30}$) instead of using the default value of $\infty$. This change was made to the $\dot{\alpha}$ derivative block from which the derivative of $\alpha$ signal is obtained. The $\dot{\alpha}$ signal is used as the input to the $C_{L_{\dot{\alpha}}}$ and $c_{m_{\dot{\alpha}}}$ parametric uncertainty blocks. The reason for this modification is that if the linearization time constant is infinity, this will cause the $\dot{\alpha}$ signal to be zero and no $C_{L_{\dot{\alpha}}}$ and $c_{m_{\dot{\alpha}}}$ parametric uncertainty will be extracted from the uncertain linearization. Using a large non-infinity time constant is able to get around this problem. The drawback of using a non-infinity linearization time constant is that the LFT model has an additional state contributed by the derivative block. However, this does not affect the overall linearized system dynamics and can be simply eliminated from the LFT model.

A LFT model with a $M$ matrix of size 66 x 63 (Figure 4.10) and a diagonal $\Delta$ matrix of size 46 x 46 (Appendix Table C.3) were obtained. The reason why the diagonal $\Delta$ matrix has such a large dimension (46) much higher than the total number of different parametric uncertainties (34) is because $C_{L_{minD}}$, $I_{xx}$, $I_{yy}$, $I_{zz}$ and $I_{xz}$ parameters were used in multiple locations in the nonlinear simulation model. The *ulinearize* realization treats each of them as a separate individual uncertainty leading to repetition of same uncertain parameter. The state equations for the realized LFT model are given by:

$$\begin{aligned}
\dot{x}_f &= A_f x_f + B_{1_f} w_f + B_{2_f} u_f \\
z_f &= C_{1_f} x_f + D_{11_f} w_f + D_{12_f} u_f \\
y_f &= C_{2_f} x_f + D_{21_f} w_f + D_{22_f} u_f
\end{aligned}$$

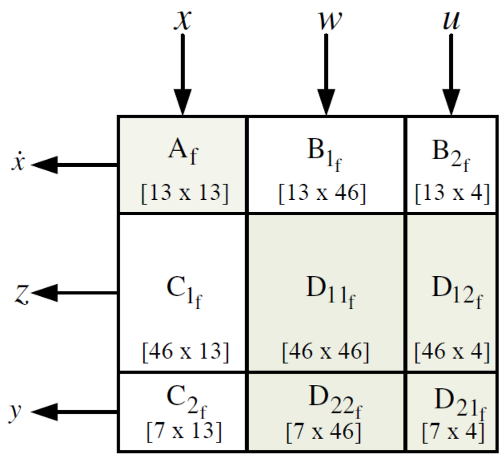

Figure 4.10: M matrix dimension obtained for UAV LFT model

### 4.3.1 Uncertain System Worst-case Gain

The LFT model obtained represents an uncertain system with the known part grouped into $M$ matrix and uncertain part in a $\Delta$ matrix with a feedback interconnection structure as shown in Figure 4.5. The gain of the uncertain system depends on the values of the uncertainty in the $\Delta$ matrix. An important question to asked about the system gain resulted from uncertainties variation is "What is the maximum gain of the system over all allowable values of the uncertainties in the $\Delta$ matrix?" The maximum gain and associated uncertainty perturbations can be used as the worst-case gain condition for a closed-loop uncertain system stability analysis. The determination of the maximum gain of uncertain system over all allowable uncertainty perturbations is known as worst-case gain analysis. The objective of the worst-case gain analysis is to find the values of the uncertain parameters that give the worst-case (maximum) gain of the system. The measure of the size for the maximum gain is the maximum singular value of the system over the frequency response, which is the $H_\infty$ norm.

A worst-case gain analysis was performed on the open-loop LFT model to find the worst-case gain condition over the frequency range of interest, which is between 1 to 30 rad/s using ***wcgain*** function from Robust Control Toolbox. A pointwise worst-case gain computation was performed. Figure 4.11 shows the result of the worst-case gain bounds across the frequency. The exact worst-case gain condition can be assumed to be given by either the lower or upper bound value since these two bounds are almost the same. The maximum singular value at each frequency point for the nominal system is also plotted to show the deviation of worst-case gain condition from the nominal system due to uncertain parameters variation in the LFT model. The worst-case gain result obtained here are used to evaluate the LFT model realization accuracy in next section.

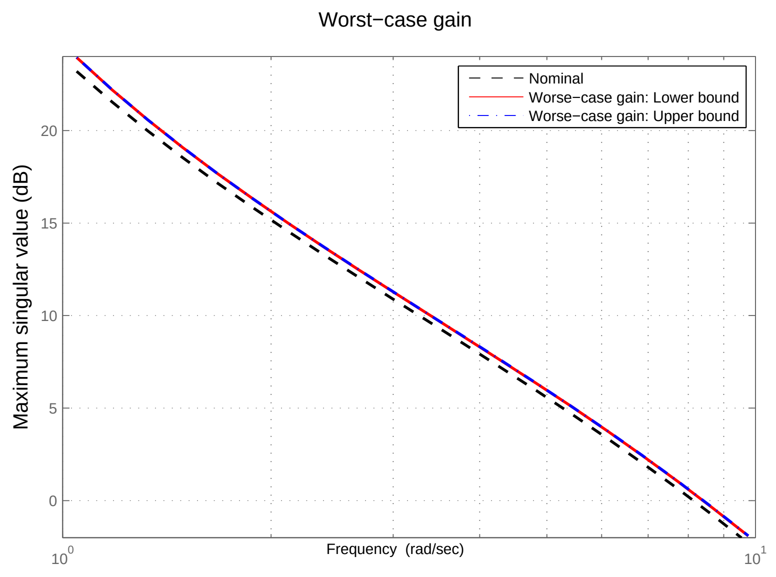

Figure 4.11: Worst-case gain analysis of full UAV LFT model

### 4.3.2 Accuracy of LFT Model Realization

The accuracy of the LFT model obtained is evaluated by comparing its output responses with the uncertain nonlinear simulation model responses. A same set of parametric uncertainty perturbations ($\delta_i$) is applied to both the LFT model and the uncertain nonlinear simulation model and the output responses of the two systems are compared. Since this comparison involves a linear model (LFT model) and a nonlinear model, there will be differences in the output responses due to the trim solution. To eliminate the effect of the linearization in the comparison, a different approach shown in Figure 4.12 is taken.

In this approach, a nonlinear model is first obtained from the uncertain nonlinear simu-

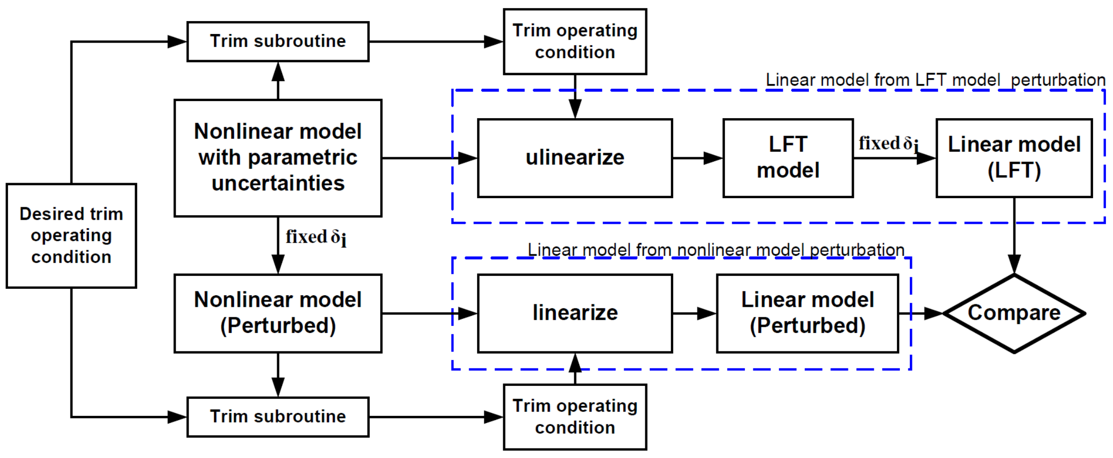
Trim subroutine
Trim operating condition
Linear model from LFT model perturbation
Nonlinear model with parametric uncertainties
ulinearize
LFT model
fixed δi
Linear model (LFT)
Desired trim operating condition
fixed δi
Linear model from nonlinear model perturbation
Nonlinear model (Perturbed)
linearize
Linear model (Perturbed)
Compare
Trim subroutine
Trim operating condition

Figure 4.12: Setup for comparing accuracy of LFT model with uncertain nonlinear simulation model

lation model with the parametric uncertainties fixed to the set of uncertainty perturbation $\delta_i$. Next, a different trim operating condition is obtained from the perturbed nonlinear model using the same desired trim operating condition before linearizing the model since uncertainty perturbation changes the trim condition which has been discussed in Section 4.2.4. The perturbed linear model obtained is used for comparison with the linear model (LFT) obtained by fixing the $\Delta$ matrix to the same set of parametric uncertainties $\delta_i$.

The approach of using the linearized model instead of the nonlinear model for comparison is only valid if the linearized model is able to represent the nonlinear model well and this has been verified in Section 3.1.1.1. An advantage of using the ulinearize for the LFT realization is shown here as it is easy to relate the physical parametric uncertainties in the LFT model and the uncertain nonlinear simulation model. This allows easy comparison between the models.

The set of uncertain perturbation $\delta_i$ chosen is based on the the worst-case gain analysis in Section 4.3.1. This is to ensure a worst-case uncertainty perturbation condition is applied to drive the uncertain system to the worst-case condition for testing the validity and accuracy of the LFT model realization approach. The set of worst-case uncertainties (Appendix Table C.4) at 5 rad/s is chosen for this analysis so that it is consistent with the flight test identification data collect at this frequency range that was used to update the uncertain nonlinear model.

Figures 4.13 and 4.14 show the frequency and time response comparisons for angle of attack, sideslip, roll and pitch angle outputs from linear (LFT) model and linear (Perturbed) model using the same set of worst-case gain uncertainty variation $\delta_i$ condition. For the time response simulation, doublet signals are applied to elevator, aileron and rudder control inputs. In each of the plots, the nominal system response is include as a baseline reference. Figures 4.13 and 4.14 shows that the linear (Perturbed) model and linear (LFT) model responses are well matched. Hence the uncertain LFT model is able to predict the response of the uncertain nonlinear simulation under the worst-case gain condition and this shows that ulinearize is able to provide an accurate LFT model realization from the uncertain nonlinear simulation model.

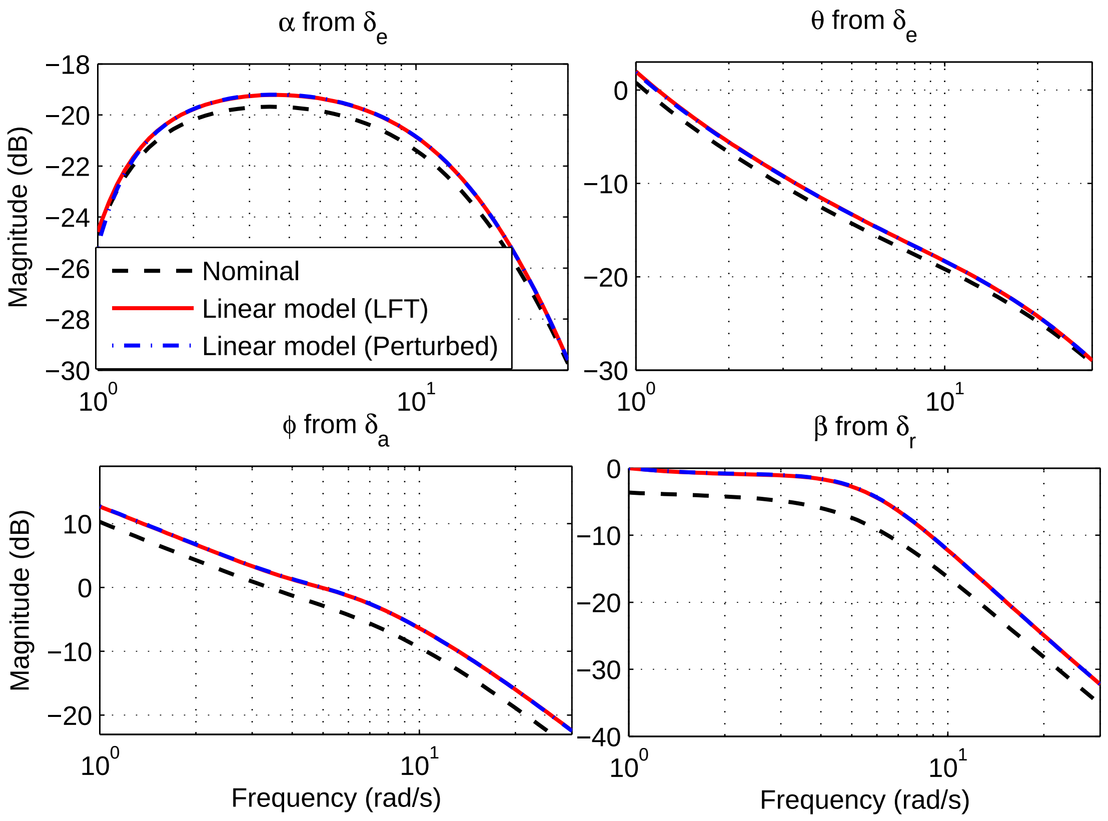

Figure 4.13: Frequency domain comparison for LFT model realization accuracy

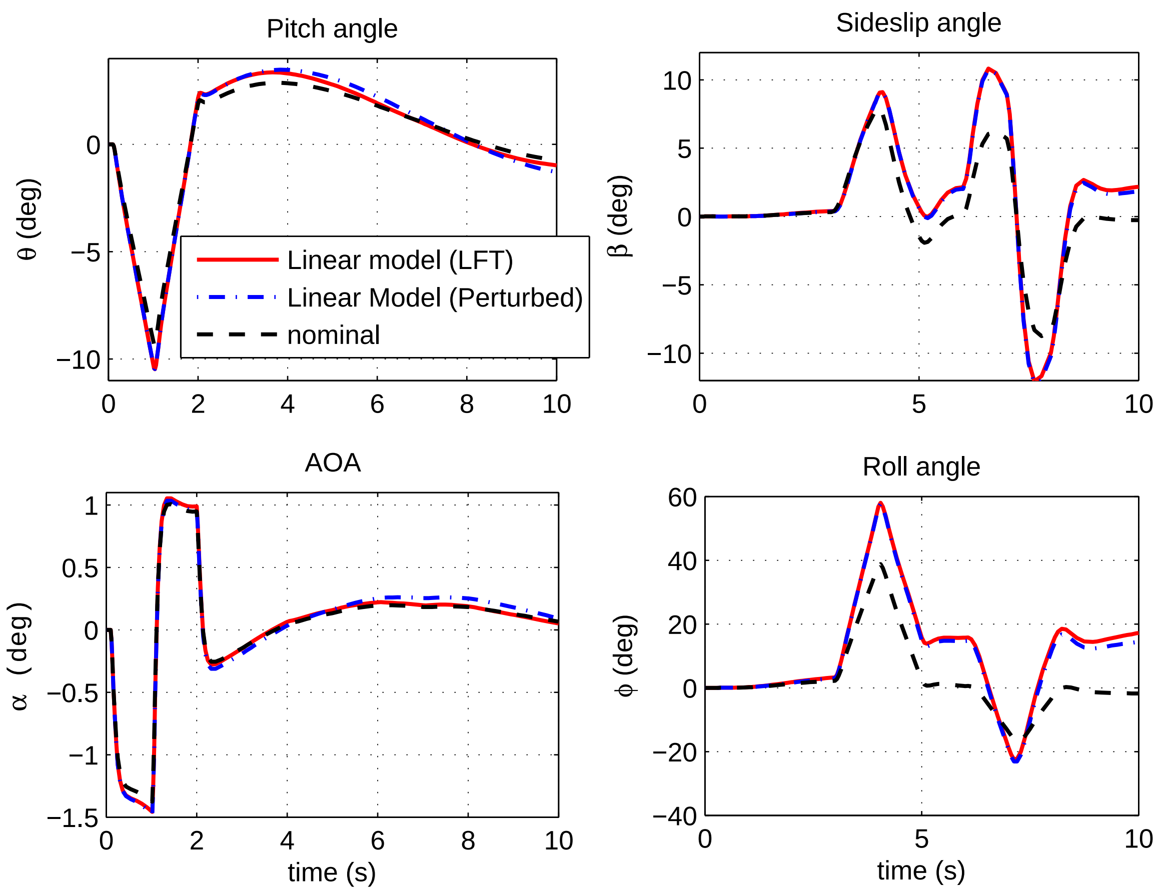

Figure 4.14: Time domain comparison for LFT model realization accuracy

### 4.3.3 Decoupled LFT model

In Section 3.1.1.1, negligible cross-coupling assumption has been made and verified for decoupling linearized aircraft dynamics into longitudinal and lateral-directional modes. However, with the presence of parametric uncertainties, the validity of this assumption may not hold.

The LFT model obtained from ulinearize in the previous section contains both longitudinal and lateral-directional modes. To decouple the LFT model into longitudinal and lateral-directional modes, the same approach to decoupling used in Section 3.1.1.2 is used. This is done by extracting the relevant columns and rows required by each mode from $A_f$, $B_{1_f}$, $B_{2_f}$, $C_{1_f}$, $D_{12_f}$, $C_{2_f}$, $D_{21_f}$ and $D_{22_f}$ matrices (Figure 4.10) of the LFT model. For the input $w$ and output $z$ to the diagonal $\Delta$ matrix, full size $D_{11_f}$ matrix is used since it is not known how each of these uncertainties is relevant to each of the mode and there might be cross-coupling contribution by these uncertainties.

To reduce any redundant uncertain parameters in the decoupled longitudinal and lateral models $\Delta$ matrices, each uncertain parameter of the decoupled uncertain longitudinal and lateral models is evaluated to check if it could be eliminated. This is similar to model reduction process where states that have insignificant effect to the overall system can be eliminated and simplified to a lower order system. Uncertain parameters with strong cross-couplings will not be eliminated in this process. The simplification of the uncertain model is done using the ***simplify*** function from the Robust Control Toolbox.

The longitudinal model obtained is:

$$\begin{aligned}
\dot{x}_{lon} &= A_{lon}x_{lon} + B_{1_{lon}}w_{lon} + B_{2_{lon}}u_{lon} \\
z_{lon} &= C_{1_{lon}}x_{lon} + D_{11_{lon}}w_{lon} + D_{12_{lon}}u_{lon} \\
y_{lon} &= C_{2_{lon}}x_{lon} + D_{21_{lon}}wlon + D_{22_{lon}}u_{lon}
\end{aligned}$$

and the lateral model obtained is:

$$\begin{aligned}
\dot{x}_{lat} &= A_{lat}x_{lat} + B_{1_{lat}}w_{lat} + B_{2_{lat}}u_{lat} \\
z_{lat} &= C_{1_{lat}}x_{lat} + D_{11_{lat}}w_{lat} + D_{12_{lat}}u_{lat} \qquad (4.3) \\
y_{lat} &= C_{2_{lat}}x_{lat} + D_{21_{lat}}w_{lat} + D_{22_{lat}}u_{lat}
\end{aligned}$$

Table 4.1 shows the details of the uncertain parameters that have been removed or retained in each of the decoupled models. The dimension of the diagonal uncertain matrix obtained from the decoupled models after simplification is much smaller than the initial full $\Delta$ matrix that was used. In the longitudinal model, 21 of the uncertainties, which are mainly related to the roll and yaw moment, have been eliminated. A similar result is obtained for the lateral model where 22 of the uncertainties eliminated are mainly from pitch moment and lift force. Intuitively, this is understandable since most of the uncertainties eliminated from longitudinal model are related to the lateral mode and vice versa for uncertainties that are eliminated from the lateral model.

Using the worst-case gain analysis result from Section 4.3.1, uncertainties variations for worst-case gain condition in Appendix Table C.4 are applied to the full and decoupled models. A comparison between the full and decoupled model responses at worst-case gain condition using angle of attack, sideslip, roll and pitch angle output responses was performed. Figure 4.15 shows that the two systems output responses are nearly identical. This shows that uncertainty perturbations do not induce a significant cross-coupling effects to the coupled and decoupled models output responses at this operating point with the given size of worst-case gain parametric uncertainties used.

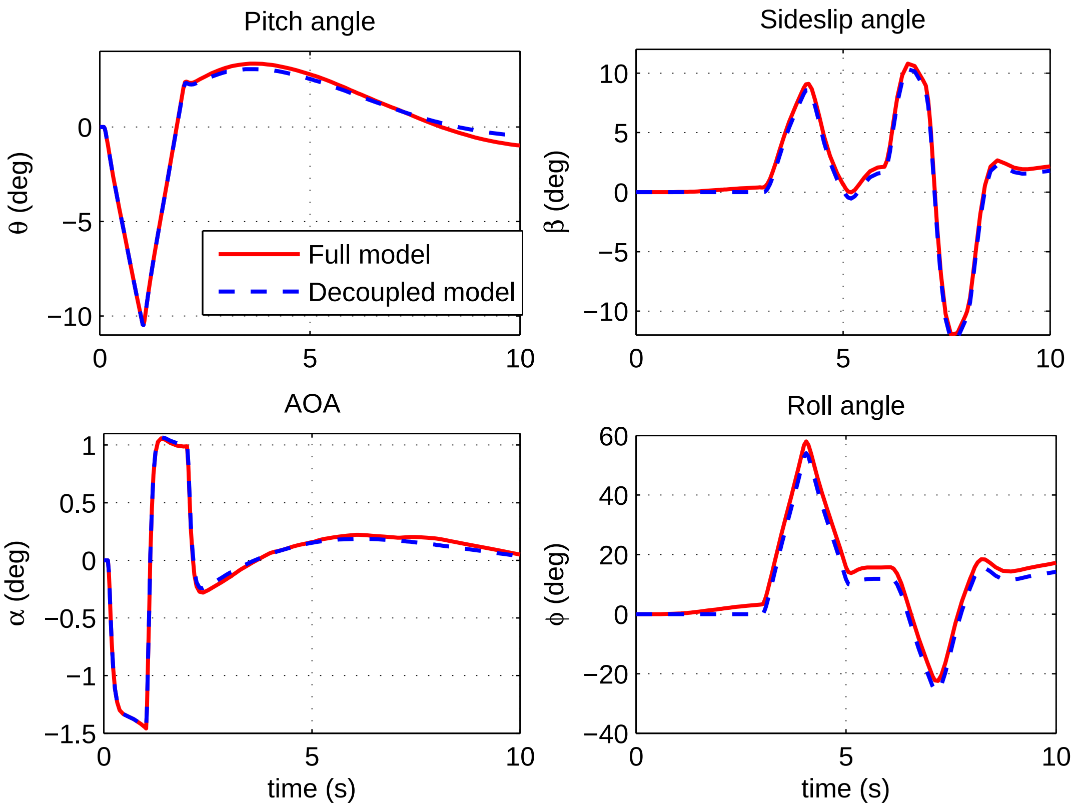

Figure 4.15: Full model vs decoupled model comparison

## 4.4 Uncertain Model Simplification

The LFT model realization from the previous section consists of detailed and accurate model description of the uncertain nonlinear model at specific operating point. To apply this uncertain model for controller synthesis, a simple representation of the model uncertainty is desirable so that the synthesized controller obtained will not be too conservative [21]. Two model uncertainty simplification approaches are presented and applied to the lateral LFT model. The simplified LFT model obtained is used for controller synthesis in the next chapter.

### 4.4.1 Uncertain Parameters Sensitivity Analysis

A sensitivity analysis of the parameter uncertainties in the LFT model can help to identify which of the uncertain parameters will result in a significant different output response from the nominal system response. This analysis can help to reduce the number of parametric uncertainties in the LFT model since less sensitive uncertain parameters can be eliminated with minimum effect on the system response. The sensitivity of the uncertain parameters is determined using worst-case analysis described previously in Section 4.3.1.

From the decoupled lateral LFT model in Equation 4.3, a two-state lateral LFT model is extracted. This LFT model is of the same form as the parameterized state-space model used for parameter identification in Equation 3.8, except that it has addition $w$ input and $z$ output to a block diagonal uncertainty matrix. The two-state lateral LFT model is given by:

$$\begin{aligned}
\dot{x}_{lat2s} &= A_{lat2s}x_{lat2s} + B_{1_{lat2s}}w_{lat2s} + B_{2_{lat2s}}u_{lat2s} \\
z_{lat2s} &= C_{1_{lat2s}}x_{lat2s} + D_{11_{lat2s}}w_{lat2s} + D_{12_{lat2s}}u_{lat2s} \\
y_{lat2s} &= C_{2_{lat2s}}x_{lat2s} + D_{21_{lat2s}}w_{lat2s} + D_{22_{lat2s}}u_{lat2s} \\
w_{lat2s} &= diag\{\delta_i^{lat}\}z_{lat2s} \quad \forall\ i = 1\ to\ 18\ and\ -1 \le \delta_i^{lat} \le 1
\end{aligned} \tag{4.4}$$

where

$$x_{lat2s} = \begin{bmatrix} p \\ r \end{bmatrix} \qquad u_{lat2s} = \begin{bmatrix} \delta_a \\ \delta_r \end{bmatrix} \qquad y_{lat2s} = \begin{bmatrix} p \\ r \end{bmatrix}$$

$$\begin{aligned}
\delta_1^{lat} &= cl_{\delta a_\triangle} \quad \delta_2^{lat} = cl_{\delta r_\triangle} \quad \delta_3^{lat} = cl_{p_\triangle} \quad \delta_4^{lat} = cl_{r_\triangle} \\
\delta_5^{lat} &= cn_{\delta a_\triangle} \quad \delta_6^{lat} = cn_{\delta r_\triangle} \quad \delta_7^{lat} = cn_{p_\triangle} \quad \delta_8^{lat} = cn_{r_\triangle} \\
\delta_{9,10}^{lat} &= I_{xx_\triangle} \quad \delta_{11,12,13,14}^{lat} = I_{xz_\triangle} \quad \delta_{15,16}^{lat} = I_{yy_\triangle} \quad \delta_{17,18}^{lat} = I_{zz_\triangle}
\end{aligned}$$

This can be written in a compact LFT form of:

$$G_{lat2s_\Delta} \quad = \quad F_u(M_{lat2s}, \Delta_{lat2s}) \tag{4.5}$$

with

$$M_{lat2s} = \begin{bmatrix} A_{lat2s} & B_{1_{lat2s}} & B_{2_{lat2s}} \\ C_{1_{lat2s}} & D_{11_{lat2s}} & D_{12_{lat2s}} \\ C_{2_{lat2s}} & D_{21_{lat2s}} & D_{22_{lat2s}} \end{bmatrix} \qquad and \qquad \Delta_{lat2s} = diag\left\{\delta_i^{lat}\right\} \;\; \forall\, i = 1 \; to \; 18$$

The lateral LFT model has a total of 18 uncertain parameters, of which 6 of them are repeated. Applying the worst-case gain analysis, the sensitivity for each of the uncertain parameters contribution to the worst-case gain is computed at each frequency point across the frequency range. Figure 4.16 shows the sensitivity values obtained from the worst-case gain analysis of the lateral LFT model for each of the uncertain parameter across the frequency range. The plot in Figure 4.16 shows that three of the different parametric uncertainties, $I_{xz_\Delta}$ ($\delta^{lat}_{11,12,13,14}$), $I_{yy_\Delta}$ ($\delta^{lat}_{15,16}$) and $cl_{\delta r_\Delta}$ ($\delta^{lat}_{2}$), have very small sensitivity values. This means that these uncertain parameters have very little contribution to the worst-case gain and removing them (setting them to be zero) will not affect the worst-case gain of the lateral LFT model significantly. Hence $\delta^{lat}_{2,11,12,13,14,15,16}$ are set to zero and Figure 4.17 shows the result of the worst-case gain for the lateral LFT model with $\delta^{lat}_{2,11,12,13,14,15,16}$ set to zero. The worst case gain obtained is very close to the full uncertain lateral LFT model with little reduction in the worst-case gain due to simplification of the uncertain model. The tradeoff of simplifying and removing the parametric uncertainties from the uncertain lateral model can be clearly seen from Figure 4.17 where the worst-case gain decreases from upper bound of full uncertain model (no parametric uncertainty removed) to a minimum bound given by the maximum singular value of the nominal model (all parametric uncertainties are removed). However, over simplification of the uncertain model by removing too many of sensitive uncertainties is not desirable as this will decrease the fidelity of the simplified uncertain model in predicting and representing the actual effect of uncertainty in the LFT model.

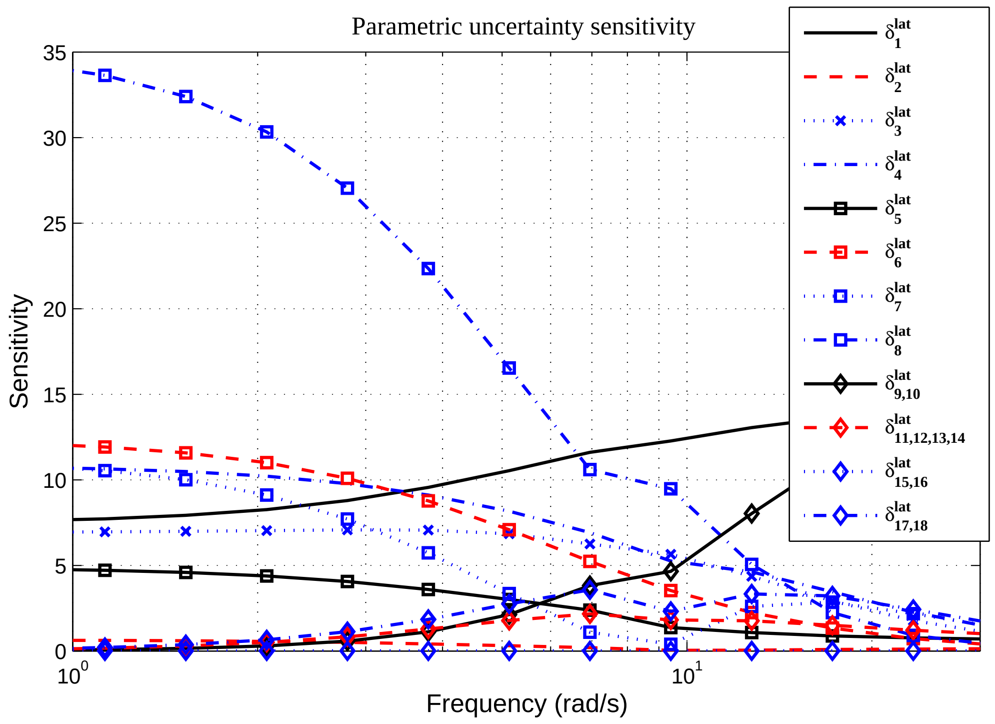

Figure 4.16: Parametric uncertainties sensitivity across frequency

### 4.4.2 Frequency Domain Uncertainty Representation

Beside using elimination method to simplify the LFT model based on uncertain parameters sensitivity analysis, another approach for simplifying the LFT model is to approximate the parametric uncertainties with an unmodeled Linear Time-Invariant (LTI) dynamic uncertainty. This is done by overbounding the real uncertainty perturbation of -1 $\leq \Delta \leq$ 1 with a single complex perturbation of $|\Delta(j\omega)| \leq 1$. The disadvantage of this approach is that the uncertainty model may be more conservative as the complex uncertainty perturbation includes possible plants that might not be in the original set of plants from the real parametric uncertainty model. However, if there are several real parametric uncertainties in the model, the conservatism is often reduced by lumping these real parametric uncertainty perturbations into a single complex perturbation as several real uncertainty perturbations region is often quite “disc-shaped” which is described by a single complex uncertainty region [37]. A commonly used approach of lumping the real parametric uncertainty perturbations to-

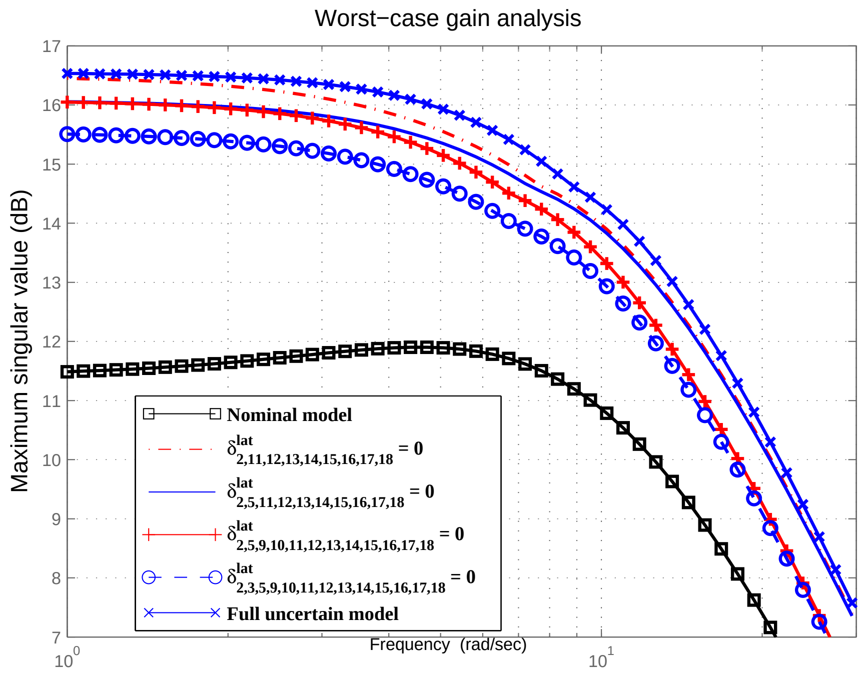

Figure 4.17: Worst-case gain analysis for different number of parametric uncertainty reduction

gether is to overbound the real parametric uncertainty perturbation region using a single complex uncertainty perturbation.

#### 4.4.2.1 Overbounding using Unmodeled Liner Time Invariant Dynamic Uncertainty Model

The tradeoff between uncertainty conservatism and closed-loop system performance motivates the desire of deriving the tightest overbound in replacing the real parametric uncertainties using single complex uncertainty model. This has been described by problem statement of computing optimal uncertainty model using convex optimization in [51–53] where frequency domain data from different measurements or plants are used for computation of tight uncertainty model bounds for robust control design purpose. The computation of tight overbound from frequency domain data has been shown to reduce to a Linear Matrix Inequalities (LMI) feasibility problem in [51] where the objective is to simultaneously search for both a nominal model and uncertainty weighting bound that give optimal uncertain model with the tightest bound on the data set.

To apply the optimal overbounding technique on the lateral model given in Equation 4.5, a family of models is generated from the uncertain lateral model by random sampling of the parametric uncertainties ($\Delta_{lat2s}$) so that the family of models covers a wide range of model responses region described by the real parametric uncertain model. Figure 4.18(a) shows a frequency domain representation using Nyquist plot for a family of models obtained from random sampling of the parametric uncertainties. At each of the frequency point in Figure 4.18(a), the family of models covers a complex number region due to different parametric uncertainties variations in $\Delta_{lat2s}$. Figure 4.18(b) shows an example for the concept of overbounding at $\omega = 1.0$ rad/s frequency point (corresponds to $\omega = 1.0$ rad/s in Figure 4.18(a)) in the complex plane. The unshaded region bounded by dashed line described the region with all possible real parametric uncertainties variations from the nominal model (red '**x**') at a specific frequency point. Each of the blue '**x**' in the unshaded region is a random sampled model from the parametric uncertain model, and the collection of these sampled models is a family of models. The number of random sampled models should be large enough so that it provides a good coverage of the entire unshaded region to be overbounded.

The red circle represents the tightest disc shape overbound that can be computed with a given nominal model to enclose the entire unshaded region with the objective of achieving the smallest shaded region. The shaded region represents the models that are not in the original set of models from the real parametric uncertainty model but has been included in the overbonding process. The addition of models in the shaded region adds conservatism to the complex uncertainty model obtained from overbounding. The disc radius $W_k$ gives the optimal frequency weighting function required to tightly overbound the family of models.

The nominal model used in the lateral LFT model is obtained from the ulinearize process and this has to be fixed as a constraint in the determination of the tightest overbound weighting function. This is to ensure that the nominal model used is a feasible trim model within the desired operating point. In addition, fixing the nominal model used simplifies the optimization for getting the tightest overbound and provides physically practical uncertain model in this application. Computation of the optimal overbound weighting function $W_k$ is solved using LMI feasibility problem at each of the frequency point [53].

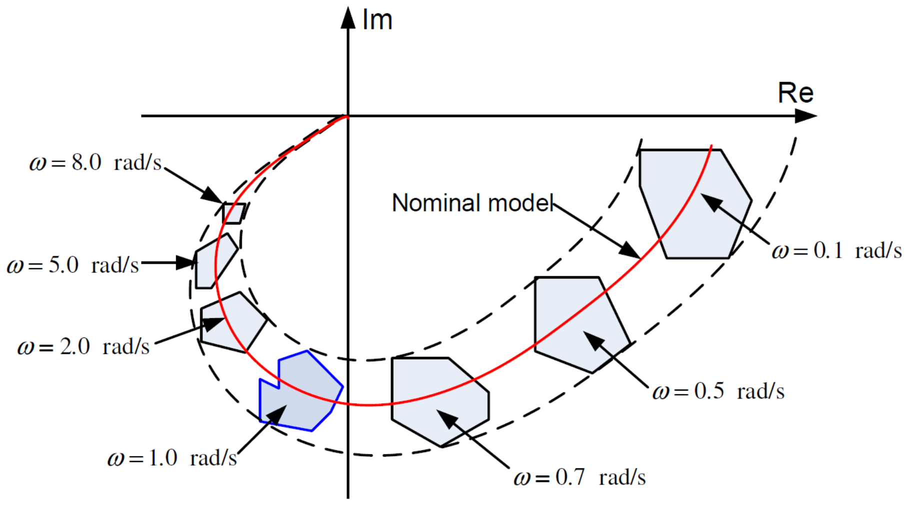

(a) Nyquist plot of uncertainty regions at different frequencies

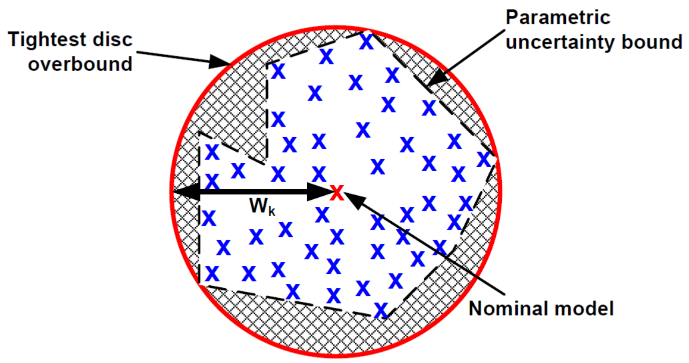

(b) Disc overbounding at $\omega = 1.0$ rad/s frequency point

Figure 4.18: Complex plane uncertainty region and disc overbound

Consider an input multiplicative unmodeled Linear Time Invariant (LTI) dynamic uncertain model used to cover the original set of parametric uncertain model, $G_\Delta$, given by:

$$G_\Delta = G_0(I + W\Delta) : \|\Delta\|_\infty \leq 1$$

where

- $G_0 \in \mathbb{R}^{n\times m}$ is the known nominal model.

- $G_\Delta \in \mathbb{R}^{n\times m}$ has no poles on the imaginary axis.

- $W \in \mathbb{R}^{n\times n}$ is a stable and minimum phase weighting function.

- $\Delta$ is any stable transfer function with magnitude of less than or equal to 1 at each frequency point.

The family of N sampled models to represent the original parametric uncertain model is given by:

$$\underbrace{\{G_1, G_2, \ldots, G_N\}}_{family\ of\ N\ sampled\ models} \quad \subseteq G_\Delta \tag{4.6}$$

Hence the problem becomes finding an optimal overbound on the sampled family of models:

$$\{G_1, G_2, \ldots, G_N\} \subseteq G_0(I + W\Delta),\ \|\Delta\|_\infty \leq 1$$

With $M$ frequency grid points, at each frequency grid point,

$$\{G_1(j\omega_k), G_2(j\omega_k), \ldots, G_N(j\omega_k)\} \subseteq G_0(j\omega_k)(I + W_k(j\omega_k)\Delta),\ \|\Delta\|_\infty \leq 1, \forall k = 1 : M \tag{4.7}$$

For each of the model in the family of $G_N$, there exist a solution for Equation 4.7 with $\|\Delta\|_\infty \leq 1$ if and only if

$$G_0(j\omega_k)W_{i,k}(j\omega_k)W^*_{i,k}(j\omega_k)G^*_0(j\omega_k) - [G_i(j\omega_k) - G_0(j\omega_k)][(G_i(j\omega_k) - G_0(j\omega_k)]^* \geq 0 \tag{4.8}$$

Applying Schur's complement formulae to Equation 4.8, the quadratic matrix inequalities become LMI given by:

$$\begin{bmatrix} G_0(j\omega_k)W_{i,k}(j\omega_k)W^*_{i,k}(j\omega_k)G^*_0(j\omega_k) & G_0(j\omega_k)][(G_i(j\omega_k) - G_0(j\omega_k)] \\ G_0(j\omega_k)[(G_i(j\omega_k) - G_0(j\omega_k)]^* & I \end{bmatrix} \geq 0 \tag{4.9}$$

The weighting $W_{i,k}$ is chosen to be block diagonal given by:

$$W_{i,k}(j\omega_k)W^*_{i,k}(j\omega_k) = \begin{bmatrix} W_1^2 & 0 & 0 & 0 \\ 0 & W_2^2 & 0 & 0 \\ 0 & 0 & \ddots & 0 \\ 0 & 0 & 0 & W_n^2 \end{bmatrix}$$

The optimization to get the optimal weightings is to solve Semi-Definite Programming (SDP) problem with objective function:

$$\min \;\; Tr(W_{i,k}(j\omega_k)W_{i,k}^{*}(j\omega_k)) \tag{4.10}$$

subject to LMI constraint in Equation 4.9 for model $i$ = 1:N and frequency point $k$ = 1:M. More details on the theorem and proofs can be found in [51, 53].

To get a stable and minimum phase weighting function $W$ from the computed optimal weighting function result from Equation 4.10, fitting is done using the optimal weights $W_k$ obtained across the frequency grids. This is done using ***fitmagfrd*** function from Robust Control Toolbox where different weighting function orders can be used for the fitting. The entire process of computing optimal frequency domain bounds and fitting them to a stable, minimum phase weighting function is available in the Robust Control Toolbox's ***ucover*** function.

The overbounding approach to uncertainty model simplification using input multiplicative uncertainty structure can also be applied to output multiplicative and additive uncertainty structures as well. The focused in this thesis is on the multiplicative uncertainty structure as it is found to give a less conservative overbound than for the additive uncertainty structure for parametric uncertain model [21].

#### 4.4.2.2 Verification of Uncertain Lateral Dynamics Model using Optimal Uncertainty Overbound

The optimal overbound computation can be used to compare the size of uncertainty bounds in different model sets. This can aid in determination if one model set overbounds the other set or if one uncertain model has a more conservative uncertainty bound than the other. This will be used here to determine if the lateral dynamic model identified from flight test data in Section 3.5 is overbounded by the lateral LFT model obtained from the uncertain nonlinear simulation model. This verification is important and useful because the lateral LFT model should overbound all the identified models to ensure it contains the actual flight data derived models. Validation of the flight test data is important for the robustness analysis using the uncertain nonlinear simulation model and LFT model to be meaningful in the integrated framework approach. Also, if the lateral LFT model has a big uncertainty bound as compare to the original identified models, this indicates that the LFT model is too conservative and more flight test data are required to update the parametric uncertainty bounds in the nonlinear simulation model in order to tighten the uncertainty bounds.

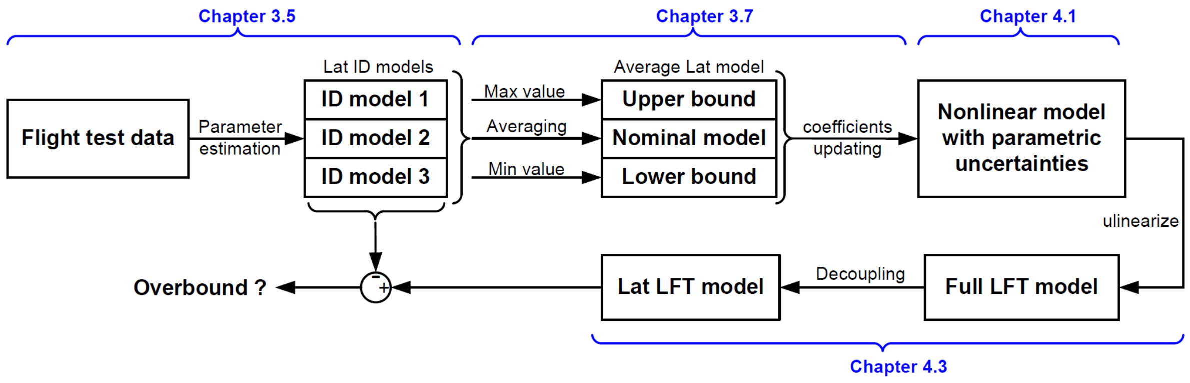

Figure 4.19: Relationship between lateral LFT model and flight test identified models

Figure 4.19 shows the flow chart on the relationship between the lateral LFT model and the flight test identified lateral models used to update the nonlinear simulation model. The objective is to find out if the lateral LFT model obtained from the uncertain nonlinear model overbounds the original set of flight test identified models. To make this comparison, the nominal model used is the same nominal model that was obtained using averaging in Section 3.7.1. Also, from the lateral LFT model in Equation 4.4, the uncertainties $\delta_9^{lat}$ to $\delta_{18}^{lat}$ are fixed at zero so that the lateral LFT model used for comparison contains the exact same number of states and physical parameters as the identified models. A family of 50 models are randomly sampled to represent the lateral LFT model.

The size of uncertainty region at each frequency point away from the nominal model across the frequencies (shown in Figure 4.18(a)) is computed using the ***ucover*** function for an input multiplicative uncertainty model structure to obtain the optimal uncertainty weighting bounds for both the identified lateral models and the family of 50 models sampled from the lateral LFT model. In both of the cases, the same nominal model is used for the optimal uncertainty weighting bounds computation. Figure 4.20 shows the plot of the optimal uncertainty bounds obtained to overbound the aileron and rudder input channels for the identified lateral models and the family of 50 models to represent the lateral LFT model.

From the plot in Figure 4.20, the optimal aileron and rudder input uncertainty bounds computed across the frequency range for the lateral LFT model is larger than the bounds computed for the identified models. This indicates that the lateral LFT model has a larger uncertainty region at each of the frequency point as compared to the identified models. This means that the lateral LFT model overbounds the flight test identified models and contains the set of models from the flight test identification. The gap between the uncertainty bounds for the lateral LFT model and identified models indicates the conservatism of the lateral LFT model in representing the flight test identified model sets. To reduce this gap, more flight test data should be collected to update the nonlinear simulation model parametric uncertainty bounds to help to tighten the gap between the LFT model and the flight test identified models.

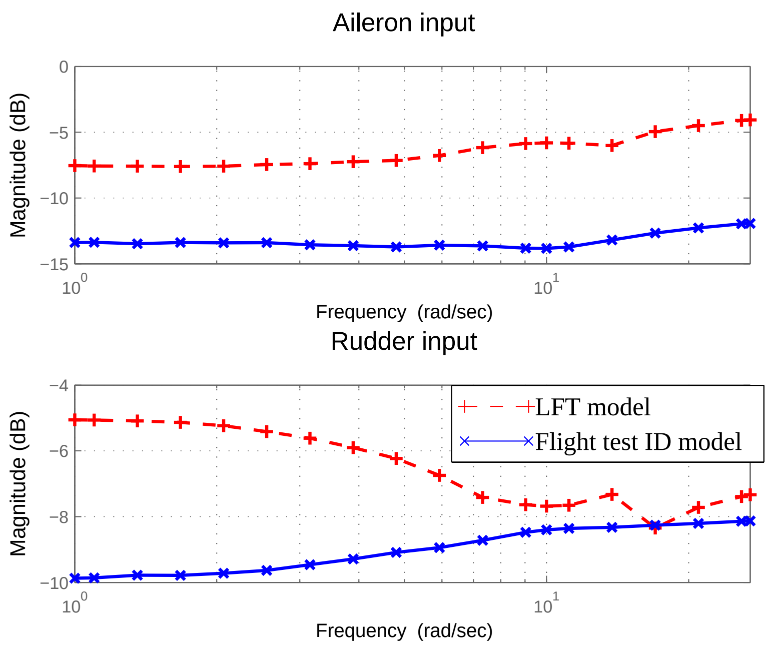

Figure 4.20: Input multiplicative uncertainty bounds for lateral LFT model and flight test identified models

| Full model uncertainty | Physical parameter | Lon model uncertainty | Lat model uncertainty |
|---|---|---|---|
| $\delta_1$ | $C_{D_{\delta_a}}$ | - | $\delta_1^{lat}$ |
| $\delta_2$ | $C_{D_{\delta_e}}$ | $\delta_1^{lon}$ | - |
| $\delta_3$ | $C_{D_{\delta_r}}$ | - | $\delta_2^{lat}$ |
| $\delta_4$ | $C_{D_{min}}$ | $\delta_2^{lon}$ | $\delta_3^{lat}$ |
| $\delta_5$ | $C_{L_0}$ | $\delta_3^{lon}$ | $\delta_4^{lat}$ |
| $\delta_6$ | $C_{L_\alpha}$ | $\delta_4^{lon}$ | - |
| $\delta_7$ | $C_{D_{\dot{\alpha}}}$ | $\delta_5^{lon}$ | - |
| $\delta_8$ | $C_{L_{\delta_e}}$ | $\delta_6^{lon}$ | - |
| $\delta_{9,10}$ | $C_{L_{minD}}$ | $\delta_{7,8}^{lon}$ | $\delta_{5,6}^{lat}$ |
| $\delta_{11}$ | $C_{L_q}$ | $\delta_9^{lon}$ | - |
| $\delta_{12}$ | $C_P$ | - | - |
| $\delta_{13}$ | $C_T$ | $\delta_{10}^{lon}$ | - |
| $\delta_{14}$ | $C_{Y_\beta}$ | $\delta_{11}^{lon}$ | $\delta_7^{lat}$ |
| $\delta_{15}$ | $C_{Y_{\delta_r}}$ | - | $\delta_8^{lat}$ |
| $\delta_{16}$ | $c_{l_\beta}$ | $\delta_{12}^{lon}$ | $\delta_9^{lat}$ |
| $\delta_{17}$ | $c_{l_{\delta_a}}$ | - | $\delta_{10}^{lat}$ |
| $\delta_{18}$ | $c_{l_{\delta_r}}$ | - | $\delta_{11}^{lat}$ |
| $\delta_{19}$ | $c_{l_p}$ | - | $\delta_{12}^{lat}$ |
| $\delta_{20}$ | $c_{l_r}$ | - | $\delta_{13}^{lat}$ |
| $\delta_{21}$ | $c_{m_0}$ | $\delta_{13}^{lon}$ | - |
| $\delta_{22}$ | $c_{m_\alpha}$ | $\delta_{14}^{lon}$ | - |
| $\delta_{23}$ | $c_{m_{\dot{\alpha}}}$ | $\delta_{15}^{lon}$ | - |
| $\delta_{24}$ | $c_{m_{\delta_e}}$ | $\delta_{16}^{lon}$ | - |
| $\delta_{25}$ | $c_{m_q}$ | $\delta_{17}^{lon}$ | - |
| $\delta_{26}$ | $c_{n_\beta}$ | $\delta_{18}^{lon}$ | $\delta_{14}^{lat}$ |
| $\delta_{27}$ | $c_{n_{\delta_a}}$ | - | $\delta_{15}^{lat}$ |
| $\delta_{28}$ | $c_{n_{\delta_r}}$ | - | $\delta_{16}^{lat}$ |
| $\delta_{29}$ | $c_{n_p}$ | - | $\delta_{17}^{lat}$ |
| $\delta_{30}$ | $c_{n_r}$ | - | $\delta_{18}^{lat}$ |
| $\delta_{31}$ | $J_{m_p}$ | - | - |
| $\delta_{32,33,34}$ | $I_{xx}$ | $\delta_{19,20}^{lon}$ | $\delta_{19,20}^{lat}$ |
| $\delta_{35,36,37,38,39,40}$ | $I_{xz}$ | $\delta_{21,22,23,24}^{lon}$ | $\delta_{21,22,23,24}^{lat}$ |
| $\delta_{41,42,43}$ | $I_{yy}$ | $\delta_{25,26,27}^{lon}$ | $\delta_{25,26}^{lat}$ |
| $\delta_{44,45,46}$ | $I_{zz}$ | $\delta_{28,29}^{lon}$ | $\delta_{27,28}^{lat}$ |

Table 4.1: Uncertain parameters in full and decoupled models ("-" denotes parameter that has been eliminated)

Chapter 5

# Flight Controller Synthesis and Implementation

The success of autonomous UAV operations depends on the autopilot system for its control, guidance and navigation tasks. Flight control design without an aircraft mathematical model is a difficult task. Flight control engineers have to perform manual tuning of the controller gains during flight testings when no model is available. This is a dangerous and time-consuming process and is limited to classical single-input, single-output (SISO) controller design method. The classical controller design approach is attractive because it is simple to apply and implement. The controller is usually designed by successive closure of feedback loops from inner angular rate feedback loops to outer tracking loops. However, this becomes increasingly difficult when more loops are added and requires a significant amount of time in trial and error tuning process that may not guarantee to obtain a controller with desired performance.

The availability of plant model permits the use of sophisticated model-based control design methods for which the designed controller can be easily synthesized and verified in simulation before any flight test is conducted. Robust multivariable control design techniques are able to handle model uncertainties and allow multivariable controller design in the presence of signal uncertainties. One particular robust multivariable control design method, $\mu$ synthesis, is popular due to its ability to account for model uncertainty and performance in the same framework. With increasing computation power of current computers and embedded systems, this offers a viable alternative to classical controller design method.

In this chapter, the $H_\infty$ and $\mu$ controller synthesis methods are used to design a linear, multivariable lateral controller using the model and model uncertainty developed in previous chapters. The focus of the controller synthesis process is the application of model-based control design software tools as part of the integrated framework environment to provide a systematic approach for controller synthesis. This helps to bridge the theory-engineering gap of controller design software tools in producing controllers that are suitable for direct implementation on the actual system.

## 5.1 Flight Control Architecture Overview

Autonomous operation of an UAV can be divided into different flight profiles. In any mission scenario, the UAV will be in autonomous cruise flight phase for majority of its flight time. In a typical cruise flight phase, the UAV will be flying at a desired cruise flight condition and performs waypoint navigation with roll angle tracking, airspeed hold, altitude hold and pitch hold mode engaged. The focus of the controller synthesis work in this section is to design a roll angle tracking controller operating in a cruise flight condition with airspeed, altitude and pitch hold modes engaged.

| **Flight Mode** | **Controller used** | **Function** |
|---|---|---|
| Airspeed Hold | Airspeed controller | Tracking of desired airspeed |
| Altitude Hold | Altitude controller | Tracking of desired altitude |
| Pitch Hold | Pitch angle controller | Tracking of reference pitch angle |
| | | and provides pitch rate damping |
| Roll Tracking | Roll angle controller | Tracking of reference roll angle |
| | | and provides roll and yaw rates damping |

Table 5.1: UAV flight modes

The function for each of the flight mode is summarized in Table 5.1. Figure 5.1 shows the flight control system architecture with various controllers used in the cruise flight phase.

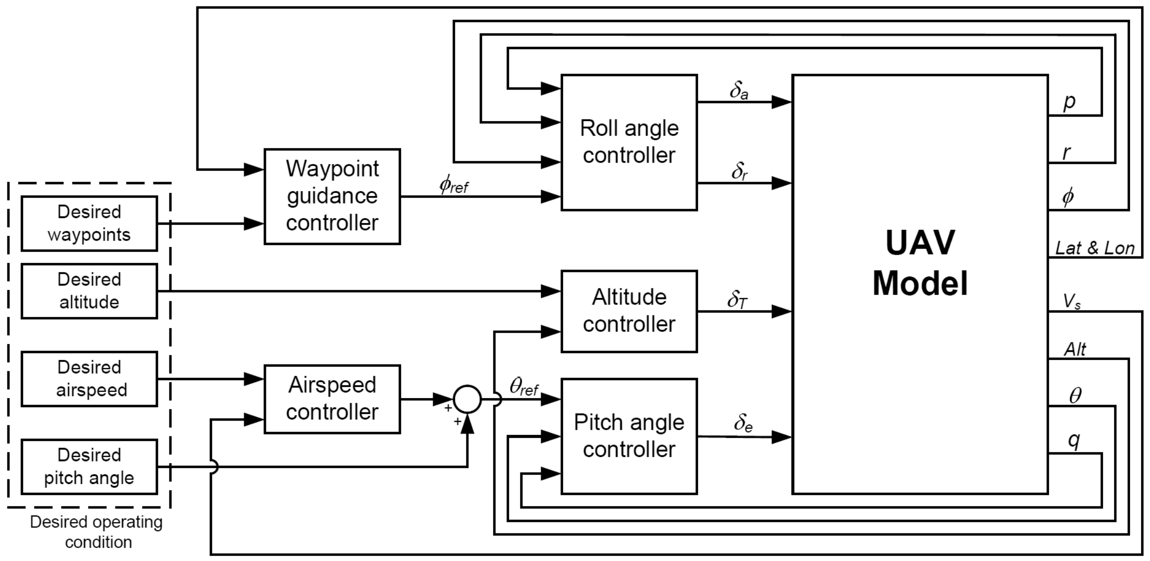

Figure 5.1: UAV flight control architecture for autonomous cruise flight

The airspeed controller works in concurrent with the altitude controller to provide tracking of desired airspeed and altitude. To increase the desired airspeed at a fixed altitude, the airspeed controller will command a negative pitch angle ($\theta_{ref}$) input to the pitch angle controller. The pitch angle controller will command the elevator control input to pitch the aircraft nose down. However, with the aircraft nose pitching down, it will decrease the altitude of the aircraft. In order to maintain at the same altitude, the altitude controller has to increase the throttle control input so that the aircraft can climb back to the desired altitude. Therefore, the increase to the throttle input will increase the airspeed of the aircraft to the new desired airspeed required.

The altitude controller will increase the throttle control input to increase the desired altitude at constant airspeed. However, increasing the throttle control input increases the airspeed above the desired airspeed. Therefore, the airspeed controller will increase the pitch angle demand of the aircraft to slow the aircraft down to the desired airspeed. With an increase in pitch angle, the aircraft will climb to the new desired altitude required.

The advantages of controlling airspeed and altitude with pitch angle and throttle control respectively rather than controlling airspeed by throttle control and altitude control by pitch angle are as follows:

- In the event of engine failure, the aircraft will have a gentle descent in altitude without airspeed and pitch angle controllers destabilizing the aircraft pitch axis. If the altitude is being controlled by pitch angle command, it will pitch the aircraft nose up when the aircraft loses altitude and the airspeed is decreasing due to the loss of engine thrust. This will cause the aircraft to stall, leading to an uncontrollable recovery situation.
- During the cruise flight condition, it is desirable to have a higher control bandwidth for the aircraft airspeed than the altitude. This is because the small UAV is more sensitive to wind gust disturbance. Regulation of airspeed using elevator control surface is faster than using the propulsion system to control the airspeed since there is time delay in the propulsion system dynamics.
- The use of throttle control for altitude control needs a lower control bandwidth than using throttle control for controlling the airspeed. This will result in less variation in throttle control input used. For increase efficiency of the propulsion system and longer flight duration, it is desirable to keep the throttle at a fixed input with minimum variation.

## 5.2 Problem Formulation for Flight Control Synthesis

The flight control synthesis and validation for autonomous cruise flight in this research will only focus on the synthesis of roll angle controller to limit the thesis work scope. However, this will not compromise the ability to demonstrate the key concepts, approaches and methodologies to fulfill the objectives of the research. The control synthesis problem is to synthesize a lateral axis controller with a specific roll angle tracking and yaw rate damping requirements. This problem formulation is chosen with the following considerations:

- In a cruise flight condition, the aircraft dynamics can be linearized and decoupled into longitudinal and lateral-directional modes since the cross-coupling effect between the two modes is negligible (Section 3.1.1). Based on the flight dynamics model, large amplitude variation in the longitudinal motion can occur without perturbing the lateral model states but large lateral motion will affect the longitudinal modes through nonlinear coupling effects. Hence for lateral axis control synthesis problem, flight test result validation will not be significantly affected by the longitudinal motion for the flight operating region. Note that the longitudinal axis is controlled by a PID controller.

- Synthesis of a flight control for lateral axis model poses a more challenging problem than the longitudinal axis controller. The short-period and phugoid mode for the longitudinal model are usually well separated with different time-scales. However, for lateral axis dynamics, the roll and Dutch-roll mode can have almost the same time-scale. This results in significant coupling effects that makes the lateral axis controller synthesis problem more challenging.

The objective of the flight control design is to follow the reference roll angle commands generated by the waypoint guidance controller during the UAV autonomous cruise flight phase. The synthesis of waypoint guidance controller is not within the scope of the research and it is assumed that the waypoint guidance is done primary using roll angle commands.

Initially a classical PID controller for roll and pitch angles tracking is implemented and tuned using flight tests conducted. The pitch angle PID controller is used to provide stabilization for the longitudinal axis during the flight testing of the synthesized robust roll angle controller. Subsequently, the roll angle controller will be designed and implemented using $\mu$ controller synthesis.

## 5.3 Classical Control Design

The standard flight control system is synthesized by successive feedback loops closure to stabilize and control the aircraft. Usually, inner loop angular rate feedback are used to stabilize the aircraft and proportional/integral control is used to improve performance. This design process becomes increasingly difficult when more loops are added to the control system. This is especially true for multivariable systems. Applying classical control design technique with successive closure of individual loop requires a significant amount of time in the trial and error process. Despite the amount of time spent on the design, it may not guarantee a successful controller design or the designed controller may give poor closed-loop performance. This motivates the use of model-based control design methods for flight control system design.

This section provides a brief description for roll and pitch angle controllers designs and implementation using PID controller. Flight tests were conducted to manual tune the PID controllers based on Zigler-Nichols method to obtain suboptimal controllers for the cruise flight condition.

### 5.3.1 Controller Architecture

The flight control architecture is presented in Figure 5.1. The PID roll and pitch angle controllers synthesized to track reference command angles ($\phi_{ref}$, $\theta_{ref}$) and provide damping in the closed-loop system are shown in Figure 5.2. An anti-windup reset is used for each integrator to keep the integrator effort small during saturation to improve the transient flight characteristics of the design. The anti-windup reset works by setting the integrator to zero when the output from the controller has reached its saturation limit.

### 5.3.2 Controller Tuning

The roll and pitch angle PID controllers are tuned during flight testing based on Zigler-Nichols tuning approach. The tuning objective is to synthesize a stable suboptimal controller with minimum emphasis on the controller optimality for good closed-loop performance. The roll angle controller is tuned first since large amplitude variations in the lateral axis can affect the longitudinal mode. Tuning of the pitch angle controller is easier after the lateral axis is stabilized with the roll angle controller. The procedures for tuning and testing the roll angle controller are:

1. Set the reference roll angle command to zero. Tune the controller to achieve a wing-leveled flight. The aircraft is manually piloted to a wing-leveled flight before the roll angle controller is engaged. During the controller tuning, if the wings start to oscillate rapidly (more than 1.5 Hz), the $K_{P_\phi}$ and $K_{D_\phi}$ feedback gains are reduced. If the wings oscillate slowly (less than 1 Hz), the $K_{I_\phi}$ feedback gain is reduced. Over a longer time period of wing-leveled flight, if the aircraft wings do not hold its wing-leveled flight well, the $K_{I_\phi}$ feedback gain is increased. During the tuning process of the roll angle

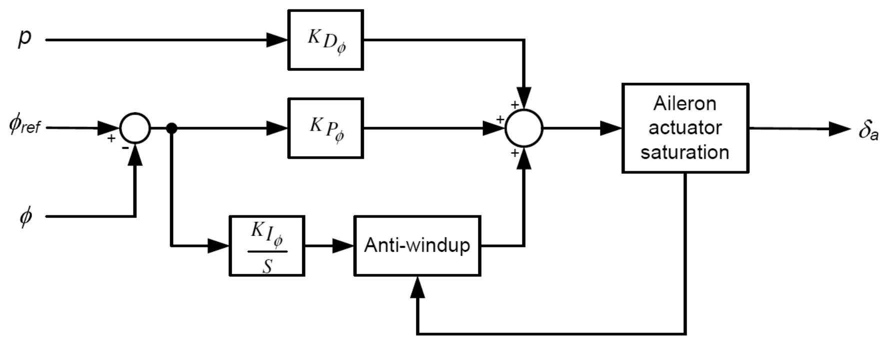

(a) Roll angle PID controller

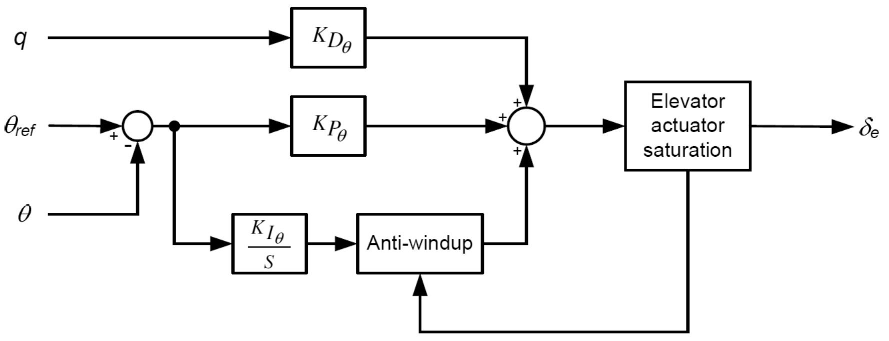

(b) Pitch angle PID controller

Figure 5.2: Roll and pitch angle PID controllers

controller, the RC pilot needs to provide elevator, rudder and throttle control inputs to stabilize and control the aircraft to remain at cruise flight operating condition.

2. The aircraft is manually piloted to different initial roll angle positions from wing-leveled flight before the roll angle controller is engaged. The PID gains are tuned again so that the roll angle controller is able to bring the aircraft back to stable wing-leveled flight position with acceptable transient response of small roll angle overshoot of 2 to 5 degrees and setting time of between 2 to 3 seconds.

3. The reference roll angle command is varied in real-time by the RC pilot using the RC control box and the controller gains are tuned for dynamic reference roll angle tracking. Figure 5.3(a) shows the roll angle tracking performance of the tuned roll angle controller obtained.

Once the roll angle controller has been tuned, the pitch angle controller is tuned with the roll angle controller loop closed and the roll angle reference command set to zero. The tuning procedures for the pitch angle controller is similar to the roll angle controller tuning, which are as follows:

1. Set the pitch angle reference command to zero to tune the controller during straight and wing-leveled flight with zero pitch angle. With the roll angle controller engaged, the aircraft is manually piloted to a straight and wing-leveled flight before the pitch angle controller is turned on. During the controller tuning, if the aircraft starts to have rapid pitch oscillations (more than 1.5 Hz), the $K_{P_\theta}$ and $K_{D_\theta}$ feedback gains are reduced. If the pitch oscillations are slow (less than 1 Hz), the $K_{I_\theta}$ feedback gain is reduced. Over a longer time period of straight and wing-leveled flight, if the aircraft starts to pitch up or down, the $K_{I_\theta}$ feedback gain is increased. During the tuning process with the roll and pitch angle controllers engaged, the RC pilot needs to provide throttle control input to regulate the aircraft airspeed.

2. The aircraft is manually piloted to different initial nose up or nose down pitch angles flight conditions before the pitch angle controller is engaged. The PID gains for the pitch angle controller are tuned during this process so that the pitch angle controller is able to control the aircraft back to stable leveled flight position with setting time of between 2 to 3 seconds.

3. The reference pitch angle command is varied in real-time by the RC pilot and the pitch angle controller gains are tuned for dynamic pitch reference command tracking. Figure 5.3(b) shows the pitch angle tracking performance result of the tuned pitch angle controller.

## 5.4 Model-based Controller Synthesis

The roll angle controller is redesigned in this section using a model-based controller synthesis technique. Model-based controller synthesis approaches take advantage of the models of the aircraft in the integrated framework for synthesis and validation of the designed controller. This provides a standard procedure for controller synthesis and validation during

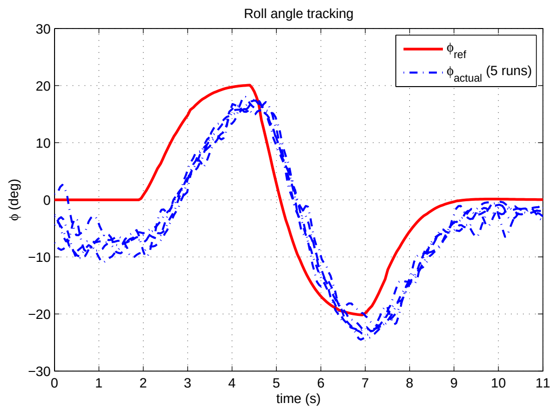

(a) Roll angle controller tracking

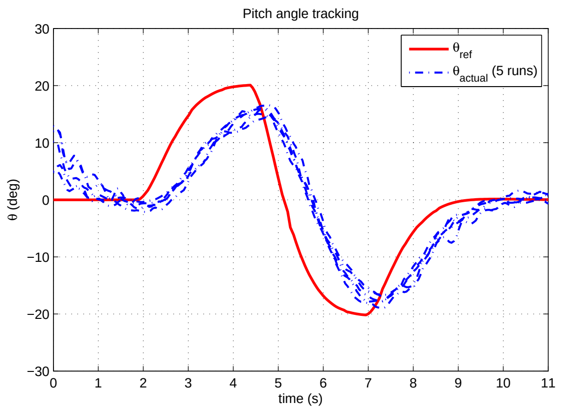

(b) Pitch angle controller tracking

Figure 5.3: Tracking performance of roll and pitch angle PID controllers

the flight control development. Two model-based methods for controller synthesis, $H_\infty$ and $\mu$ synthesis methods, from the robust control are used. The $H_\infty$ and $\mu$ synthesis techniques are mixed-sensitivity controller design technique that allows conflicting design objectives to optimally satisfy various design objectives through usage of different weighting functions in the controller synthesis formulation. Hence, the selection of appropriate weighting functions is very important for successful $H_\infty$ and $\mu$ controller designs.

### 5.4.1 Control Design Specifications

The selection of weighting functions for $H_\infty$ and $\mu$ controllers synthesis is based on the desired control design specifications. The performance objectives of the roll angle controller is to provide accurate tracking of reference roll angle commands generated by the waypoint guidance controller and roll and yaw rate dampings in the lateral axis. These objectives are challenging because tracking of roll angle commands will cause a yaw in the opposite direction (adverse yaw) due to the aerodynamic coupling between the roll and yaw axes of the aircraft, which opposes the performance objective of providing yaw rate damping during the roll angle commands tracking. The performance criteria for the roll angle control design are as follows:

- Track roll angle reference commands ($\phi_{ref}$) with less than 6 degrees tracking error for up to 1 rad/s bandwidth. The rise time for the roll angle tracking should be less than 2.5 seconds.

- The yaw rate coupling should be less than 25 deg/s across all frequencies.
- The control effort should stay within the control surfaces saturation limits at all times.
- The controller should be robust and achieve desired performance objectives for all values of the model uncertainties described in the aircraft uncertainty modeling in Chapter 4.2.

### 5.4.2 Problem Formulation and Weighting Functions Selection

The roll angle control design problem is formulated as a standard signal-based $H_\infty$ controller design problem where different design specifications are achieved simultaneously. This reduces the control design problem to optimization problem where the norm size of the error signals is to be kept small subjected to different external signals that affect the UAV system.

Weighting functions are used to shape the frequency content information for the input exogenous signals and output error signals to achieve the desired design specifications. It helps to normalize and weight each of the requirements so that the controller synthesis problem is well-posed. Weighting functions are also used to incorporate model uncertainty into the controller design process. Figure 5.4 shows the control design interconnection with the weighting functions and reference model used for the signal-based $H_\infty$ roll angle controller synthesis. The selection of the weighting functions and reference model in the system interconnection are described in the following sections.

#### 5.4.2.1 UAV lateral model

The UAV lateral model used is a three states state-space model obtained from flight test system identification as described in Section 3.1.2.

$$\begin{bmatrix} \dot{p} \\ \dot{r} \\ \dot{\phi} \end{bmatrix} = \begin{bmatrix} L_p & L_r & 0 \\ N_p & N_r & 0 \\ 1 & 0 & 0 \end{bmatrix} \begin{bmatrix} p \\ r \\ \phi \end{bmatrix} + \begin{bmatrix} L_{\delta_a} & L_{\delta_r} \\ N_{\delta_a} & N_{\delta_r} \\ 0 & 0 \end{bmatrix} \begin{bmatrix} \delta_a \\ \delta_r \end{bmatrix} \tag{5.1}$$

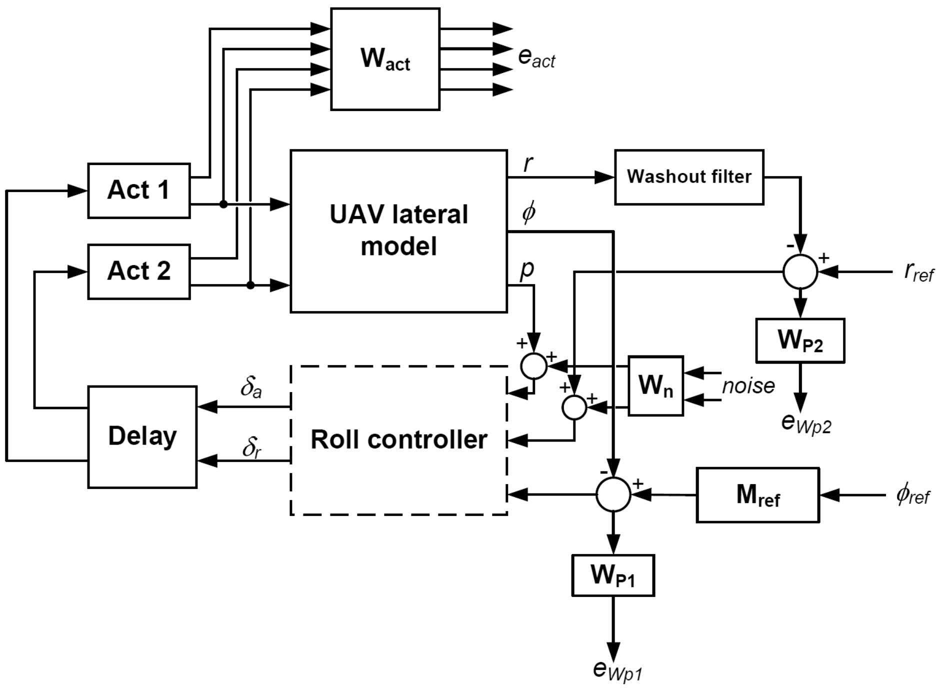

Figure 5.4: System interconnection for $H_\infty$ controller synthesis

The control and stability parameters used in Equation 5.1 are given in Appendix Table B.2. For $H_\infty$ controller synthesis, only the nominal value of the parameters are used. However in the $\mu$ synthesis design technique, the parameter uncertainty values between lower and upper bounds are used to describe uncertainty variations in the model.

### 5.4.2.2 Actuator model

The actuator models, ACT 1 (rudder servo actuator) and ACT 2 (aileron servo actuator), describe the dynamics for the servo actuators used in the Ultrastick aircraft. The outputs from the actuator model are the angular rate and angle deflections. The aileron and rudder servo actuators are the same and are modeled by first order dynamics which mainly accounts for actuator time lag. The actuator time lag is approximated to be 20 ms (from Section 2.2.4). Hence, the angular rate and angle deflection outputs from the actuators are described by the transfer functions:

$$\dot{\delta}_{a,r} = \frac{50s}{s+50}\ , \quad \delta_{a,r} = \frac{50}{s+50}$$

#### 5.4.2.3 Actuator Output Weighting Function

The actuator output weighting function $W_{act}$ is used to limit the maximum angular rate and angle deflections for both the aileron and rudder control surfaces in the $H_\infty$ problem formulation. A diagonal constant weight, corresponding to aileron angular rate and angle deflections and rudder angular rate and angle deflections, is used. A constant weight of 1.0 is used for the aileron and rudder angle deflection and this limits the outputs from the aileron and rudder deflection angle to be within ± 25 degrees while the deflection rates are limited to be within ± 5 rad/s using a constant weighting function of 0.2. Hence the actuator weighting function $W_{act}$ is given by:

$$W_{act} = \begin{bmatrix} 0.2 & 0 & 0 & 0 \\ 0 & 1.0 & 0 & 0 \\ 0 & 0 & 0.2 & 0 \\ 0 & 0 & 0 & 1.0 \end{bmatrix}$$

#### 5.4.2.4 Time Delay

The flight avionics system is made up of different hardware components integrated together. With different hardware devices and signals flow between them occurring at the same time, there will be time delay within the flight control system since it takes finite amount of time to process, pack, send or receive data from one device to the other. A time delay model is used to account for the time delay ($T_d$) in the closed-loop system measured in the PIL simulator. This is described in more detail in the next chapter. It is important to include the time delay in the controller synthesis process as time delay in the closed-loop system reduces the closed-loop stability margin and bandwidth. A first order Padé approximation is used to approximate the time delay:

$$e^{-T_d s} \simeq \frac{1 - T_d s/2}{1 + T_d s/2}$$

where the time delay $T_d$ measured from the PIL simulator is about 0.08 seconds.

#### 5.4.2.5 Washout Filter

The roll angle controller commands the rudder to provide yaw damping at high frequency during the roll angle tracking maneuver. A washout filter is added to the yaw rate sensor feedback path to aid the controller. A washout filter is simply a high pass filter that only allows high frequencies signal to go through while attenuating low frequencies signal. The transfer function of the washout filter is given by:

$$\frac{s}{s+\omega_w}$$

where $\omega_w$ $(rad/s)$ is the cutoff frequency that the yaw rate signal will be attenuated such that the roll angle controller will not provide any yaw rate feedback during steady turn. The cutoff frequency is selected as 15 rad/s.

#### 5.4.2.6 Sensor Noise

A constant weight is used in the controller synthesis process to model the gyros noise for roll and yaw angular rate sensor measurements fed back to the controller. The weight is selected based on three standard deviation bound (99.7 % confidence interval) of the gyros noise. The sensor roll and yaw gyros noise standard deviation, published in [54], is $8.73 \times 10^{-2}$ $rad/s$. Therefore the three standard deviation noise bound is 0.03 $rad/s$. Hence the sensor weight used is:

$$W_n = \begin{bmatrix} 0.03 & 0 \\ 0 & 0.03 \end{bmatrix}$$

#### 5.4.2.7 Model Reference

A reference model is used to define the ideal response of the closed-loop roll angle tracking response. The ideal response is prescribed by the specifications required by the waypoint guidance controller which provides the reference roll angle commands. A second order reference model is used to provide a smooth reference roll angle command for the roll angle tracking controller. A rise time of 2.2 seconds is chosen to provide a reasonable bandwidth in the reference roll angle command. A damping ratio of 0.75 is selected to have an overshoot of less than 3 % in the reference roll angle command from the reference roll angle command generated by the waypoint guidance controller. The second order model reference is given by:

$$M_{ref} = \frac{0.669}{s^2 + 1.227s + 0.669}$$

#### 5.4.2.8 Performance Weighting Functions

Performance weighting functions, $Wp_1$ and $Wp_2$, are used to shape the roll angle and yaw angular rate tracking error responses to achieve the desired closed-loop performance specifications. $Wp_1$ is used to keep the mismatch between the reference roll angle command and the actual aircraft roll angle small at low frequencies with small steady-state error. The controller should roll-off at high frequencies since tracking of reference roll angle command is not required at high frequencies due to the low frequency reference command signals from the waypoint navigation controller. Large model uncertainty at high frequencies is another reason why the performance should decrease below 1 around the loop-bandwidth. Since the rise time of the roll angle reference command is set to 2.2 seconds using the reference model, good tracking of the roll angle reference command signals is required from 0 to 1 $rad/s$. The accuracy of the AHRS roll angle attitude solution obtained is approximately $\pm$ 5 degrees. Hence a steady-state reference roll angle tracking error of less than 6 degrees is desired. The weighting function used is:

$$Wp_1 = \frac{2.5(s + 40)}{s + 10}$$

This has a low frequency gain of 10 for up to 1 rad/s which gives a roll angle tracking error of less than 5.7 degrees.

$Wp_2$ is used to penalize the amplitude of the yaw angular rate with the yaw rate reference, $r_{ref}$, set to zero. The weighting function used is:

$$Wp_2 = \frac{1}{0.15}$$

The $Wp_2$ weight is used to limit the yaw angular rate to be less than $\pm$ 25 deg/s across all frequencies range.

### 5.4.3 $H_\infty$ and $\mu$ Controller Synthesis

This section describes $H_\infty$ and $\mu$ synthesis techniques with the system interconnection defined in Figure 5.4 to compute $H_\infty$ and $\mu$ synthesis controllers.

#### 5.4.3.1 $H_\infty$ Controller Synthesis

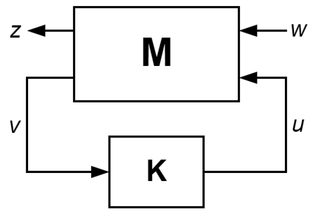

Figure 5.5: Configuration for $H_\infty$ controller synthesis

The system interconnection defined in Figure 5.4 can be put into a general feedback design problem configuration shown in Figure 5.5. $M$ represents the system interconnection structure in Figure 5.4, $K$ is the feedback controller, $u$ is a vector of control inputs from the controller, $v$ is a vector of measurement signals, $w$ is a vector of exogenous input signals and $z$ is a vector of errors to be kept small to meet the control design objectives.

The closed-loop transfer function from $w$ to $z$ is given by the linear fractional transformation:

$$z = F_l(M, K)w$$

The $H_\infty$ controller synthesis for the general configuration in Figure 5.5 is to find all stabilizing controllers K which minimize

$$\| F_l(M, K) \|_\infty = \max_\omega \hat{\sigma}(F_l(M, K)(j\omega))$$

This problem has been solved efficiently by using algorithms in [55] for a sub-optimal $H_\infty$ controller with:

$$\| F_l(M, K) \|_\infty < \gamma$$

by reducing the value of the $\gamma$ iteratively. The optimality of the designed controller is dependent on the minimum $\gamma$ obtained in the synthesis. Therefore the suboptimal $H_\infty$

controller synthesis problem is to find all stabilizing controllers K with $\gamma$ less than $\gamma_{\min}$ where $\gamma_{\min}$ is the minimum value of $\| F_l(P, K) \|_\infty$ over all stabilizing controllers K [37].

The Matlab function ***hinfsyn*** is used to compute a sub-optimal $H_\infty$ controller for the $H_\infty$ synthesis problem describes above using $\gamma$-iteration [39]. The $H_\infty$ synthesis procedure uses only the nominal plant model in Figure 5.4 without model uncertainty. The controller design objective is to find a sub-optimal controller that balances the tradeoff in achieving required closed-loop performance and small state order controller that is feasible to implement in the flight computer system.

#### 5.4.3.2 $\mu$ Synthesis

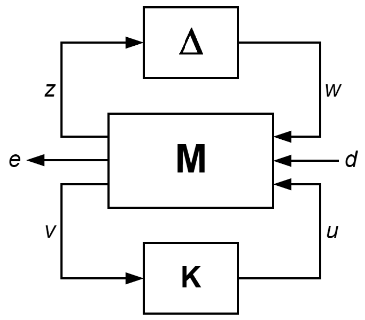

Figure 5.6: Configuration for $\mu$ controller synthesis

The $\mu$ synthesis process differs from the $H_\infty$ controller synthesis process as it is able to synthesize robust controllers with model uncertainty included into the synthesis process. Figure 5.6 shows the general framework for $\mu$ synthesis. The system interconnection in Figure 5.4 can be rearranged to match the inputs, outputs, uncertainty perturbations and controller in this framework. $M$ represents the system interconnection structure in Figure 5.4, $K$ is the feedback controller, $u$ is a vector of control inputs from the controller, $v$ is a vector of measurement signals, $z$ and $w$ are inputs and outputs to and from the uncertainty block, $d$ is a vector of exogenous input signals and $e$ is a vector of errors to be kept small to meet the control design objectives.

The $\mu$ synthesis makes use of the results from the structure singular value $\mu$ to find the controller that minimizes a given $\mu$ condition. The details of the structure singular value can be found in [56]. The $\mu$ synthesis problem is to find a controller $K$ that minimizes [57]

$$\inf_{K} \sup_{\omega} \mu(F_l(M(j\omega), K(j\omega))) \tag{5.2}$$

However, calculation of the $\mu$ value is NP-hard and the minimization problem is reformulated as a minimization of the upper bounds of the structured singular value that includes a real, rational, stable, minimum phase transfer function $D(j\omega)$ [58]. The synthesis problem is rewritten to find a stabilizing controller $K$ and a scaling matrix $D$ that minimizes:

$$\| D(j\omega)F_l(M(j\omega), K(j\omega))D^{-1}(j\omega) \|_\infty \tag{5.3}$$

The minimization problem in Equation 5.3 can be solved using alternative minimization with $K$ and $D$ parameter that combines $H_\infty$ and $\mu$ synthesis. This iteration approach is called "D-K iteration". The details of the D-K iteration can be found in [56].

The Matlab function ***dksyn*** in the Robust Control Toolbox is used for the $\mu$ synthesis problem for the system interconnection in Figure 5.4. The ***dksyn*** command generates a robust controller through minimizing the $\mu$ value using D-K iterations and solving a sequence of scaled $H_\infty$ controller problems to achieve the robust performance of the closed-loop system associated with uncertain plant model [39]. A sub-optimal $\mu$ controller, rather than an optimal $\mu$ controller, is desired . This is because the order of the controller grows rapidly with D-K optimization and results to a high order controller that makes the controller implementation in the flight computer system difficult.

## 5.5 Controller Implementation

The controllers obtained from $H_\infty$ and $\mu$ controller synthesis procedures are continuous time state-space controllers that are useful for testing and analysis within the Matlab/Simulink environment. To successfully implement these controllers on the embedded flight computer system, some important implementation issues have to be addressed. These involve simplifying the high order controller to a low order controller, converting the continuous controller to discrete-time form that is suitable for digital implementation, coding the discrete-time controller for real-time implementation and addressing controller saturation problems. Figure 5.7 shows the flow chart for the controller implementation process.

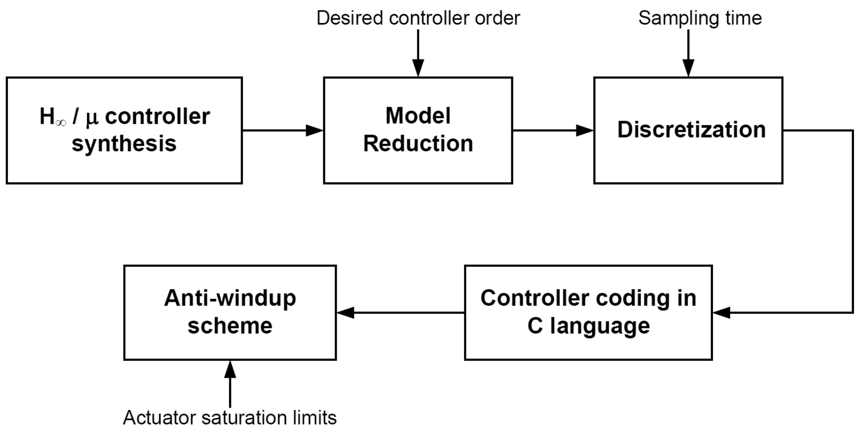
Desired controller order
Sampling time
H∞ / μ controller synthesis
Model Reduction
Discretization
Anti-windup scheme
Controller coding in C language
Actuator saturation limits

Figure 5.7: Controller implementation process

### 5.5.1 Controller Order Reduction

The $H_\infty$ and $\mu$ controller synthesis tools tend to produce relative high order state-space controller. The order of the controller obtained will be at least equal to the order of the plant used for the synthesis. With the inclusion of weighting functions, this further increases the controller order. A complex and high order controller hinders its implementation on a low computation power flight computer system. It is necessary to perform controller order reduction to have a simple and low order controller to reduce the computation requirement on the embedded flight computer.

The objective of controller order reduction is to generate a lower order controller such that the reduced order controller preserves the behavior of the original design with little degradation of the closed-loop system stability and performance in the frequency range of interest.

To achieve these objectives, the controller model reduction process must not significantly change the input-output response of the controller. This is done by removing states that are both less controllable and observable. The Hankel singular values of the system provide a measure of both controllability and observability for each of the state at the same time. A large Hankel singular value means that the state is both highly controllable and observable. Therefore, the states with small Hankel singular values can be removed from the controller state. The Hankel singular values of the controller can be computed using a balance realization of the controller state-space model in which the controllability and observability Gramians are equal [37]. The ***balreal*** command from Matlab's Control System Toolbox is used for the balance realization computation.

Two main approaches to model reduction used are truncation and residualization. In truncation, the states that are to be removed are simply discard. In residualization, the states that are to be removed will have their derivatives set to zero. Subsequently, these states are solved in terms of states that are to be retained with the control input state. The residualization process helps to preserve steady-state gain of the controller. Hence, controller model reduction via truncation often provides a closer match at higher frequency range while residualization will match better at lower frequency range and steady-state [48].

For the roll angle controller, the frequency range of interest is tracking performance in the low frequency range. Therefore the residualization method is used for controller order reduction. The residualization can be done using ***modred*** command from Matlab's Control System Toolbox with the state elimination method chosen to match DC gain.

The procedure for controller order reduction is to perform a balance realization of the controller state-space model and determine which are the states that can be reduced based on the Hankel singular values. Next, residualization is carried out to reduce the controller model order by removing the states with small Hankel singular values. This process is commonly known as balanced residualization.

### 5.5.2 Controller Discretization

In implementation of the controller using digital flight computer system, the continuous-time controller obtained from the reduced order controller requires discretization for digital implementation. The discrete-time controller behaves differently from the continuous-time controller as it samples measurement inputs and updates control outputs at equal sample time step. The control output signals are held constant until the next update. With smaller sampling step, the discrete-time controller approximates the continuous-time controller more closely. However, as the sampling time get smaller, more computation power is required to perform more frequent controller updates. On the other hand, too large sampling time degrades the performance of the controller because the discrete-time controller deviates from the continuous-time controller. This can cause the closed-loop system response to be oscillatory and unstable. Therefore the sampling time for discretization is very important for good performance behavior of the implemented digital controller on the flight computer system.

The update rate for the digital controller implementation is chosen to be 25 Hz and this gives a sampling time of 0.04 seconds. The sampling rate is chosen such that it is faster than the roll mode of the aircraft (time constant of approximately 0.08 seconds from Section 3.5.1.1) but still keep the flight computer within a reasonable computational load. Therefore the continuous-time controller is discretized with sampling time of 0.04 seconds using Matlab ***c2d*** command with a first-order hold method. The first-order hold discretization method is preferred because it provides a linear interpolation between the input sampled data and does not introduce additional time delay to the discretized system unlike zero-order hold method which has a half-sample time delay [59].

### 5.5.3 Controller C Code Implementation

The synthesis and discretization of the controller in Matlab environment are performed using double precision floating-point math. The implementation of digital controller in the flight computer system is done easily with floating point unit since the MPC 555 flight computer uses a 32-bits floating point processor. This is one of the main advantages of using the MPC 555 flight computer over other fixed-point processors as it minimizes the quantization effects and allows for easy and fast floating point math computation.

The implementation of the state-space controller with C code programming is simple and straight forward. With the continuous-time reduced model controller obtained from Section 5.5.1 of the form given by:

$$\begin{aligned} \dot{x}_c &= A_c x_c + B_c u_c \\ y_c &= C_c x_c + D_c u_c \end{aligned} \tag{5.4}$$

where $x_c$ contains the states of the reduced order controller and

$$u_c = \begin{bmatrix} p \\ r_{ref} - r \\ \phi_{ref} - \phi \end{bmatrix}, \quad y_c = \begin{bmatrix} \delta_a \\ \delta_r \end{bmatrix}$$

Applying a first-order hold discretization to Equation 5.4, the discrete-time state-space representation of the controller is given by:

$$\begin{aligned} \dot{x}_c(k+1) &= A_c^k x_c(k) + B_c^k u_c(k) \\ y_c(k) &= C_c^k x_c(k) + D_c^k u_c(k) \end{aligned} \tag{5.5}$$

where $x_c(k)$ contains the states of the controller at k time step, $A_c^k$, $B_c^k$, $C_c^k$, $D_c^k$ are the discrete-time state-space matrices obtained from the ***c2d*** command, and

$$u_c(k) = \begin{bmatrix} p(k) \\ r_{ref}(k) - r(k) \\ \phi_{ref}(k) - \phi(k) \end{bmatrix}, \quad y_c = \begin{bmatrix} \delta_a(k) \\ \delta_r(k) \end{bmatrix}$$

The discrete-time state-space controller in Equation 5.5 is implemented on the flight computer system using C programming language. The C code is implemented through simple matrix multiplication and addition of the state dynamics and output equations in each of the time step with sensor feedback inputs obtained from the sensor data packet.

### 5.5.4 Anti-windup Scheme

The actuator control surfaces used on the UAV have displacement limits given in Appendix Table A.4. Control surfaces saturation occur when the control signal outputs exceed these saturation limits. Once this happens, the flight control system command does not actuate the control surfaces anymore and this effectively becomes an open feedback path. If the control signal continues to applied to the state integrator in Equation 5.5, the integrator action will keep winding up until an opposite sign error signal starts to unwind the integrator [60]. This results in poor performance and poses stability problem for the closed-loop system.

A simple anti-windup scheme is used for the aileron and rudder control surfaces to prevent severe stability and performance degradation problems in event when control surfaces saturation happen. Figure 5.8 shows the implementation of anti-windup scheme. $K_{\delta_a}$ and $K_{\delta_r}$ are the anti-windup gains used for feeding back windup from the roll angle controller when control outputs $\delta_a$ and $\delta_r$ exceed the actuator limits. These gains are chosen to be large enough such that the feedback loops keep the windup small when the actuators are saturated. The gains selected are $K_{\delta_a} = 0.01$ and $K_{\delta_r} = 0.01$.

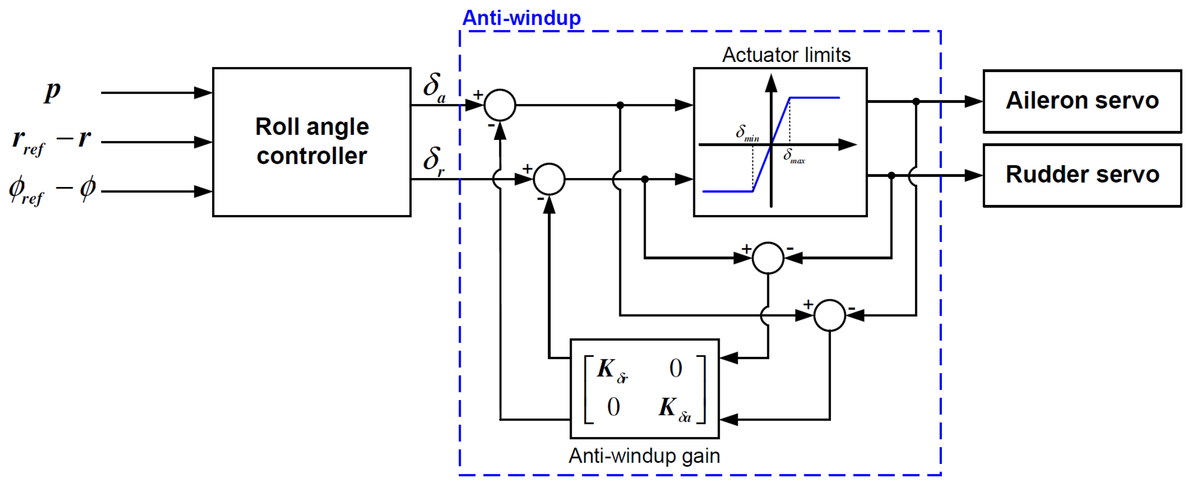

Figure 5.8: Anti-windup implementation

## 5.6 $\mu$ Controller Synthesis and Implementation

In this section, details for the $\mu$ roll angle controller synthesis and implementation on the flight computer are presented. The controller synthesis uses the uncertainty modeling results in Chapter 4.2. The $\mu$ controller is tested and validated in the next chapter using the integrated framework environment. Input multiplicative uncertainty model obtained from overbounding the uncertain lateral model is used for the $\mu$ synthesis. Since $H_\infty$ controller synthesis follows the same controller synthesis procedures except that the model used contains no model uncertainty, it will not be presented here.

### 5.6.1 Input Multiplicative Uncertainty Model

The lateral UAV model with input multiplicative uncertainty (Figure 5.9) used for $\mu$ controller synthesis is obtained using unmodeled LTI dynamic uncertainty model overbounding approach described in Section 4.4.2. The family of N sampled models in Equation 4.6 representing the lateral parametric uncertainty model in Equation 4.5 is obtained by 50 random samplings of the original parametric model. Figure 5.10 shows the plot of the 50 random sampled models. A second order weighting function is synthesized to overbound these 50 sampled models with an input multiplicative uncertainty model. Figure 5.11 shows the Bode magnitude plot of the second order weighting function obtained from the ***ucover*** command overbounding. The weighting functions obtained are:

$$W_{ail} = \frac{0.312s^2 + 10.7s + 33.3}{s^2 + 28.7s + 77.5}, \quad W_{rud} = \frac{0.295s^2 + 5.08s + 40.1}{s^2 + 14.4s + 42.1} \tag{5.6}$$

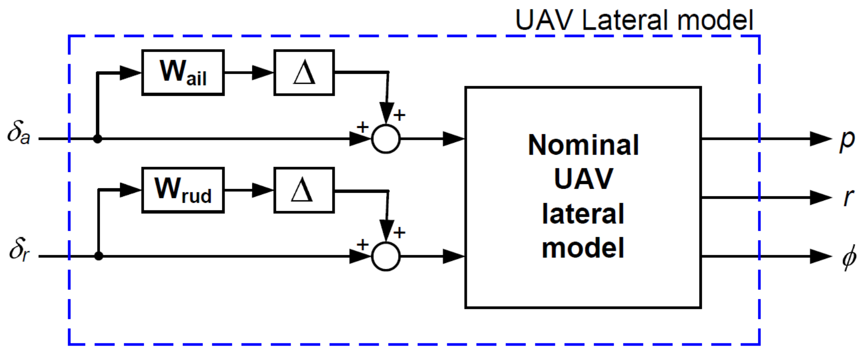

Figure 5.9: Lateral UAV model with input multiplicative uncertainty

### 5.6.2 $\mu$ Controller Synthesis

The $\mu$ controller is synthesized using the system interconnection defined in Figure 5.4 with input multiplicative uncertainty models obtained in Equation 5.6. The D-K controller synthesis gives a controller of 31 states with $\gamma$ value of 0.857 and peak $\mu$ value of 0.817.

The 31 states $\mu$ controller obtained from $\mu$ synthesis has too high state order for implementation on the flight computer system and has to be reduced to a lower order controller. Figure 5.12 shows the plot of the Hankel singular values for the 31 states $\mu$ controller. The

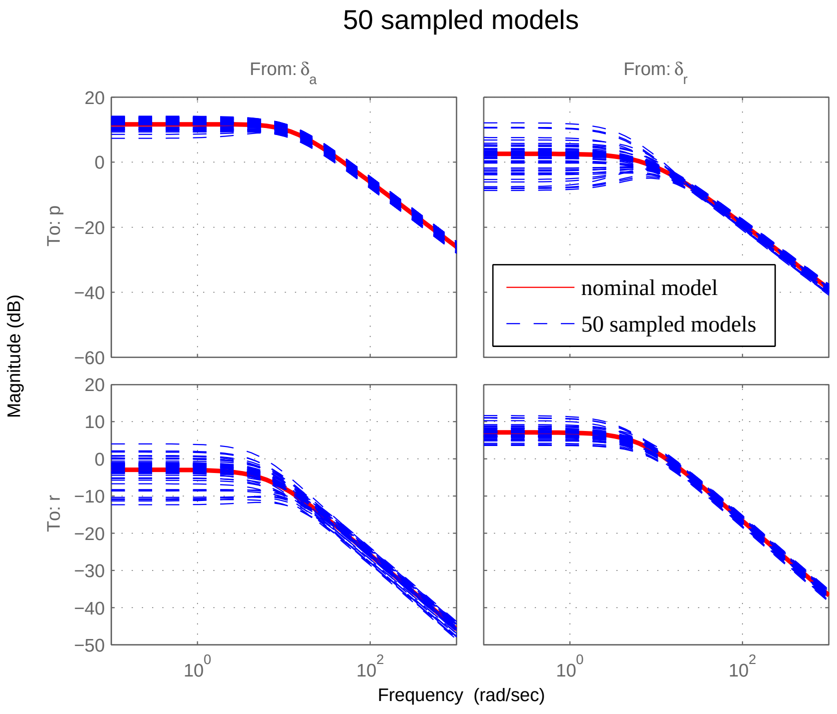

Figure 5.10: 50 random sampled lateral models

plot shows that all the 31 poles are stable and a large number of states have very little contribution to the input/output behavior of the controller. Therefore the states with state energy less than 0.01 are eliminated.

After the states elimination, the reduced order controller has only 8 states. Figure 5.13 shows the Bode magnitude diagram of the original 31 states and the reduced 8 states controller. In the low frequency region below 2 rad/s, the Bode magnitude plot matches very well for the original and reduced order controller. For frequency range up to 10 rad/s, the original and reduced order controller are almost the same, except for the yaw rate input to rudder output channel.

### 5.6.3 Robust Analysis

Robust analysis is performed with the system interconnection shown in Figure 5.4 with the original and reduced order $\mu$ controller. The UAV lateral model used in this analysis is the real parametric uncertainty model given in Equation 4.5. Figure 5.14 shows the

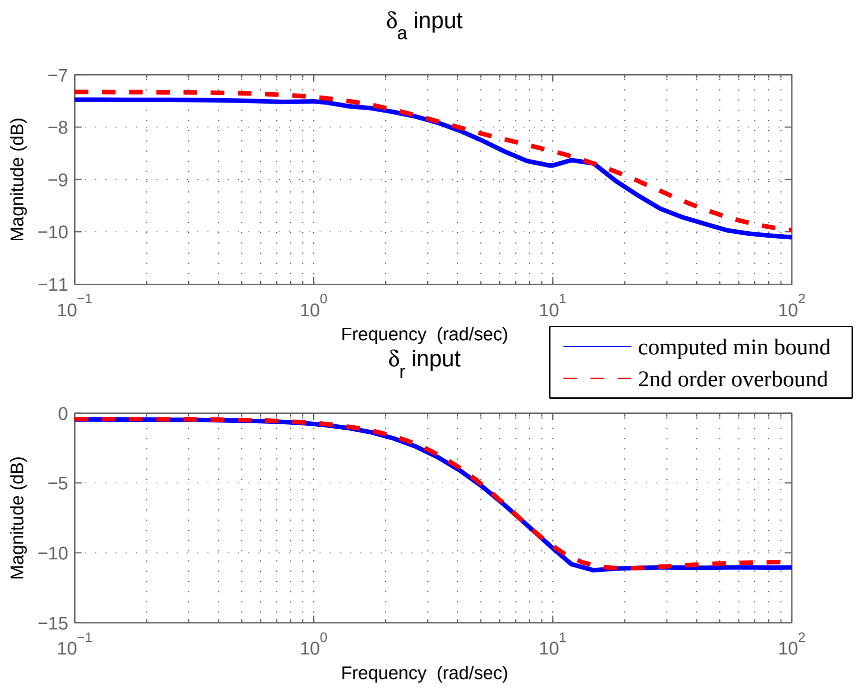

Figure 5.11: Input multiplicative uncertainty model overbound weights

plots for robust stability and performance analysis. Robust stability analysis result of the full and reduced order controller in Figure 5.14 shows no significant difference between the original 31 states controller and the reduced 8 states controller. Hence, reduction in the controller state orders using the residualization model reduction technique for a low order controller does not affect the closed-loop system stability with model uncertainty perturbations. The $\mu$ values for both the original and reduced order controller are less than 0.6 in the frequency range of interest. This indicates that robust stability is achieved and the controllers stabilizes the complete set of uncertain model.

Robust performance analysis for the full and reduced order controller shown in Figure 5.14 indicates that the reduction of controller orders does not affect the closed-loop system performance robustness with model uncertainty perturbations. Within the frequency range of interest, the peak $\mu$ values for the full and reduced order controller are less than 1, indicating that the controllers achieved their desired performance with complete set of model uncertainty perturbations. In summary, the robust analysis results show that the

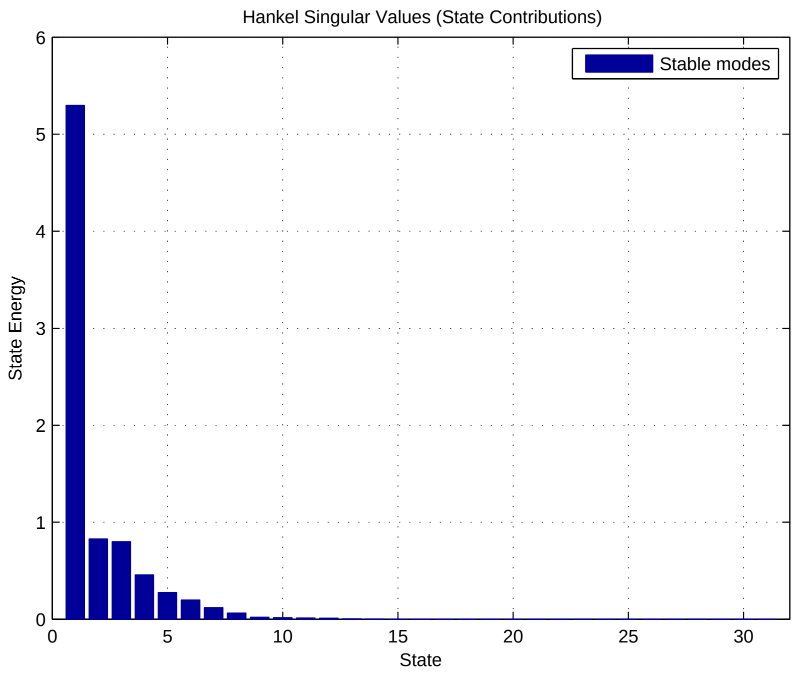

Figure 5.12: Hankel singular value plot of the 31 states $\mu$ controller

reduced order controller has similar closed-loop robustness performance as that of the full order controller with model uncertainty perturbations. Hence the reduced order controller preserves the same behaviors as that of the original full order controller and the reduced order controller is used in the controller implementation.

### 5.6.4 Controller Implementation

For discrete-time digital controller implementation, the reduced order continuous-time $\mu$ controller is being discretized with a sampling time of 0.04 seconds using the first order hold method. This gives a discrete-time state-space controller with 9 by 9 $A_c^k$ matrix, 9 by 3 $B_c^k$ matrix, 2 by 9 $C_c^k$ matrix and 2 by 3 $D_c^k$ matrix in Equation 5.5 for C code programming implementation. The implemented C controller will be tested in the integrated framework developed in the next chapter.

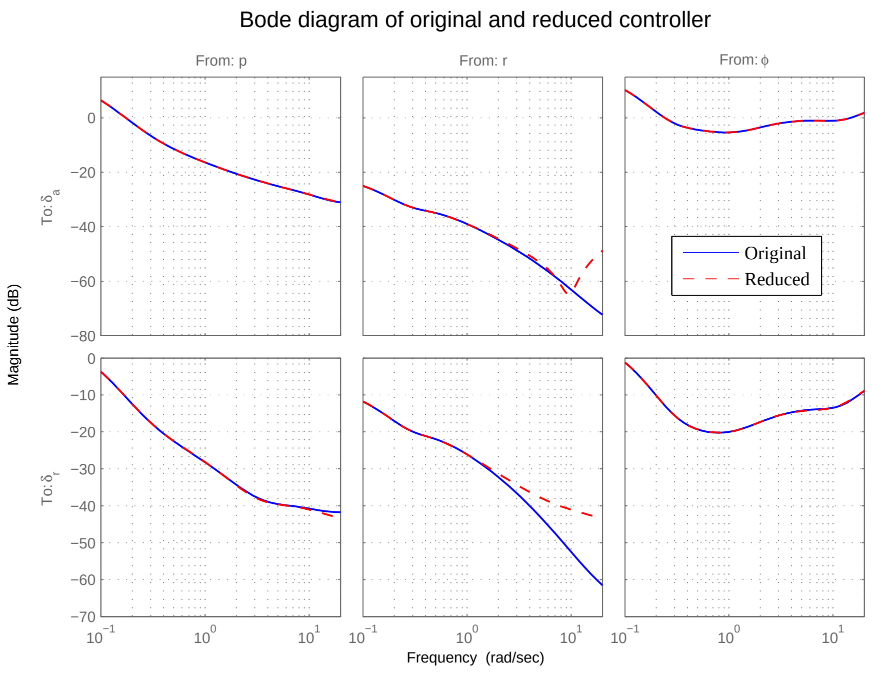

Figure 5.13: Bode diagram of original and reduced order controller

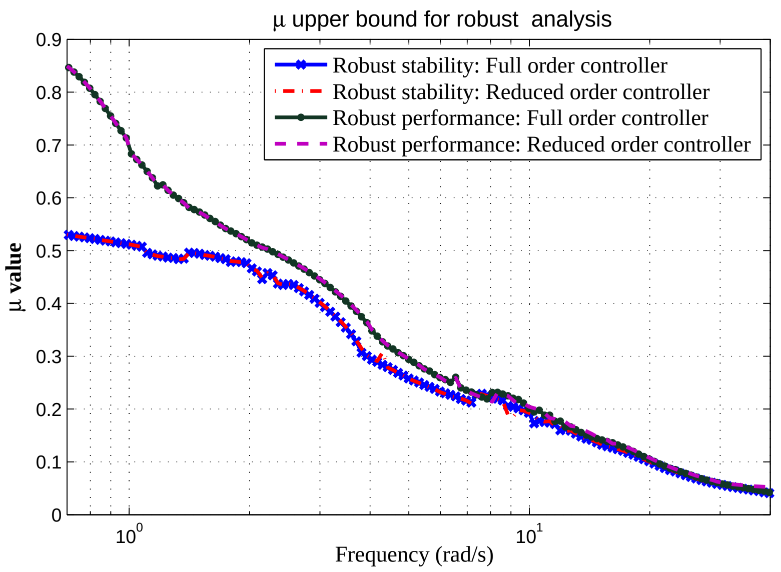

Figure 5.14: Robust stability and performance analysis

Chapter 6

# Flight Control System Testing and Performance Validation in Integrated Framework

The proof of success in any flight control system design is achieving design specifications with the controller implemented in flight test. Flight test validation represents the actual assessment of whether the flight control system design meets the design requirements in the true environment and verifies if the design requirements used are practical and achieve the desired system objectives.

However, flight trials are resource intensive and expensive. With modern flight control system getting more complex, there is a need to use other validation approaches to support and augment the flight control validation process. The ability to update and improve the accuracy of the aerodynamics and system model in a high fidelity simulation model provides an attractive approach to augment the current flight control validation process. The use of simulation-based testing is critical to reducing the cost and time spent in the development of UAV systems.

Simulation-based testing helps to save time and effort prior to actual flight trials as it helps to validate the proper operation of flight control law, software and hardware implementation within the bench test environment. This helps to ensure that the flight control system has high integrity and is bug free prior to flight tests. However, the success of simulation-based validation depends on the accuracy of simulation model used in representing the actual physical system. This clearly requires the simulation model to be validated against the actual system for the simulation-based testing to be valid. Hence, the main emphasis of the flight test is in the validation of the models used for simulation and controller performance and robustness testings.

In this chapter, the flight controller developed in Chapter 5 undergoes a series of systematic performance validation testing before the synthesized controller is implemented in the UAV system for actual flight testings. Details of the setup used for the integrated flight control development tests, software and hardware-in-the-loop testings, are covered. Performance validation flight tests are conducted to test the synthesized controller. Flight test results are used to compare with the simulation-based test results.

## 6.1 Integrated Framework for Flight Control Development Testing

The integrated framework for flight control development provides a systematic and progressive test environment for testing the synthesized controllers. Figure 6.1 shows the four progressive steps involved in testing of flight controllers. In each setup steps, different aspects and issues of controller synthesis and implementations are tested and verified. This provides an easy way of debugging and identifying any design or implementation issues within the development cycle. Hence it is important to know the differences between each of the test setups to better identify the source of the problem. For example, if good performance is achieved in software-in-the-loop (SIL) testing but the same controller results in poor performance in processor-in-the-loop (PIL) testing, the reason for the poor performance in PIL test environment might not be due to poor controller rather a characteristics of the PIL was not modeled correctly. For example, it might be due to a time delay issue in the PIL testing which is absent in the SIL test setup.

During the controller testing process, the model and control design are updated iteratively to achieve the desired closed-loop performance objectives. This tight integration between the controller synthesis and testing using the model developed provides validation for both the synthesized controller and the model developed at the same time.

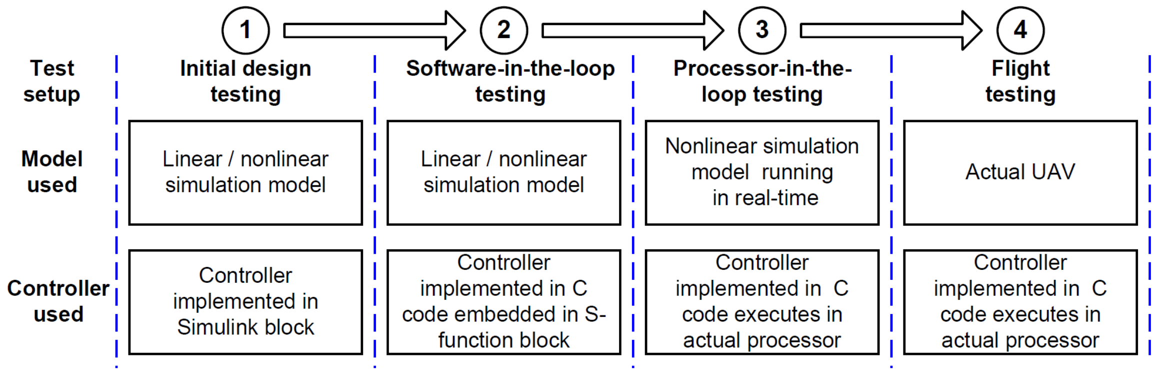
1
2
3
4
Test setup
Initial design testing
Software-in-the-loop testing
Processor-in-the-loop testing
Flight testing
Model used
Linear / nonlinear simulation model
Linear / nonlinear simulation model
Nonlinear simulation model running in real-time
Actual UAV
Controller used
Controller implemented in Simulink block
Controller implemented in C code embedded in S-function block
Controller implemented in C code executes in actual processor
Controller implemented in C code executes in actual processor

Figure 6.1: Integrated framework for flight control development testing

### 6.1.1 Initial Design Testing

Initial design testing is the first step used to test the synthesized controller. The discrete-time controller (obtained from Section 5.5.2) is implemented in Simulink to validate the closed-loop performance with the nonlinear simulation model. This testing verifies the designed controller is able to meet the design requirements.

### 6.1.2 Software-in-the-loop Testing

The second step is implementation of the controller in C code as an embedded S-function block. The controller can now be tested via SIL testing in the Matlab/Simulink environment. The purpose of the SIL testing is to validate the correctness and implementation of the controller C code implementation.

### 6.1.3 Processor-in-the-loop Testing

The PIL testing is used to test the successful C code controller from SIL testing to the actual flight computer in the third step. This provides an actual test of the implemented flight control codes in the actual flight computer processor. In addition to the flight control code running on the embedded processor, other software sub-modules of the autopilot system

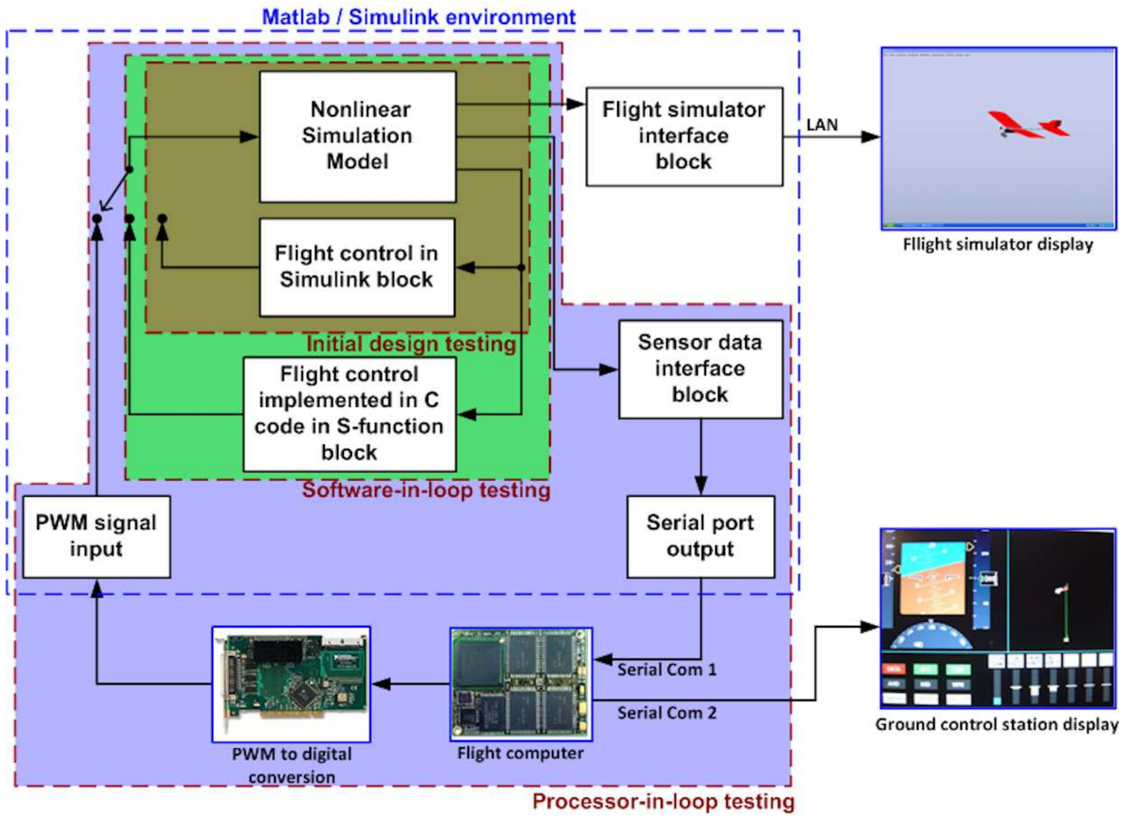
Matlab / Simulink environment
Nonlinear Simulation Model
Flight control in Simulink block
Initial design testing
Flight control implemented in C code in S-function block
Software-in-loop testing
Flight simulator interface block
LAN
Fllight simulator display
Sensor data interface block
Serial port output
PWM signal input
Serial Com 1
Serial Com 2
Ground control station display
PWM to digital conversion
Flight computer
Processor-in-loop testing

Figure 6.2: Flight control development testing architecture: Initial design, software-in-the-loop and processor-in-the-loop testing

such as attitude determination algorithm, data acquisition and telemetry communication modules are running at the same time to form a complete functional, standalone autopilot system. The differences between SIL and PIL testing are:

- SIL testing uses perfect attitude data ($\phi$, $\theta$ and $\psi$) but the PIL testing uses attitude data from real-time AHRS attitude determination algorithm.
- SIL testing uses exact control commands output from the flight control algorithm to provide closed-loop control with the simulation model. In the PIL testing, the flight computer system outputs actual PWM control signals to the servo actuators. A counter/timer data acquisition board is used to acquire the controller commands for closed-loop control of the simulation model.

- PIL testing is carried out with flight computer system and simulation model operating in real-time with serial communication and data acquisition board interfaces. The hardware components in the system may result in time delays associated with each of the hardware devices or processes. However in SIL testing, no external hardware components are involved and all the processes run on a single simulation environment with a single clock time.

### 6.1.4 Flight Testing

Flight testing provides actual test of the complete flight control system and the nonlinear simulation model in real flight environment. The exact flight control code that was used in the PIL testing is implemented in the UAV flight computer system for flight testing. The flight test provides dynamic response of the UAV with environmental disturbance factors such as wind gust effect. This data is used to validate the simulation model and the performance of the flight control system implemented.

## 6.2 Processor-in-the-loop Simulator

The PIL simulator provides an intermediate step to test the synthesized controller on actual hardware target processor before the controller is put on actual flight test. This approach offers the following advantages:

- Ability to test and identify controller implementation issues before flight testing. This helps to determine controller implementation limitations on actual hardware system and provides important information for controller redesign.

- Provides a real-time environment for testing synthesized controllers.

- Provides a good testbed for hardware and software system integration so that the functionality of components can be tested at a system level. This helps ensure the integrated system has high integrity and free of fault.

- Provides simulation environment for RC pilots and flight test engineers to prepare, train and understand the scope of flight trial and gains confidence with the UAV system.

Beside testing, debugging and validating flight control design and implementation, the PIL simulator can be used for post-flight analysis such as validating simulation model used with updated flight test data. Once the simulation model has been sufficiently validated, it can be used to augment and substitute many of the flight test trials and helps to reduce the risk and development cost for the UAV systems.

### 6.2.1 PIL Simulator System Setup

The PIL simulator setup is an extension of SIL setup that includes actual embedded target processor (flight computer) and flight simulator display. During the simulation, the simulation environment outputs sensor data through a communication link to the target processor that executes the embedded software code in real-time. The flight computer uses the fed back sensor data to generate control signals which are sent back to the simulation model using another communication link to control the aircraft simulation model. Hence the software simulation and flight computer formed a closed-loop control system (as shown in Figure 6.3).

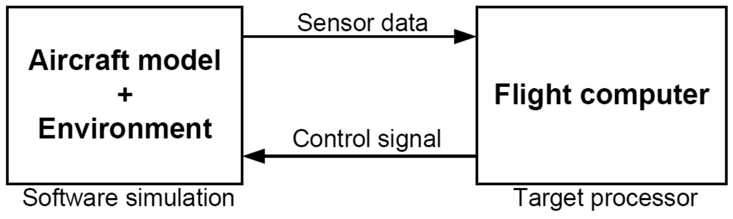

Figure 6.3: Overview of PIL simulation concept

#### 6.2.1.1 PIL Software System Architecture

The PIL simulation model uses the same nonlinear simulation model as in the SIL testing. For the simulation model to execute in real-time on desktop computer, Real-Time Windows Target (RTWT) toolbox is used. The RTWT software provides real-time execution of the generated C code to run on Windows operating system. The generated C code is able to interact with external hardware systems using the input/output (I/O) devices within the desktop computer. The entire C code generation and binary executable file are automatically generated with RTWT toolbox [61].

The I/O blocks from RTWT toolbox are added to the nonlinear aircraft simulation model developed in Chapter 2. These I/O blocks, stream data output, stream data input and PWM DAQ (shown in Figure 6.4), allow the simulation model to interface with the data inputs and outputs to the flight computer and simulator. The stream data input uses the User Datagram Protocol (UDP) to send data to the flight simulator while the stream data output block uses serial communication protocol to send sensor data to the flight computer. The PWM DAQ block acquires control signals from the flight computer using a timer/counter board in the desktop computer. Figure 6.4 shows the Simulink block diagram layout used for the auto-code generation in the PIL simulation. For auto-code generation, a discrete sampling time has to be defined and it is set to 0.02 seconds. This is the maximum time step size that can be used so that the PIL simulator can output sensor data at 50 Hz, which is the same data output rate used in the actual IMU/GPS sensor.

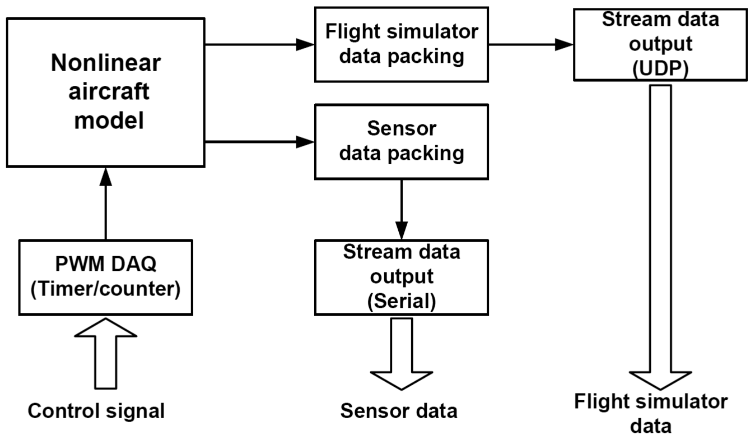

Figure 6.4: PIL simulator Simulink block architecture

#### 6.2.1.2 PIL Hardware System Architecture

The PIL hardware system setup is duplicate of the actual flight computer system on the UAV except for the IMU/GPS sensor and data modem. Figure 6.5 shows the architecture of the hardware system setup. The desktop computer runs both the RTWT simulation and FlightGear flight simulator programs in real-time. The FlightGear flight simulator receives simulation data using UDP communication at 5 Hz from the RTWT simulation. Serial communication port 1 provides serial sensor data output at 50 Hz with 38.4 Kbps baud rate to the MPC 555 flight computer while the timer/counter board provides servo commands inputs to the simulator via desktop PCI bus.

The failsafe board is a multiplexer board used to switch the PWM control output signals to the servo actuators between manual pilot and autopilot mode using the RC transmitter. This functionality allows the PIL simulator to simulate the same scenario as in the actual flight test where the RC pilot performs manual flight before switching to autopilot mode during the flight to test the autopilot system. The ground control station allows monitoring of real-time flight data from the flight computer. The flight data can be recorded for analysis purpose. Figure 6.6 shows the PIL simulator system.

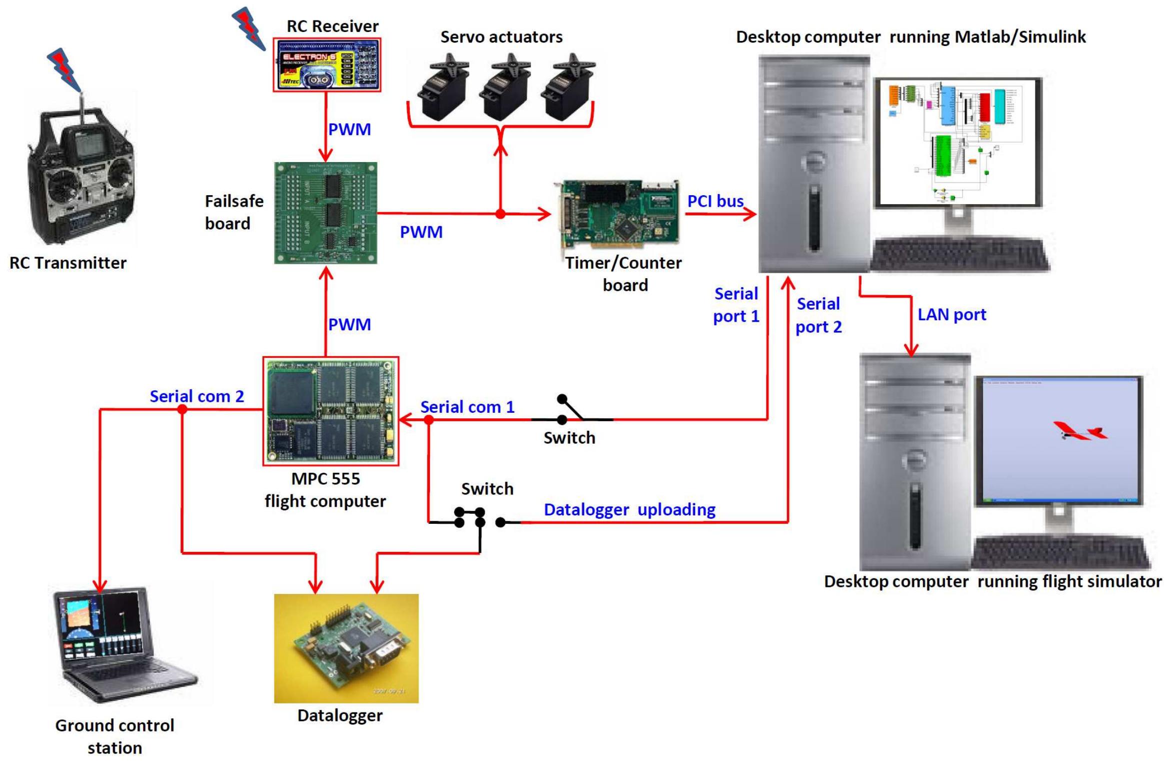

Figure 6.5: PIL simulator hardware system setup

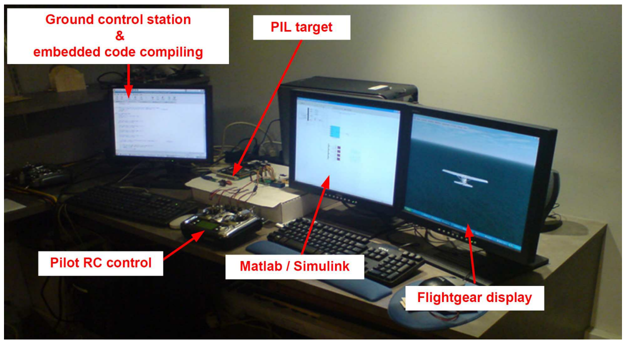

(a) PIL station

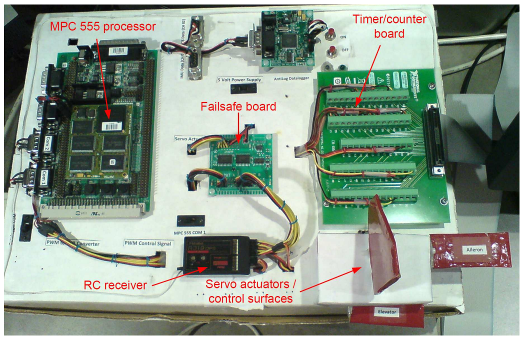

(b) PIL hardware system

Figure 6.6: PIL simulator setup

### 6.2.2 PIL System Operation Verification

The objective of the PIL simulator is to provide a realistic representation of the actual UAV system operation. To determine how well the simulator performs and its limitations, verification of the system operation has to be done. This verification focuses on three important areas of the PIL system setup that are critical for its successful operation in representing the actual system.

- Sensor output data from simulator to flight computer
- Control input data from flight computer to simulator
- Time delay of simulator closed-loop system

#### 6.2.2.1 Verification of Sensor and Attitude Solution Data

The UAV Simulink nonlinear simulation outputs sensor data with the same packet structure as that of actual IMU/GPS sensor unit. These data are packed and sent through serial communication port to the flight computer which acquires the data and performs real-time attitude determination. Figure 6.7 shows part of inertia sensor data output from the nonlinear simulation model that are sent through serial communication port to the flight computer system. The $\phi$, $\theta$ and $\psi$ euler angles from the nonlinear simulation are not sent to the flight computer. This is because in the actual UAV system operation, these data are not measured from the sensor but are obtained using the attitude determination algorithm.

In SIL testing, the inertia and Euler angles data obtained from the nonlinear simulation model are used directly. However in PIL testing, the Euler angles are estimated using the AHRS attitude determination algorithm and the angular rates and linear accelerations have their biases removed. These bias estimates are obtained from the AHRS algorithm. If the AHRS algorithm performs poorly and calculates very different Euler angles and bias estimates, the result will be the SIL and PIL controller testing outputs being different. The cause of this mismatch would not due to controller synthesis and implementation problem but rather the AHRS algorithm problem.

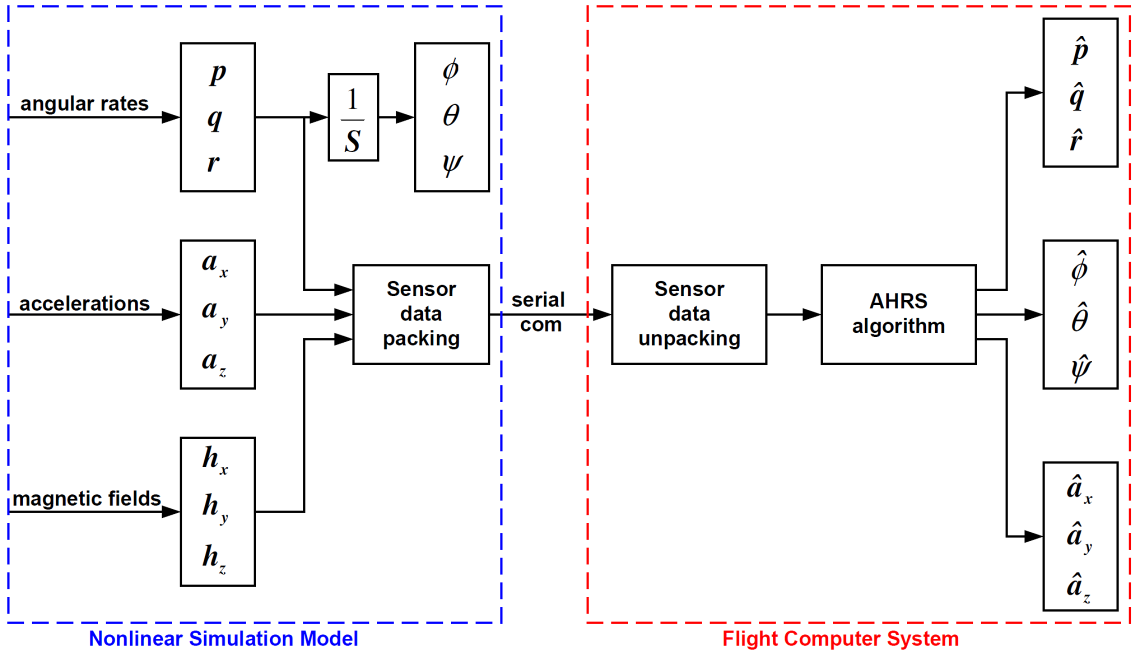

Figure 6.7: Sensor and attitude solution outputs in PIL simulator

Figure 6.8 shows a comparison of sensor data (currently used by the flight control algorithm) between the nonlinear simulation model output ($p$, $q$, $r$, $\phi$ and $\theta$) and the flight computer system output ($\hat{p}$, $\hat{q}$, $\hat{r}$, $\hat{\phi}$ and $\hat{\theta}$). The angular rates data match perfectly since no sensor noise is used in the simulation. However, for the roll and pitch angle, there are some differences in the estimated Euler angles given by the AHRS algorithm as compared to the "truth" Euler angles output from the nonlinear simulation model. This slight differences in the Euler angles will result to some slight differences to the Euler angle tracking responses between the SIL and PIL results. The difference between the two has nothing to do with the controller design or implementation. The addition of attitude determination algorithm in the PIL testing results in additional dynamics in the PIL simulator closed-loop system as compared to the SIL testing setup.

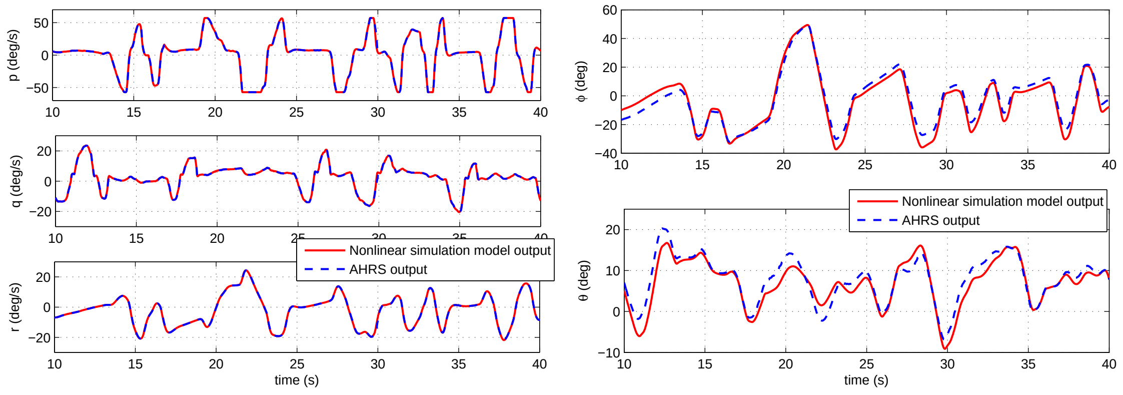

(a) Angular rates (b) Euler angles

Figure 6.8: Comparison of nonlinear simulation model and AHRS algorithm angular rates and Euler angles

#### 6.2.2.2 Verification of Control Input Data

The control input signals generated by the flight computer system are used to drive the servo actuators that actuate the aerodynamic control surfaces. These control signals are in the form of PWM signals. For control actions to control the UAV simulation model in closed-loop, the PWM control signals have to be acquired by the timer/counter data acquisition card (shown in Figure 6.5). It is important to ensure that the control signals generated by the flight computer system are accurately acquired into the simulation model for closed-loop control. Figure 6.9 shows details of the control signal flow diagram and signal conversion in the PIL simulator. To verify that the control signals output from the flight computer system are the same as that acquired into the simulation model, control signals at **C1** and **C2** (Figure 6.9) are recorded during closed-loop PIL testing.

Figure 6.10 shows plot of two control signals, aileron and elevator control, at **C1** and **C2**. Note that this plot does not account for time delay between the measurement point

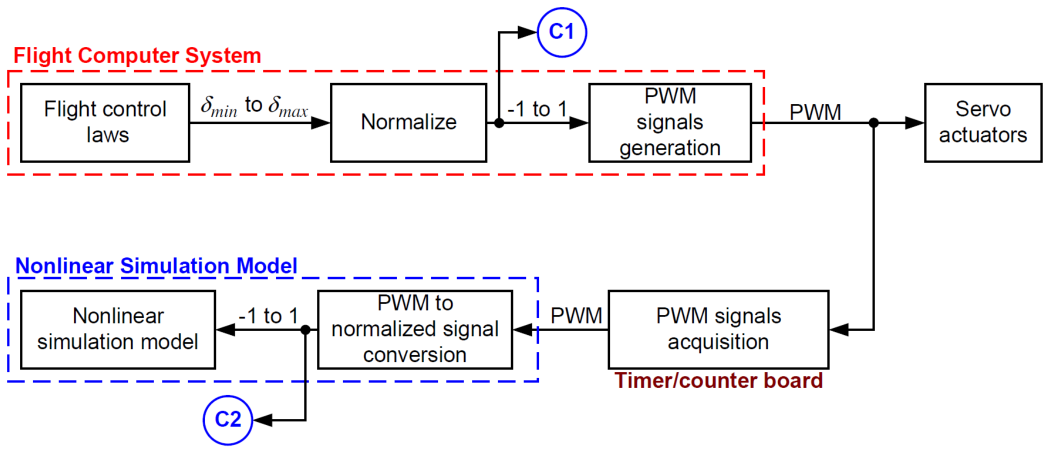

Figure 6.9: Control signal flow diagram

at **C1** and **C2**. The time delay effect will be addressed in the next section. From the plot, the aileron and elevator control signals at **C1** and **C2** matches perfectly. This verifies that the control signals output from the flight computer system are accurately acquired into the simulation model for closed-loop PIL testing.

#### 6.2.2.3 PIL Simulator Closed-loop System Time Delay

The PIL simulator is made up of different hardware components integrated together. With different hardware devices and signals flow between them occurring at the same time, there will be time delay within the simulator since it takes finite amount of time to process, pack, send or receive data from one device to the other. For closed-loop control in the PIL simulator, this aggravates the time delay problem since the feedback action goes through a daisy chain with all the devices in a loop. For example, the simulation model has to send out sensor data to the flight computer before the flight computer can generate the required control signals to the failsafe board and subsequently the failsafe board has to send the control signals to the timer/counter board before the control signals are acquired back into the simulation model for closed-loop control.

The time delay effect for a closed-loop control system is important as it reduces the stability margin and bandwidth of the closed-loop system. In the PIL simulator setup, the time delay effect will impose a limitation on testing of the controllers since a large time

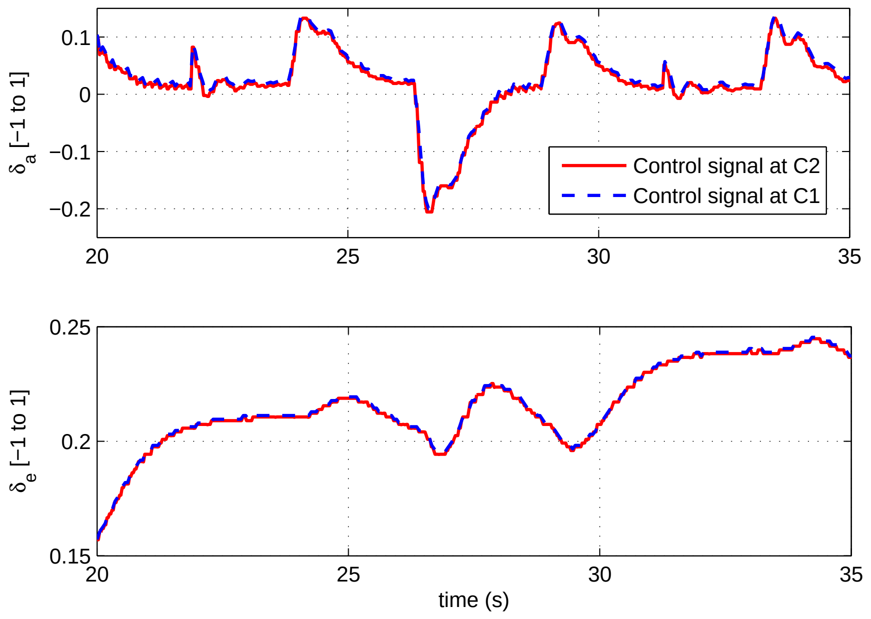

Figure 6.10: Verification of control signals in PIL simulator

delay in the simulator will limit the ability to test high bandwidth controllers. Also, for the $H_\infty$ and $\mu$ controllers that are to be tested using the PIL simulator, the time delay in the simulator has to be included during the controller synthesis.

The time delay to be determined is the time required for a signal generated from the simulation model to be sent to the flight computer system, process the data and sent back to the simulation model. During the time delay measurement, the simulation model and flight computer system are configured to execute the same simulation and flight control routines to ensure that the simulator is using the same computation load as in normal PIL testing. The approach used to measure the time delay is to add an addition toggle logic in the flight control algorithm such that once it receives the toggle signal, it will send a control signal back to the simulation model. The toggle signal used to toggle this logic in the flight computer system is sent from the simulation model. This allows the time history of outgoing toggling signal and incoming control signal to be measured and recorded using a common time stamp within the simulation environment. The time delay between the outgoing toggle signal and the incoming control signal is the closed-loop time delay for the

PIL simulator.

Figure 6.11 shows time history plot of the toggle signal and control signal that are measured in the simulation environment. The time gap between the start of the toggle signal and time where the incoming control signal changes is the time delay for the closed-loop process. The time delay measured is approximately 0.08 seconds. The measured time delay is associated with the total time delay of the closed-loop system. This approach is unable to identify a time delay in each of the process. Therefore it is impossible to know if majority of the time delay is contributed from the flight computer system hardware components used or from the additional components, such as timer/counter board, used in the PIL simulator.

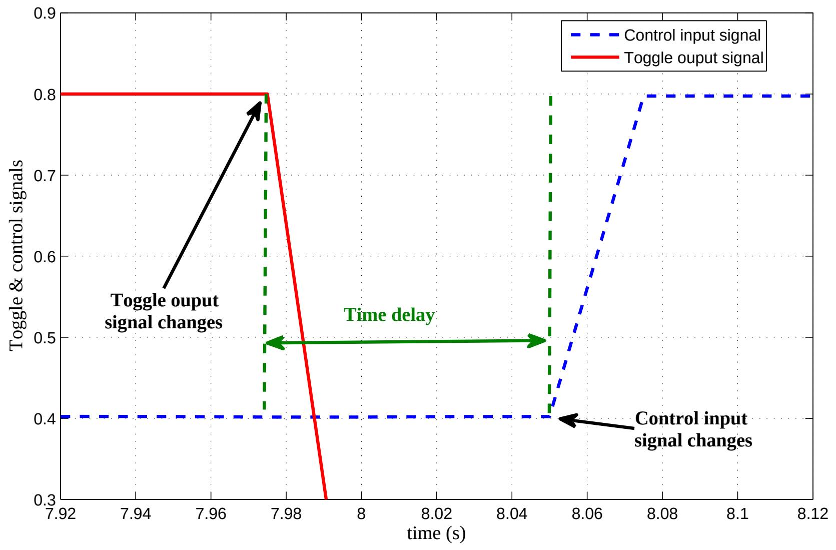

Figure 6.11: Time delay measurement in PIL simulator

It is assumed that the time delay measured from the PIL simulator is the same in the actual UAV system. This assumption is made because it is not possible to measure the time delay in the same way with the actual UAV system using the current instrumentation onboard of the UAV. However, since the PIL simulator setup duplicates almost all the hardware components used on the UAV system, it is reasonable to expect that the time delay for the flight control system of the UAV should not be very different from the PIL simulator system.

## 6.3 Integrated Framework Flight Control Synthesis and Validation

In this section, the modeling, simulation and analysis framework developed will be integrated together for validation of designed controllers. The task of controller synthesis and validation are closely related since it is an iterative process to design and validate the designed controller to achieve the required performance specifications. Different incremental levels of controller testing and validation are performed using the integrated framework. This will be illustrated with the $\mu$ roll angle controller from Chapter 5.

### 6.3.1 Flight Test Validation Setup

A well-designed validation experiment is necessary to provide a realistic and consistent set of test conditions across different levels of controller testing within the integrated framework. This helps to provide a direct and meaningful comparison for closed-loop system performance results and gives useful information for controller redesign if necessary.

#### 6.3.1.1 Design of Reference Command Signal

The performance objective for the roll angle controller design is to provide reference roll angle ($\phi_{ref}$) tracking. In this case, a filtered doublet reference roll angle is used to provide a smooth and piecewise continuous reference roll angle tracking signal as oppose to a normal doublet signal ($\phi_{dbt}$). This approach is taken for practical controller testing in the actual flight test and also for practical application of tracking a smooth reference roll angle. A second order low pass filter, with rise time of 0.7 second and damping of 0.85, smoothes the doublet command. The transfer function of the filter is given by:

$$TF_{\phi_{dbt} \to \phi_{ref}} = \frac{6.612}{s^2 + 4.371s + 6.612}$$

The amplitude of the roll angle demand is chosen to be $\pm$ 20 degrees so that it remains within the controller designed operating envelope. The period of the doublet signal is selected to be 2.5 seconds so that this will provide a signal with excitation frequency content (Equation 3.10) less than the maximum frequency limit of the identified model used in the controller design. Figure 6.12 shows the difference between normal and filtered doublet reference roll angle commands.

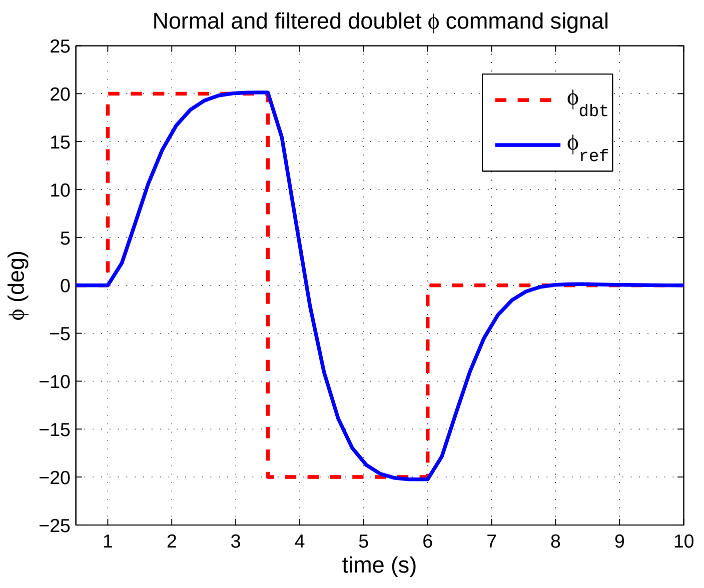

Figure 6.12: Normal and filtered $\phi$ doublet commands

To ensure a consistence and repeatable reference command signal is being input during all the tests, the $\phi_{ref}$ signal profile is pre-programmed and generated by the flight computer system. Figure 6.13 shows time history of $\phi_{ref}$ signal designed for the validation experiment. This form of $\phi_{ref}$ signal profile is commonly used during UAV waypoint navigation flight. The $\phi_{ref}$ signal is divided into 3 parts:

- $0 \leq$ t $<$ 2 seconds: The $\phi_{ref}$ is zero. This is to provide zero roll angle reference tracking for the roll angle controller as well as achieving a wing-leveled flight before the filtered doublet roll angle command is executed.

- $2 \leq$ t $<$ 9 seconds: The filtered doublet roll angle command is executed. This provides a dynamic reference roll angle tracking for the designed controller.

- $9 \leq$ t $<$ 11 seconds: The $\phi_{ref}$ is zero. This is to command the UAV back to wing-leveled flight again to complete the validation experiment which the RC pilot can easily assume manual control of the UAV at a trim position.

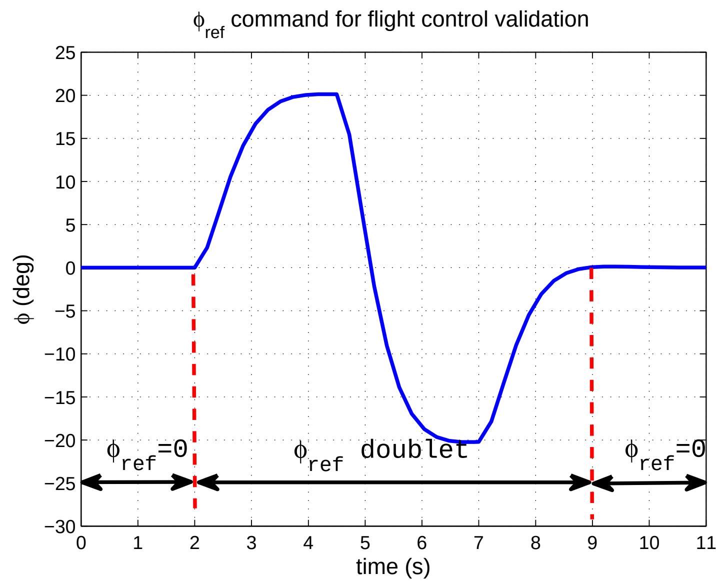

Figure 6.13: Time history of $\phi_{ref}$ used for validation experiment

### 6.3.1.2 Validation Test Setup

Beside using an exact sequence of $\phi_{ref}$ command for all the validation experiments, the flight conditions and setup of the experiments have to be the same so that the controller tracking performance can be compared between different sets of validation experiment. In the SIL and PIL testing, this can be easily configured in the simulation setup. However, for actual flight testing, it is not easy to have the same flight conditions. This is because there are ambient environment factors such as wind gust disturbance that cannot be controlled during the flight test. These environmental disturbances are difficult to include in the SIL and PIL testing since it is not easy to measure these variables during the flight tests. Hence, precautions are taken to conduct the flight tests with minimal deviation from the flight conditions used in the SIL and PIL testing.

The flight conditions used in the validation experiment is given by the desired operating condition in Table 3.1. The sequence of $\phi_{ref}$ command starts when the autopilot system is engaged by the RC pilot. In the autopilot mode, the PID pitch angle controller described in Section 5.3.1 is engaged so that this helps to provide a zero pitch angle flight condition while the roll angle controller is tracking the $\phi_{ref}$ command. The only control that the RC pilot has while the autopilot is engaged is the throttle control. This is used to regulate the UAV airspeed so that it is able to maintain at the desired airspeed condition throughout the flight test.

### 6.3.2 Initial Design Testing

The first level of controller testing is done using the discrete-time reduced order $\mu$ controller from Section 5.6.4 implemented into the flight control Simulink block. Closed-loop Monte-Carlo simulation runs with model uncertainty perturbations are performed. Figure 6.14 shows the $\phi$ angle tracking result obtained from 50 simulation runs. The result shows that the designed controller is able to track the $\phi_{ref}$ command well with about 0.5 seconds time delay.

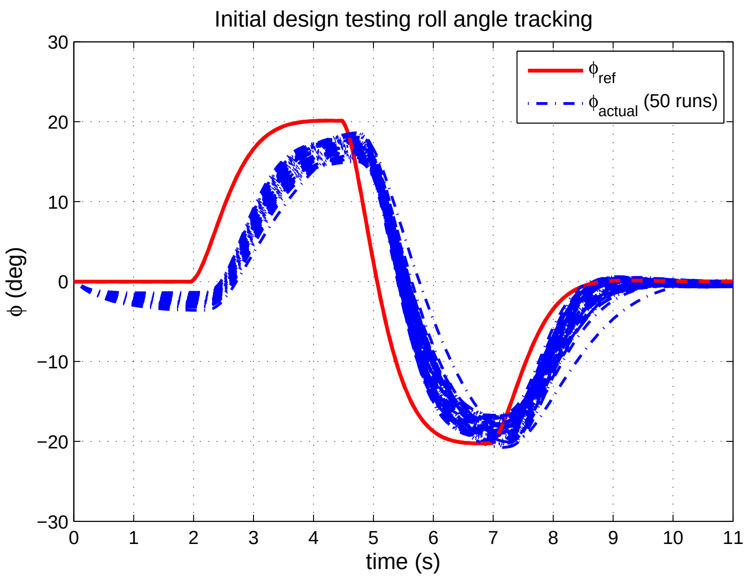

Figure 6.14: $\phi$ angle tracking for initial design testing

### 6.3.3 Software-in-the-loop Testing

The same reduced order $\mu$ controller is implemented in C and embedded into the Matlab's S-function block for SIL testing. 50 Monte-Carlo simulation runs are performed with the uncertain nonlinear simulation model. Figure 6.15 shows the result of the $\phi$ angle tracking. The SIL $\phi$ angle tracking performance obtained is almost the same as the result obtained from the initial design testing. The result indicates that the controller implemented in C is correct and the implemented C code can be port to the flight computer system for PIL testing.

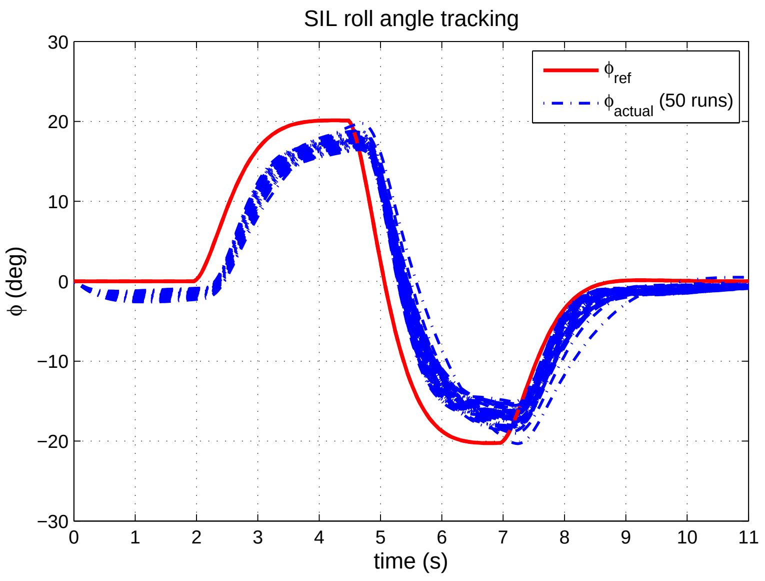

Figure 6.15: $\phi$ angle tracking for SIL testing

### 6.3.4 Processor-in-the-loop Testing

The C implementation of the controller successfully tested in the SIL testing was complied with the full autopilot program code and uploaded into the MPC 555 flight computer system for PIL testing. The PIL testing is done in the exact same manner as in actual flight test where the RC pilot needs to fly the aircraft in the manual mode, trim the aircraft and switch over to autopilot mode to test the controller. The setup of the PIL simulator flight environment is exactly the same as that in the simulator parameter tuning described in

Section 2.2.1.4.

Automated Monte-Carlo simulation runs used in the initial design and SIL testing cannot be used in PIL testing as the flight computer system is running the actual standalone autopilot routine that cannot be reset instantaneously for each different Monte-Carlo simulation run. Therefore manual variation of model uncertainty conditions was performed in each of the PIL testing run.

Selective model uncertainty conditions are chosen for the PIL testing to limit the number of PIL testing runs. The worst-case gain analysis tools described in Section 4.3.1 is used to determine the closed-loop system worst-case gain condition due to model uncertainty perturbations. This helps to provide the worst-case model uncertainty conditions for the PIL testings.

Figure 6.16 shows result of the worst-case gain analysis of the closed-loop system using the system interconnection in Figure 5.4 with parametric uncertainties in the UAV lateral model. For frequency range between 0.5 to 10 rad/s, 10 different combinations of parameter values result to the worst-case gain condition at each of the frequency point within this frequency range. Hence, these combinations are chosen and used for the PIL testings. Figure 6.17 shows the result obtained from PIL testings using each of the combination of uncertainty parameters at the worst-case gain. The roll angle tracking performance obtained is similar to the result obtained from the SIL testing.

### 6.3.5 Flight Testing

Flight test of the UAV was conducted with the exact same autopilot program code tested in the PIL testing. The conduct of the flight test is carried out in the same way as the PIL testing, where the RC pilot needs to fly and trims the aircraft before engaging the autopilot at desired operating condition. Multiple test runs with the controller are carried out during the flight test. In each of the run, the RC pilot trimmed the aircraft in the direction of head wind so that the controller is tested in a minimal cross-wind condition.

Figure 6.18 shows the roll angle tracking performance obtained from the flight test runs where $t = 0\ s$ (origin) is the time the autopilot is engaged. The initial roll angles from all the runs are different since this is dependent on how well the RC pilot managed to

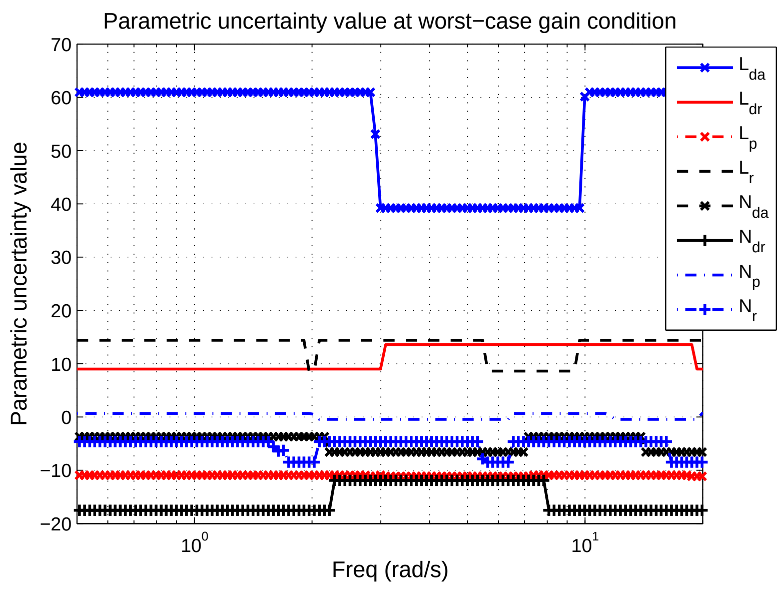

Figure 6.16: Parametric uncertainty values of closed-loop system at worst-case gain condition

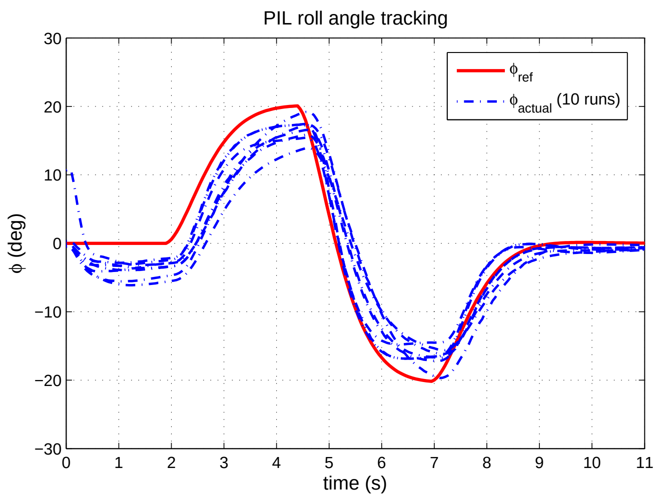

Figure 6.17: $\phi$ angle tracking for PIL testing

trim the aircraft to wing-leveled flight before engaging the autopilot. However, regardless of the initial roll angle positions, the roll angle controller is able to track the reference command signal, similar to the responses obtained from the initial design, SIL and PIL testing. Repeatable and consistent tracking responses are achieved for the five different flight test runs shown in Figure 6.18. The only difference between the flight test results and the initial design, SIL and PIL testing results is that some high frequency oscillations are observed in the flight test roll angle tracking responses. This might be due to other external disturbances or high frequency model dynamics not accounted for during the controller synthesis or captured by the model used. Nevertheless, the flight testing result still have good matching with the initial design, SIL and PIL testing. This result helps to validate:

1. Performance of the synthesized controller using the model developed achieves the control design tracking performance objective.

2. Model and model uncertainty developed have adequate fidelity for the controller synthesis and analysis purposes .

3. Framework used for control synthesis and validation is feasible and achieves its intended objectives.

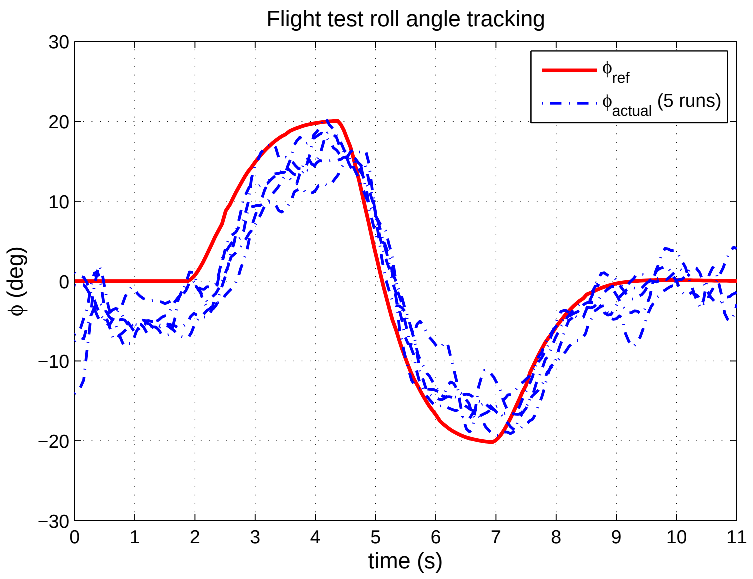

Figure 6.18: $\phi$ angle tracking for flight testing

## 6.4 Applications of Integrated Framework for Performance Analysis

The integrated framework used provides a generic framework and tools for generic flight controller synthesis, validation and analysis applications. This section will illustrate an example application of the integrated framework for validating performance of a $H_\infty$ controller design.

In this setup, two different $H_\infty$ roll angle tracking controllers are designed and implemented using the same setup (weighting functions and performance objectives) described in Section 5.4 with nominal UAV lateral model. One of the $H_\infty$ controllers is designed to have a better performance with $\gamma$ of 1.0 while the other $H_\infty$ controller has a worse off performance with $\gamma$ of 1.6. The $\gamma$ values are chosen such that the better controller will be able to achieve the design performance objectives while the poor controller will not be able to achieve the design performance objectives. The controllers are implemented using the same procedures described in Section 5.5. For each of the implemented discrete-time controller, the controller is reduced to a forth order controller so that both of the implemented controllers have the same order for making a fair comparison.

Prior to the integrated framework testings, robust analysis is performed on the two controllers to analyze the robustness of the controllers subjected to real parametric model uncertainty perturbations in Appendix Table B.5. Figure 6.19 shows the result for the robust analysis. From the robust stability analysis plot in Figure 6.19, both the controllers are robustly stable to the real parametric uncertainty perturbations across the frequencies. However, the robust performance analysis plot in Figure 6.19 shows that the poor performance controller has $\mu$ value of more than 1 in the low frequencies region. The interpretation of $\mu$ greater than 1 in robust performance analysis means that with the real parametric uncertainty variations, the closed-loop system is not able to achieve its performance objectives. This means that the closed-loop system has poor low frequency tracking performance. This is expected because even with the nominal model, the poor performance controller is not able to achieve its performance objectives since it is designed with $\gamma$ value of more than 1.

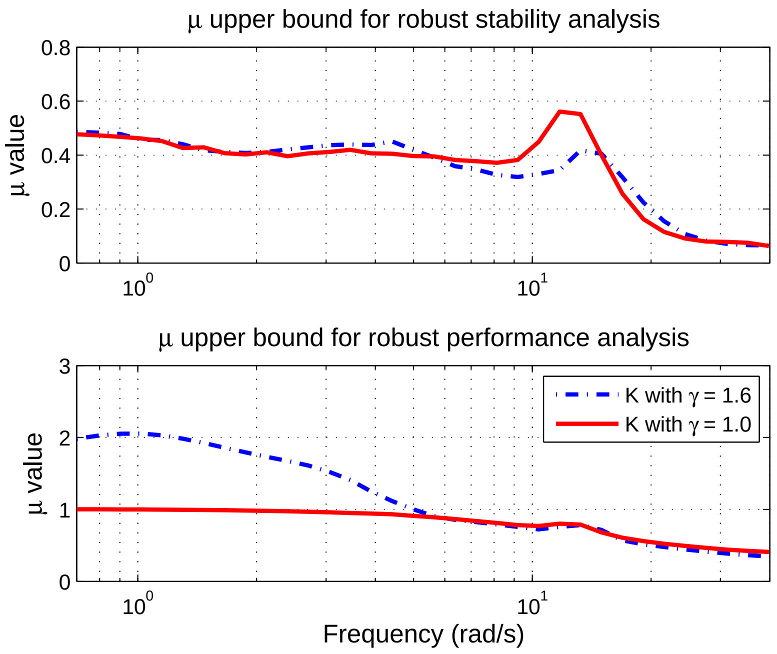

Figure 6.19: Robust analysis of $H_\infty$ controllers with $\gamma$ of 1.0 and 1.6

Next, the two $H_\infty$ controllers are tested using the integrated framework developed to validate their closed-loop performance in SIL and flight tests. The same validation setup described in Section 6.3.1 is used for the tests.

In the SIL tests, 50 Monte-Carlo simulation runs are performed with the uncertain nonlinear simulation model for each of the controller in the closed-loop. Figure 6.20(a) and 6.20(b) show the SIL roll angle tracking performance with the good ($\gamma = 1.0$) and poor ($\gamma = 1.6$) performance controller respectively. The poor performance controller shows poor roll angle tracking performance (Figure 6.20(b)) with large steady-state error as compared to the better performance controller (Figure 6.20(a)). This is consistent with the designed $\gamma$ value since controller with $\gamma$ value of 1.6 has a poor performance as compared to the controller with $\gamma$ value of 1. Both the controllers shows stable closed-loop roll angle tracking responses in Figure 6.20(a) and 6.20(b) and this is consistent with the robust stability analysis results where the $\mu$ values are less than 1 across the frequencies of interest, which means that the closed-loop systems are stable with model uncertainty variations.

The two controllers are loaded onto the UAV flight computer and flight tested using the

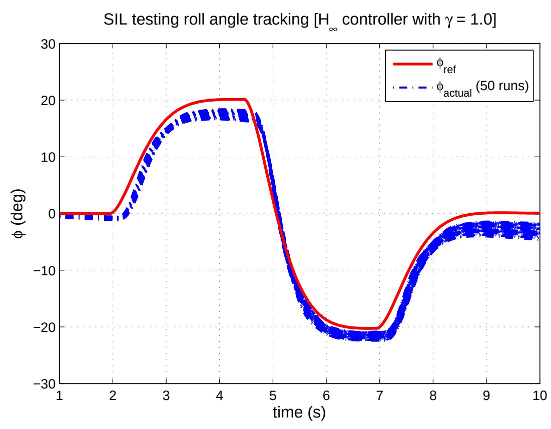

(a) SIL test ($\gamma = 1.0$)

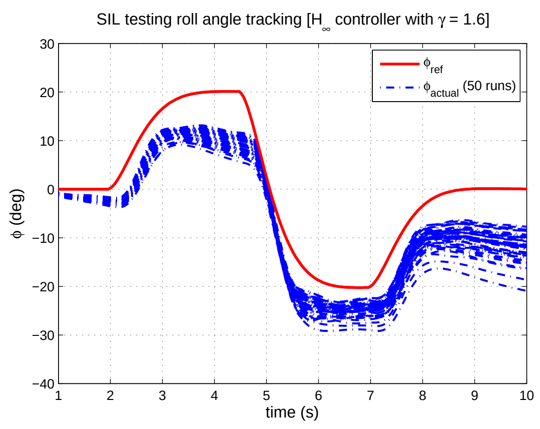

(b) SIL test ($\gamma = 1.6$)

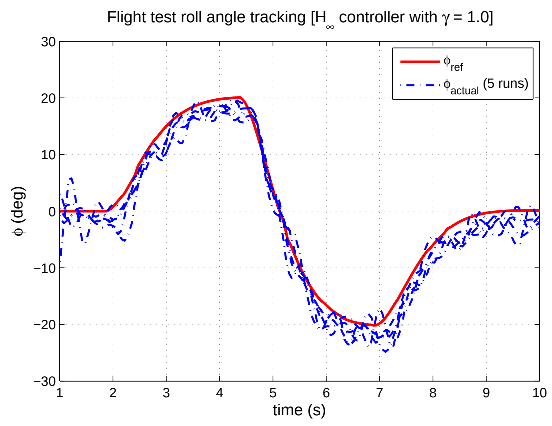

(c) Flight test ($\gamma = 1.0$)

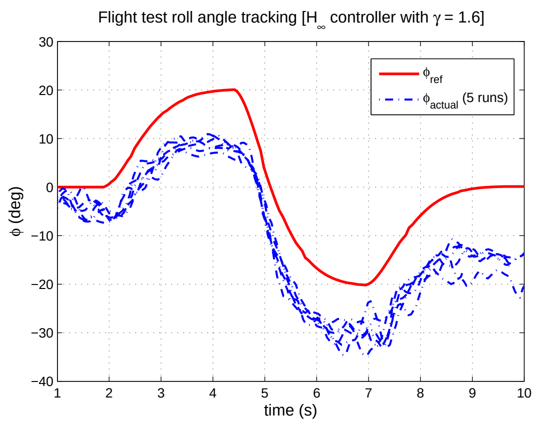

(d) Flight test ($\gamma = 1.6$)

Figure 6.20: SIL and flight test result of $H_\infty$ controllers

same procedure described in Section 6.3.5. Figure 6.20(c) and 6.20(d) show the flight test results of the roll angle tracking performance with the good ($\gamma = 1.0$) and poor ($\gamma = 1.6$) performance controllers respectively. The flight test results show good matching with the SIL testing results. Comparing the SIL testing (Figure 6.20(a)) and flight test results (Figure 6.20(c)) for the good performance controller, both the plots show the same responses. The same result is observed with the worse off performance controller tests in Figure 6.20(b) (SIL testing) and 6.20(d) (flight test). For both of the controllers, the SIL testing results are able to predict and match the actual flight test results well. Again, this shows and proves the success in the integrated framework developed for control synthesis and validation.

# Chapter 7

# Conclusion and Recommendations

## 7.1 Summary

This thesis presented the development of an integrated framework for flight control synthesis and validation with practical application to a small UAV testbed. The main aim of the research is to develop a systematic approach in integrating different processes in model-based flight control development using advance techniques and design tools from initial design to flight testing of the UAV.

The field of disciplines involved in this research is very wide. This includes mathematical modeling of the air vehicle, software and hardware system integration of the UAV system, simulator analysis tools development, flight test system identification and flight control system design. Extensive efforts have been spent in the past 4 years in the development of the integrated framework and procedures to support the UAV flight control system development.

In the aircraft modeling, a 6-DOF nonlinear simulation model was developed based on first principle theory. Moment of inertia measurement experiments and flight simulator parameters tuning were conducted to determine the physical parameters of the vehicle required in the nonlinear simulation model.

To improve the fidelity of the simulation model used, flight test system identification was conducted to update the aerodynamic coefficients in the simulation model. A linear parameterized state-space model was used for time-domain maximum likelihood parameter estimation. Model validation in time and frequency domain of the identified models using flight test validation data showed good matching within the frequency range of input excitation signal used which was derived from the design of experiment. The identified parameters were used to update the aerodynamic coefficients in the nonlinear simulation model by removing the dimensions from these identified parameters.

Parametric uncertainty modeling was used to model the experimental derived parametric uncertainties into the nonlinear simulation model. A systematic approach was provided to model these parametric uncertainties into the nonlinear simulation model so that an LFT model can be extracted using ulinearize procedure. This approach provides a physically meaningful parametric uncertainties in the LFT model. The details of the principles, procedures, accuracy and limitations in using ulinearize for the LFT realization have been presented. Since the LFT model obtained from the ulinearize realization contains a large number of parametric uncertainties, two methods of LFT model simplification, sensitivity analysis and frequency domain overbounding approach, have been proposed to reduce the complexity of the LFT model.

For the flight control synthesis, a flight control architecture was proposed for the UAV autopilot system. In the controller synthesis problem, an autonomous cruise flight condition was chosen. Classical PID controllers were first implemented and manually tuned using flight tests. The roll angle controller was subsequently redesigned using both $H_\infty$ and $\mu$ synthesis with specific performance specifications using the model and model uncertainty developed. The synthesized controller was implemented on the embedded flight computer system. Various practical and important controller implementation issues have also been discussed.

To validate the performance of synthesized controllers, the integrated framework developed was used for testing and validation of the controllers. The framework provides a systematic and progressive approach to test the controllers before the controllers were tested in actual flight tests. The SIL and PIL testings provide good prediction for the closed-loop tracking performance obtained from flight tests. This helps to validate the model and model uncertainty used in the integrated framework as well as validating the performance of the controllers that were designed

The proposed integrated framework for synthesis and validation of flight control system has been successfully applied and demonstrated on the small UAV system and this achieves the objectives of the thesis work.

## 7.2 Recommendations

The current process of controller C code implementation to the embedded flight computer system was done using manual coding. It is desirable to use autocode generation for this process so that it will expedite the controller C code implementation process as well as minimize error in the controller C code implementation.

The validation approach used in this work is based on time domain comparisons of the closed-loop tracking responses. This approach does not provide any quantitative result for the validation process. A better performance validation metric for model, model uncertainty and closed-loop performance needs to be developed to address this problem. This performance validation metric can be extended to real-time flight test validation so that the controller performance can be validated online during flight test.

The flight test system identification performed in this work is limited to two-state lateral model due to the limitation of the current sensor package used on the UAV. A better sensor package with better attitude determination algorithm will help to improve the parameter estimation with a four-state lateral model. This will help to update and improve the fidelity of the nonlinear simulation model.

# Bibliography

[1] H. Chao, Y. Cao, and Y. Chen, "Autopilots for small fixed-wing unmanned air vehicle: A survey," *IEEE International Conference on Mechatronics and Automation*, pp. 3144–3149, 2007.

[2] D. Jung and P. Tsiotras, "Modeling and hardware-in-the-loop simulation for a small unmanned aerial vehicle," *AIAA Guidance, Navigation and Control Conference and Exhibit*, no. 2007-2768, 2007.

[3] I. Kaminer, O. Yakimenko, V. Dobrokhodov, and K. Jones, "Rapid flight test prototyping system and the fleet of UAVs and MAVs at the naval postgraduate school," *Proceedings of the 3rd AIAA Unmanned Unlimited Technical Conference*, 2004.

[4] J. Renfrow, S. Liebler, and J. Denham, "F-14 flight control law design, verification and validation using computer aided engineering tools," *Proceedings of the Third IEEE Conference on Control Applications*, vol. 3, pp. 359–364, 1994.

[5] M. Tischler, *Advances in aircraft flight control.* Taylor and Francis Ltd, 1996.

[6] M. Civita, G. Papageorgiou, W. Messner, and T. Kanadeo, "Design and flight testing of a high-bandwidth $H_\infty$ loop shaping controller for a robotics helicopter," *AIAA Guidance, Navigation and Control Conference and Exhibit*, no. 2002-4836, 2002.

[7] E. Hallberg, J. Komlosy, T. Rivers, M. Watson, D. Meeks, I. K. J. Lentz, and O. Yakimenko, "Development and application of a rapid flight test prototyping system for unmanned air vehicle," *International Congress on Instrumentation in Aerospace Simulation Facilities*, pp. 26.1–26.10, 1999.

[8] R. Smith, G. Dullerud, S. Rangan, and K. Poolla, "Model validation for dynamically uncertain systems," vol. 3, no. 1, pp. 43–58, 1997.

[9] N. M. Jodeh, P. A. Blue, and A. A. Waldron, "Development of small unmanned aerial vehicle research platform: Modeling and simulating with flight test validation," *AIAA Modeling and Simulation Technologies Conference and Exhibit*, no. 2006-6261, 2006.

[10] eCos. Homepage. [Online]. Available: http://ecos.sourceware.org/

[11] J. S. Jang and D. Liccardo, "Automation of small UAVs using a low cost MEMS sensor and embedded computing platform," Crossbow Technology Inc., Tech. Rep.

[12] Phytec. MPC555 microcontroller datasheet. [Online]. Available: http://www.phytec.com/products/sbc/PowerPC/phyCORE-MPC555.html

[13] Crossbow. Micronav sensor datasheet. [Online]. Available: http://www.xbow.com/Products/Product_pdf_files/Inertial_pdf/uNAV_Datasheet.pdf

[14] Maxstream. XTend RF data modem datasheet. [Online]. Available: http://www.digi.com/products/wireless/long-range-multipoint/xtend-module.jsp

[15] Horizon_Hobby. Spektrum DX7 RC radio system datasheet. [Online]. Available: http://www.spektrumrc.com/Products/Default.aspx?ProdID=SPM2710l

[16] Reactive_Technologies. RxMux failsafe switch datasheet. [Online]. Available: http://reactivetechnologies.com/RxMux.html

[17] Anticyclone_System. Antilog RS232 serial datalogger datasheet. [Online]. Available: http://www.anticyclone.myzen.co.uk/product_antilog.html

[18] Unmanned_Dynamics. Aerosim blockset homepage. [Online]. Available: http://www.u-dynamics.com/aerosim/default.htm

[19] Unmannned_Dynamics_LLC, *Aerosim Blockset Version 1.2 User's Guide,*. -, 2003.

[20] R. Nelson, *Flight Stability and Automatic Control.* McGraw-Hill Science/Engineering/Math, 1997.

[21] Y. C. Paw and G. J. Balas, "Uncertainty modeling, analysis and robust flight control design for a small UAV system," *AIAA Guidance, Navigation, and Control Conference*, no. 2008-7434, 2008.

[22] M. Abdulrahim and R. Lind, "Control and simulation of a multi-role morphing micro air vehicle," *AIAA Guidance, Navigation and Control Conference and Exhibit*, no. 2005-6481, 2005.

[23] B. Owens, D. Cox, and E. Morelli, "Development of a low-cost sub-scale aircraft for flight research: The FASER project," *AIAA Aerodynamics Technology and Ground Testing Conference*, no. 2006-3306, 2006.

[24] FlightGear. Homepage. [Online]. Available: http://www.flightgear.org/

[25] Horizon_Hobby. Power 25 outrunner motor specifications. [Online]. Available: http://www.horizonhobby.com/Products/Default.aspx?ProdID=EFLM4025A

[26] MotoCalc. Homepage. [Online]. Available: http://www.motocalc.com/

[27] K. Kotwani, S. Sane, H. Arya, and K. Sudhakar, "Experimental characterization of propulsion system for mini aerial vehicle," *31st National Conference on Fluid Mechanics and Fluid Power*, pp. 671–678, 2004.

[28] M. P. Merchant, "Propeller performance measurement for low reynolds number unmanned aerial vehicle applications," Master's thesis, Wichita State University, 2004.

[29] B. Mettler, *Identification Modeling and Characteristics of Miniature Rotorcraft.* Springer, 2002.

[30] M. Tischler and R. Remple, *Aircraft and rotorcraft system identification: Engineering methods with flight-test examples.* AIAA, 2006.

[31] R. V. Jategaonkar, *Flight Vehicle System Identification: A time domain Methodology.* AIAA, 2006.

[32] V. Klein and E. A. Morelli, *Aircraft system identification: Theory and Practice.* AIAA, 2006.

[33] L. Ljung, *System Identification: Theory for the user.* Prentice Hall, 1999.

[34] E. A. Morelli, “Flight test of optimal inputs and comparison with conventional inputs,” *Journal of Aircraft*, vol. 36, no. 2, pp. 389–397, 1999.

[35] J. L. Crassidis and J. L. Junkins, *Optimal Estimation of Dynamic Systems.* Harpman & Hall/CRC, 2004.

[36] T. M. Foster and W. J. Bowman, “Dynamic stability and handling qualities of small unmanned-aerial-vehicle,” *AIAA Aerospace Sciences Meeting and Exhibit*, no. 2005-1023, 2005.

[37] S. Skogestad and I. Postlethwaite, *Multivariable feedback control: Analysis and Design.* Wiley, 2005.

[38] C. M. Belcastro, “Uncertainty modeling of real parameter variation for robust control applications,” Ph.D. dissertation, Drexel University, 1994.

[39] G. Balas, R. Chiang, A. Packard, and M. Safonov, *Robust Control Toolbox 3 User’s Guide.* The MathWorks, 2007.

[40] M. Idan and G. E. Shaviv, “Robust control design strategy with parameter-dominated uncertainty,” *Journal of Guidance, Control and Dynamics*, vol. 19, no. 3, pp. 605–611, 1996.

[41] A. Varga, G. Looye, D. Moormann, and G. Grübel, “Automated generation of LFT-based parametric uncertainty descriptions from generic aircraft models,” *Mathematical and Computer Modelling of Dynamical Systems*, vol. 4, no. 4, pp. 249–274, 1998.

[42] S. Hecker and A. Varga, “Generalized LFT-based representation of parametric uncertain models,” *European Journal of Control*, vol. 10, no. 4, pp. 326–337, 2004.

[43] T. Mannchen, D. G. Bates, and I. Postlethwaite, “Modeling and computation worst-case uncertainty combinations for flight control systems analysis,” *Journal of Guidance, Control and Dynamics*, vol. 25, no. 6, pp. 1029–1039, 2002.

[44] R. Kureemun, D. G. Bates, and M. J. Hayes, "On the generation of LFT-based uncertainty models for flight control law robustness analysis," *AIAA Guidance, Navigation, and Control Conference*, no. 2001-4396, 2001.

[45] F. R. Chavez and D. K. Schmidt, "Uncertainty modeling for multivariable-control robustness analysis of elastic high speed vehicles," *Journal of Guidance, Control and Dynamics*, vol. 22, no. 1, pp. 87–95, 1999.

[46] J. M. Biannic and C. Doll, "Introduction to a Simulink-based interface for LFRT toolbox," *Free web publication http://www.cert.fr/dcsd/idco/perso/Biannic/download/slklfr.pdf*, 2006.

[47] J. F. Magni, "Linear fractional representation toolbox [version 2.0] for use with Matlab," *Free Web publication http://www.cert.fr/dcsd/idco/perso/Magni/*, 2006.

[48] D. Bates and I. Postlethwaite, *Robust Multivariable Control of Aerospace Systems.* Delft University Press, 2002.

[49] D. K. Schmidt and S. K. Lee, "New results in structured uncertainty modeling for flexible flight vehicles," *AIAA Guidance, Navigation, and Control Conference*, no. 99-4157, 1999.

[50] T. Lombaerts, J. Mulder, and G. Voorsluijs, "Design of a robust control system for a mini-UAV," *AIAA Guidance, Navigation, and Control Conference and Exhibit*, no. 2005-6408, 2005.

[51] H. Hindi, C. Y. Seong, and S. Boyd, "Computating optimal uncertainty models from frequency domain data," *IEEE Conference on Decision and Control*, vol. 3, pp. 2898–2905, 2002.

[52] K. E. Haggblom, "Data-based modeling of block-diagonal uncertainty by convex optimization," *American Control Conference*, pp. 4637–4642, 2007.

[53] G. J. Balas, A. K. Packard, and P. J. Seiler, "Uncertain model set calculation from frequency domain data," *In:P. M .J Van den Hof, P. S. C. Heuberger, C. W. Scherer Se-*

*lected Topics in Model-Based Control: Bridging Rigorous Theory and Advanced Technology, Springer-Verlag*, 2009.

[54] Z. Xing and D. Gebre-Egziabher, "Modeling and bounding low cost inertial sensor errors," *IEEE/ION Position, Location and Naviagtion Symposium*, pp. 1122–1132, 2008.

[55] J. C. Doyle, K. Glover, P. Khargonekar, and B. A. Francis, "State-space solution to standard $H_2$ and $H_\infty$ control problem," *IEEE Transaction on Automatic Control*, no. 8, pp. 831–847, 1989.

[56] K. Zhou and J. C. Doyle, *Essentials of Robust Control.* Prentice Hall, 1998.

[57] G. J. Balas, "Robust control of flexible structures: Theory and experiments," Ph.D. dissertation, California Institute of Technology, 1990.

[58] J.-Y. Shin, "Worst-case analysis and linear parameter-varying gain scheduled control of aerospace systems," Ph.D. dissertation, University of Minnesota, 2000.

[59] J. Ledin, *Embedded Control Systems in C/C++: An Introduction for Software Devlopers Using Matlab.* CMP Books, 2004.

[60] G. F. Franklin, J. D. Powell, and A. Emami-Naeini, *Feedback Control of Dynamic Systems.* Prentice Hall, 2002.

[61] Matlab and Simulink, *Real-Time Windows Target 3 User's Guide.* The MathWorks Inc, 2008.

# Appendix A

# Physical Parameters Data

## A.1 Simulator Parameter Tuning

| | | | |
|---|---|---|---|
| $C_{L_0}$ | $2.30 \times 10^{-1}$ | $c_{l_{\delta a}}$ | $8.55 \times 10^{-2}$ |
| $C_{L_\alpha}$ | 4.58 | $c_{l_{\delta r}}$ | $-2.40 \times 10^{-3}$ |
| $C_{L_{\dot{\alpha}}}$ | 1.97 | $c_{l_p}$ | $-5.05 \times 10^{-1}$ |
| $C_{L_q}$ | 7.95 | $c_{l_r}$ | $2.52 \times 10^{-1}$ |
| $C_{L_{min}}$ | $2.30 \times 10^{-1}$ | $c_{m_0}$ | $1.35 \times 10^{-1}$ |
| $C_{D_0}$ | $4.34 \times 10^{-2}$ | $c_{m_\alpha}$ | -1.50 |
| $C_{D_{\delta e}}$ | $1.35 \times 10^{-2}$ | $c_{m_{\delta e}}$ | $-9.92 \times 10^{-1}$ |
| $C_{D_{\delta r}}$ | $3.03 \times 10^{-2}$ | $c_{m_{\dot{\alpha}}}$ | $-1.04 \times 10^{1}$ |
| $C_{Y_\beta}$ | $-8.30 \times 10^{-1}$ | $c_{m_q}$ | $-3.82 \times 10^{1}$ |
| $C_{Y_{\delta r}}$ | $1.91 \times 10^{-1}$ | $c_{n_\beta}$ | $7.26 \times 10^{-2}$ |
| $C_{Y_p}$ | 0.00 | $c_{n_{\delta r}}$ | $-6.93 \times 10^{-2}$ |
| $C_{Y_r}$ | 0.00 | $c_{n_p}$ | $-6.90 \times 10^{-2}$ |
| $c_{l_\beta}$ | $-1.30 \times 10^{-1}$ | $c_{n_r}$ | $-9.46 \times 10^{-2}$ |

Table A.1: Aerodynamic coefficients obtained from simulator parameter tuning

## A.2 Moment of Inertia Measurement

### A.2.1 Aircraft Moment of Inertia Measurement

The Ultrastick aircraft moment of inertia is determined using compound pendulum method [9]. For a compound pendulum shown in Figure A.1, the moment of inertia of the mass $I_{mass}$ ($kgm^2$) is related to its natural frequency $\omega_n$ (rad/s) with small angular amplitude oscillations:

$$\omega_n = \sqrt{\frac{mgL}{I_{mass} + mL^2}} \tag{A.1}$$

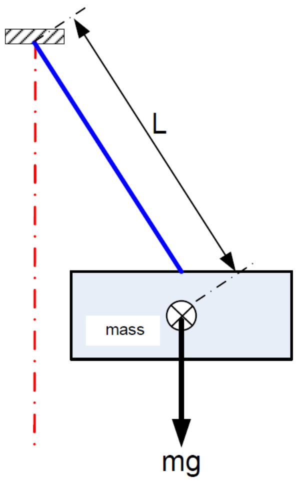

Figure A.1: Description of compound pendulum method setup

The relationship between damped frequency $\omega_d$ (rad/s), natural frequency $\omega_n$ (rad/s) and undamped frequency $\omega_{ud}$ is:

$$\omega_n = \sqrt{\omega_d^2 + \omega_{ud}^2} \tag{A.2}$$

The natural frequency of the oscillations is determined using Equation A.2 with the damped and undamped frequency measured using the compound pendulum experiment. The damped frequency is given by a single period of oscillation $T_p$ (s) for the pendulum motion:

$$\omega_d = \frac{2\pi}{T_p}$$

The undamped frequency is approximated using the exponent equation for the pendulum motion oscillation, $e^{\omega T}$. This can be written as $e^{-t/\tau}$, where $\tau$ (s) is the time constant. For oscillation motion to die out (exponent equation becomes zero and $t = T_f$), this time can be approximated with $t = 5\tau$. Therefore, the undamped natural frequency computed by:

$$\omega_{ud} = \frac{5}{T_f} \tag{A.3}$$

Figure A.2 shows the setup of the moment of inertia measurement for the Ultrastick aircraft. In the pendulum swing, the time taken for 10 oscillations (to compute $T_p$) and for the oscillations to die out ($T_f$) are taken. 3 sets of data are taken for each axis to determine the natural frequency for small angular oscillations and the moment of inertia is calculated with Equation A.1.

The largest and the smallest moment of inertia values are used as the upper and lower bound value while the mean value between these two bounds is the nominal value for the aircraft moment of inertia. These values are given in Appendix Table A.2.

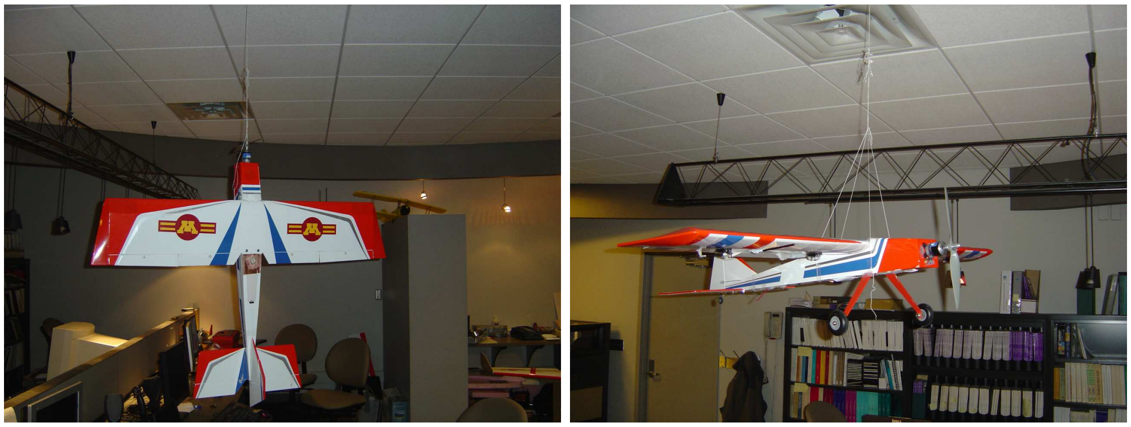

(a) Pendulum swing setup for $I_{zz}$ determination (b) Pendulum swing setup for $I_{xx}$ and $I_{yy}$ determination

Figure A.2: Setup for aircraft moment of inertia measurement

### A.2.2 Propulsion Moment of Inertia Measurement

The propulsion system moment of inertia measurement determines the moment of inertia contributed by rotating components from the propulsion system. These components include:

- Propeller
- Electric motor
- Propeller adaptor

These components are rotating about a common axis and are semi-semi-symmetrical about the aircraft body x-axis. The moment of inertia of the propulsion system is measured as a composite assembled system using bifilar pendulum method. This approach uses the period of the composite system undamped oscillations to calculate the moment of inertia of the propulsion system.

$$J_p = \left(\frac{T_n}{2\pi}\right)\frac{mgR^2}{L} \tag{A.4}$$

where

- $J$ = moment of inertia of the composite system ($kgm^2$)
- $T_n$ = undamped oscillation period (s)
- $m$ = mass of the composite system (kg)
- $g$ = gravitational constant ($9.81m/s^2$)
- $R$ = radius of the gyration (m)
- $L$ = length of the pendulum (m)

Figure A.3(a) shows the description of the bifilar pendulum system setup.

A 20 degrees anglular displacement is applied to the bifiar pendulum setup shown in Figure A.3(b) so that the pendulum system oscillates about the propeller axis of rotation. The time taken for 5 oscillation cycles is measured and the period taken for a single oscillation is used in Equation A.4 to compute the propulsion system moment of inertia. Two more data sets are taken and the moment of inertia are computed. The largest and the smallest moment of inertia values are used as the upper and lower bound values while the mean value between these two bounds is the nominal value for the propulsion system moment of inertia. These values are given in Appendix Table A.2.

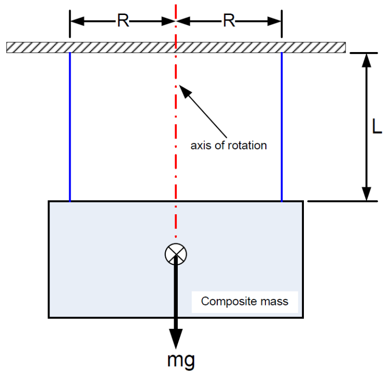

(a) Description of bifilar pendulum setup

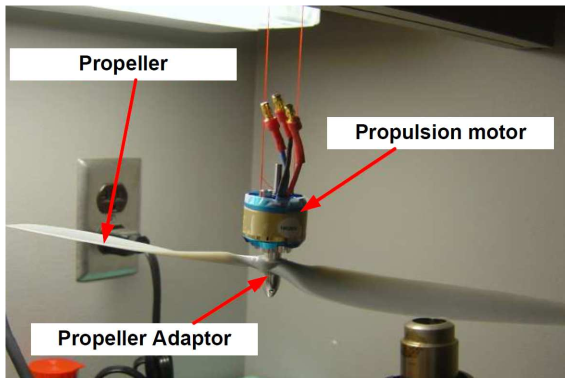

(b) Propulsion system moment of inertia measurement

Figure A.3: Bifilar pendulum system setup

### A.2.3 Summary of Moment of Inertia Data

| Moment of inertia | Lower bound | Nominal | Upper bound |
|---|---|---|---|
| $I_{xx}$ $(kgm^2)$ | $7.74 \times 10^{-2}$ | $8.94 \times 10^{-2}$ | $1.03 \times 10^{-1}$ |
| $I_{yy}$ $(kgm^2)$ | $1.24 \times 10^{-1}$ | $1.44 \times 10^{-1}$ | $1.59 \times 10^{-1}$ |
| $I_{zz}$ $(kgm^2)$ | $1.34 \times 10^{-1}$ | $1.62 \times 10^{-1}$ | $1.99 \times 10^{-1}$ |
| $I_{xz}$ $(kgm^2)$ | $1.12 \times 10^{-2}$ | $1.40 \times 10^{-2}$ | $1.68 \times 10^{-2}$ |
| $I_p$ $(kgm^2)$ | $1.29 \times 10^{-4}$ | $1.30 \times 10^{-4}$ | $1.31 \times 10^{-4}$ |

Table A.2: Moment of inertia data

## A.3 Propeller Characteristics

| Advance ratio ($J$) | Coefficient of thrust ($C_T$) | Coefficient of power ($C_P$) |
|---|---|---|
| $4.00 \times 10^{-2}$ | $1.00 \times 10^{-2}$ | $4.50 \times 10^{-2}$ |
| $1.30 \times 10^{-1}$ | $9.60 \times 10^{-2}$ | $4.50 \times 10^{-2}$ |
| $2.60 \times 10^{-1}$ | $8.60 \times 10^{-2}$ | $4.80 \times 10^{-2}$ |
| $3.30 \times 10^{-1}$ | $8.25 \times 10^{-2}$ | $4.80 \times 10^{-2}$ |
| $3.80 \times 10^{-1}$ | $8.00 \times 10^{-2}$ | $4.80 \times 10^{-2}$ |
| $4.40 \times 10^{-1}$ | $6.75 \times 10^{-2}$ | $4.60 \times 10^{-2}$ |
| $5.10 \times 10^{-1}$ | $5.40 \times 10^{-2}$ | $4.30 \times 10^{-2}$ |
| $5.90 \times 10^{-1}$ | $4.10 \times 10^{-2}$ | $3.75 \times 10^{-2}$ |
| $6.40 \times 10^{-1}$ | $3.00 \times 10^{-2}$ | $3.25 \times 10^{-2}$ |
| $7.00 \times 10^{-1}$ | $2.00 \times 10^{-2}$ | $2.88 \times 10^{-2}$ |

Table A.3: Propeller performance data for APC 12 x 8E propeller

## A.4 Control Surfaces Limits

| Control Surface | Lower limit (deg) | Upper limit (deg) |
|---|---|---|
| Aileron | -23 | 23 |
| Elevator | -20 | 20 |
| Rudder | -25 | 25 |

Table A.4: Control surfaces saturation limits

# Appendix B

# Linearization Result

## B.1 Operating Point Condition

| States | Trim value | Output | Trim value | Control input | Trim value |
|---|---|---|---|---|---|
| $u\ (m/s)$ | $1.70 \times 10^1$ | $V_a\ (m/s)$ | $1.70 \times 10^1$ | $\delta_e\ (rad)$ | $9.10 \times 10^{-2}$ |
| $v\ (m/s)$ | $3.00 \times 10^{-2}$ | $\beta\ (deg)$ | $1.00 \times 10^{-1}$ | $\delta_a\ (rad)$ | $1.01 \times 10^{-2}$ |
| $w\ (m/s)$ | $3.70 \times 10^{-1}$ | $\alpha\ (deg)$ | 1.24 | $\delta_r\ (rad)$ | -6.70 $\times 10^{-2}$ |
| $p\ (deg/s)$ | 0.00 | $\phi\ (deg)$ | $1.00 \times 10^{-1}$ | $\delta_T\ (\%)$ | $4.25 \times 10^1$ |
| $q\ (deg/s)$ | 0.00 | $\theta\ (deg)$ | $2.50 \times 10^{-1}$ | | |
| $r\ (deg/s)$ | 0.00 | $\psi\ (deg)$ | $3.16 \times 10^2$ | | |
| $\phi\ (deg)$ | $1.00 \times 10^{-1}$ | $h\ (m)$ | $1.00 \times 10^2$ | | |
| $\theta\ (deg)$ | $2.50 \times 10^{-1}$ | | | | |
| $\psi\ (deg)$ | $-4.36 \times 10^1$ | | | | |
| $h\ (m)$ | $1.00 \times 10^2$ | | | | |
| $\omega_p\ (rad/s)$ | $5.09 \times 10^2$ | | | | |

Table B.1: Trim operating point condition

## B.2 Full Linearized Model

$$\mathbf{A}_f = \begin{bmatrix} -0.444 & -0.000 & 0.594 & 0.000 & -9.794 & 0.000 & 0.000 & 0.000 & -0.362 & -0.019 & 0.0134 \\ -0.003 & -1.476 & 0.000 & 9.794 & 0.002 & 0.000 & 0.000 & 0.368 & 0.000 & -16.997 & 0.000 \\ -0.983 & 0.001 & -7.804 & -0.012 & 0.482 & 0.000 & 0.001 & 0.019 & 15.322 & 0.000 & 0.000 \\ 0.000 & 0.000 & 0.000 & 0.000 & -0.000 & 0.000 & 0.000 & 1.000 & -0.000 & -0.049 & 0.000 \\ 0.000 & 0.000 & 0.000 & 0.000 & 0.000 & 0.000 & 0.000 & 0.000 & 1.000 & -0.001 & 0.000 \\ 0.000 & 0.000 & 0.000 & -0.000 & 0.0000 & 0.000 & 0.000 & 0.000 & 0.001 & 1.001 & 0.000 \\ 0.000 & 0.000 & 0.000 & 0.000 & 0.000 & 0.000 & 0.000 & 0.000 & 0.000 & 0.000 & 0.000 \\ 0.090 & -5.703 & 0.002 & 0.000 & 0.000 & 0.000 & -0.000 & -21.709 & 0.000 & -6.809 & 0.002 \\ 0.180 & -0.000 & -8.310 & 0.000 & 0.000 & 0.000 & -0.000 & -0.000 & -35.203 & -0.000 & 0.000 \\ 0.010 & 1.329 & 0.000 & 0.000 & 0.000 & 0.000 & -0.000 & -0.100 & 0.000 & -2.698 & 0.000 \\ 136.660 & -0.152 & 2.962 & 0.000 & 0.000 & 0.000 & 0.054 & 0.000 & 0.000 & 0.000 & -8.501 \end{bmatrix}$$

$$\mathbf{B}_f = \begin{bmatrix} -0.000 & 0.001 & 0.001 & 0.000 \\ 0.000 & 0.002 & 0.006 & 0.000 \\ -0.004 & 0.000 & 0.000 & 0.000 \\ 0.000 & 0.000 & 0.000 & 0.000 \\ 0.000 & 0.000 & 0.000 & 0.000 \\ 0.000 & 0.000 & 0.000 & 0.000 \\ 0.000 & 0.000 & 0.000 & 0.000 \\ 0.000 & -0.105 & -0.003 & -0.006 \\ -0.106 & 0.000 & 0.000 & 0.000 \\ 0.000 & -0.006 & -0.012 & -0.001 \\ 0.000 & 0.000 & 0.000 & 3.894 \end{bmatrix} \times 10^3$$

$$\mathbf{C}_f = \begin{bmatrix} 1.000 & -0.001 & 0.022 & 0.000 & 0.000 & 0.000 & 0.000 & 0.000 & 0.000 & 0.000 & 0.000 \\ 0.000 & 0.059 & 0.000 & 0.000 & 0.000 & 0.000 & 0.000 & 0.000 & 0.000 & 0.000 & 0.000 \\ -0.001 & 0.000 & 0.059 & 0.000 & 0.000 & 0.000 & 0.000 & 0.000 & 0.000 & 0.000 & 0.000 \\ 0.000 & 0.000 & 0.000 & 1.000 & 0.000 & 0.000 & 0.000 & 0.000 & 0.000 & 0.000 & 0.000 \\ 0.000 & 0.000 & 0.000 & 0.000 & 1.000 & 0.000 & 0.000 & 0.000 & 0.000 & 0.000 & 0.000 \\ 0.000 & 0.000 & 0.000 & 0.000 & 0.000 & 1.000 & 0.000 & 0.000 & 0.000 & 0.000 & 0.000 \\ 0.000 & 0.000 & 0.000 & 0.000 & 0.000 & 0.000 & 1.000 & 0.000 & 0.000 & 0.000 & 0.000 \end{bmatrix}$$

$$\mathbf{D}_f = \begin{bmatrix} 0.000 & 0.000 & 0.000 & 0.000 \\ 0.000 & 0.000 & 0.000 & 0.000 \\ 0.000 & 0.000 & 0.000 & 0.000 \\ 0.000 & 0.000 & 0.000 & 0.000 \\ 0.000 & 0.000 & 0.000 & 0.000 \\ 0.000 & 0.000 & 0.000 & 0.000 \\ 0.000 & 0.000 & 0.000 & 0.000 \end{bmatrix}$$

## B.3 Decoupled Linear Model

$$\mathbf{A}_{lon} = \begin{bmatrix} -0.444 & 0.594 & -0.362 & -9.794 & 0.000 & 0.014 \\ -0.983 & -7.804 & 15.322 & 0.481 & 0.001 & 0.000 \\ 0.180 & -8.310 & -35.203 & 0.000 & -0.000 & 0.000 \\ 0.000 & 0.000 & 1.000 & 0.000 & 0.000 & 0.000 \\ 0.000 & 0.000 & 0.000 & 0.000 & 0.000 & 0.000 \\ 136.660 & 2.962 & 0.000 & 0.000 & 0.054 & -8.501 \end{bmatrix}$$

$$\mathbf{B}_{lon} = \begin{bmatrix} -0.000 & 0.000 \\ -0.004 & 0.000 \\ -0.106 & 0.000 \\ 0.000 & 0.000 \\ 0.000 & 0.000 \\ 0.000 & 3.894 \end{bmatrix} \times 10^3$$

$$\mathbf{C}_{lon} = \begin{bmatrix} 1.000 & 0.022 & 0.000 & 0.000 & 0.000 & 0.000 \\ -0.001 & 0.059 & 0.000 & 0.000 & 0.000 & 0.000 \\ 0.000 & 0.000 & 1.000 & 0.000 & 0.000 & 0.000 \\ 0.000 & 0.000 & 0.000 & 1.000 & 0.000 & 0.000 \\ 0.000 & 0.000 & 0.000 & 0.000 & 1.000 & 0.000 \end{bmatrix}$$

$$\mathbf{D}_{lon} = \begin{bmatrix} 0.000 & 0.000 \\ 0.000 & 0.000 \\ 0.000 & 0.000 \\ 0.000 & 0.000 \\ 0.000 & 0.000 \end{bmatrix}$$

$$\mathbf{A}_{lat} = \begin{bmatrix} -1.476 & 0.368 & -16.997 & 9.794 & 0.000 \\ -5.703 & -21.709 & -6.809 & 0.000 & 0.000 \\ 1.329 & -0.100 & -2.698 & 0.000 & 0.000 \\ 0.000 & 1.000 & -0.049 & 0.000 & 0.000 \\ 0.000 & 0.000 & 1.001 & 0.000 & 0.000 \end{bmatrix}$$

$$\mathbf{B}_{lat} = \begin{bmatrix} 2.147 & 5.480 \\ -105.001 & -2.792 \\ -6.131 & -12.398 \\ 0.000 & 0.000 \\ 0.000 & 0.000 \end{bmatrix}$$

$$\mathbf{C}_{lat} = \begin{bmatrix} 0.059 & 0.000 & 0.000 & 0.000 & 0.000 \\ 0.000 & 1.000 & 0.000 & 0.000 & 0.000 \\ 0.000 & 0.000 & 1.000 & 0.000 & 0.000 \\ 0.000 & 0.000 & 0.000 & 1.000 & 0.000 \\ 0.000 & 0.000 & 0.000 & 0.000 & 1.000 \end{bmatrix}$$

$$\mathbf{D}_{lat} = \begin{bmatrix} 0.000 & 0.000 \\ 0.000 & 0.000 \\ 0.000 & 0.000 \\ 0.000 & 0.000 \end{bmatrix}$$

## B.4 Open Loop ID Results

### B.4.1 Model 2 Parameter Identification

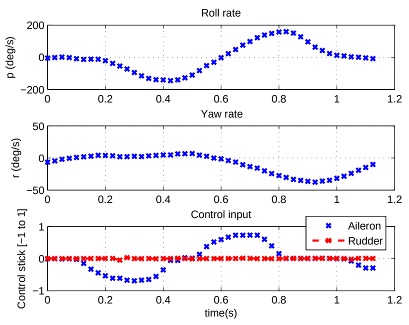

(a) Aileron control excitation

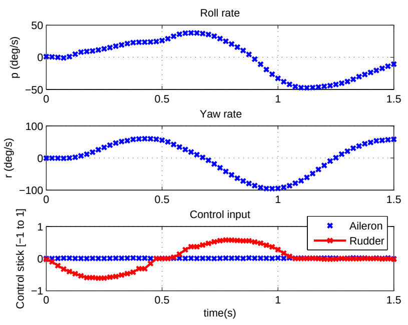

(b) Rudder control excitation

Figure B.1: Flight test data for model 2 parameter identification

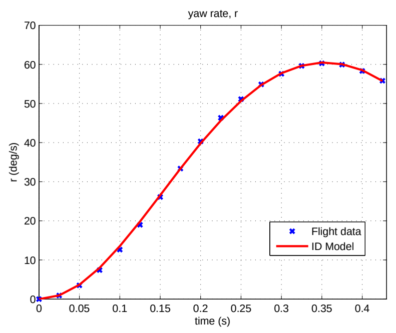

(a) Step 1

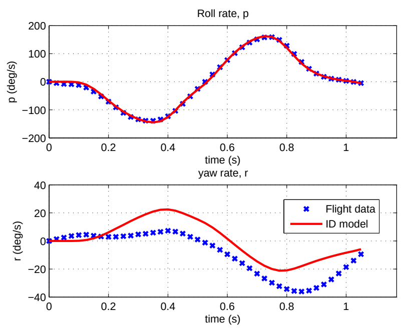

(b) Step 2

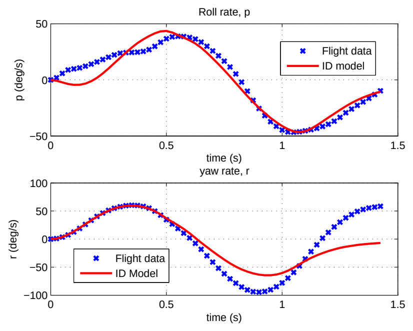

(c) Step 3

Figure B.2: Model 2 parameter identification

### B.4.2 Model 3 Parameter Identification

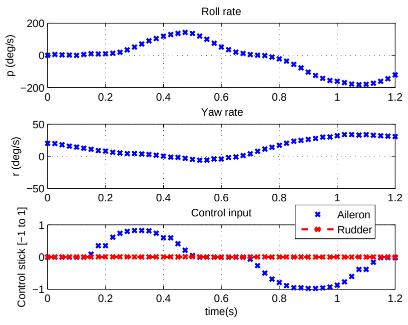

(a) Aileron control excitation

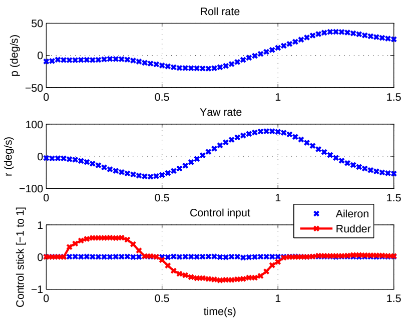

(b) Rudder control excitation

Figure B.3: Flight test data for model 3 parameter identification

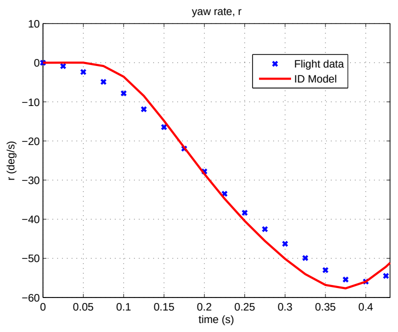

(a) Step 1

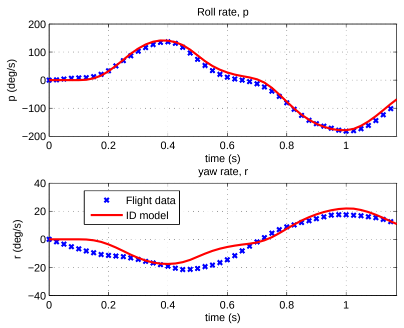

(b) Step 2

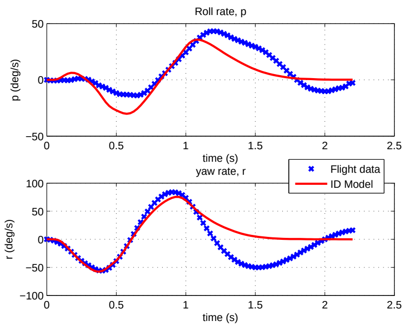

(c) Step 3

Figure B.4: Model 3 parameter identification

## B.5 Nominal Model Computed

| Derivatives | Lower bound | Nominal value | Upper bound |
|---|---|---|---|
| $L_p(s^{-1})$ | $-1.28 \times 10^1$ | $-1.20 \times 10^1$ | $-1.11 \times 10^1$ |
| $L_r(s^{-1})$ | $8.62 \times 10^0$ | $1.15 \times 10^1$ | $1.44 \times 10^1$ |
| $N_p(s^{-1})$ | $-4.48 \times 10^{-1}$ | $1.20 \times 10^{-1}$ | $6.87 \times 10^{-1}$ |
| $N_r(s^{-1})$ | $-8.48 \times 10^0$ | $-6.55 \times 10^0$ | $-4.62 \times 10^1$ |
| $L_{\delta_a}(s^{-2})$ | $4.33 \times 10^1$ | $5.24 \times 10^1$ | $6.14 \times 10^1$ |
| $L_{\delta_r}(s^{-2})$ | $8.99 \times 10^0$ | $1.13 \times 10^1$ | $1.36 \times 10^1$ |
| $N_{\delta_a}(s^{-2})$ | $-6.58 \times 10^0$ | $-5.13 \times 10^0$ | $-3.67 \times 10^0$ |
| $N_{\delta_r}(s^{-2})$ | $-1.75 \times 10^1$ | $-1.47 \times 10^1$ | $-11.9 \times 10^1$ |

Table B.2: Nominal model with upper and lower bounds

# Appendix C

# Uncertainty Modeling

## C.1 Aerodynamic Coefficients Parametric Uncertainty

| Aerodynamic coefficient | Lower bound | Nominal | Upper bound |
|---|---|---|---|
| $c_{l_p}$ | $-4.43 \times 10^{-1}$ | $-4.14 \times 10^{-1}$ | $-3.84 \times 10^{-1}$ |
| $c_{l_r}$ | $2.99 \times 10^{-1}$ | $3.99 \times 10^{-1}$ | $4.99 \times 10^{-1}$ |
| $c_{n_p}$ | $-2.81 \times 10^{-2}$ | $-7.50 \times 10^{-3}$ | $4.31 \times 10^{-2}$ |
| $c_{n_r}$ | $-5.32 \times 10^{-1}$ | $-4.11 \times 10^{-1}$ | $-2.90 \times 10^{-1}$ |
| $c_{l_{\delta a}}$ | $5.60 \times 10^{-2}$ | $6.77 \times 10^{-2}$ | $7.94 \times 10^{-2}$ |
| $c_{l_{\delta r}}$ | $1.60 \times 10^{-2}$ | $1.68 \times 10^{-2}$ | $1.76 \times 10^{-2}$ |
| $c_{n_{\delta a}}$ | $-1.54 \times 10^{-2}$ | $-1.20 \times 10^{-2}$ | $-8.60 \times 10^{-3}$ |
| $c_{n_{\delta r}}$ | $-4.10 \times 10^{-2}$ | $-3.45 \times 10^{-2}$ | $-2.79 \times 10^{-2}$ |

Table C.1: Aerodynamic coefficients nominal, lower and upper bound values

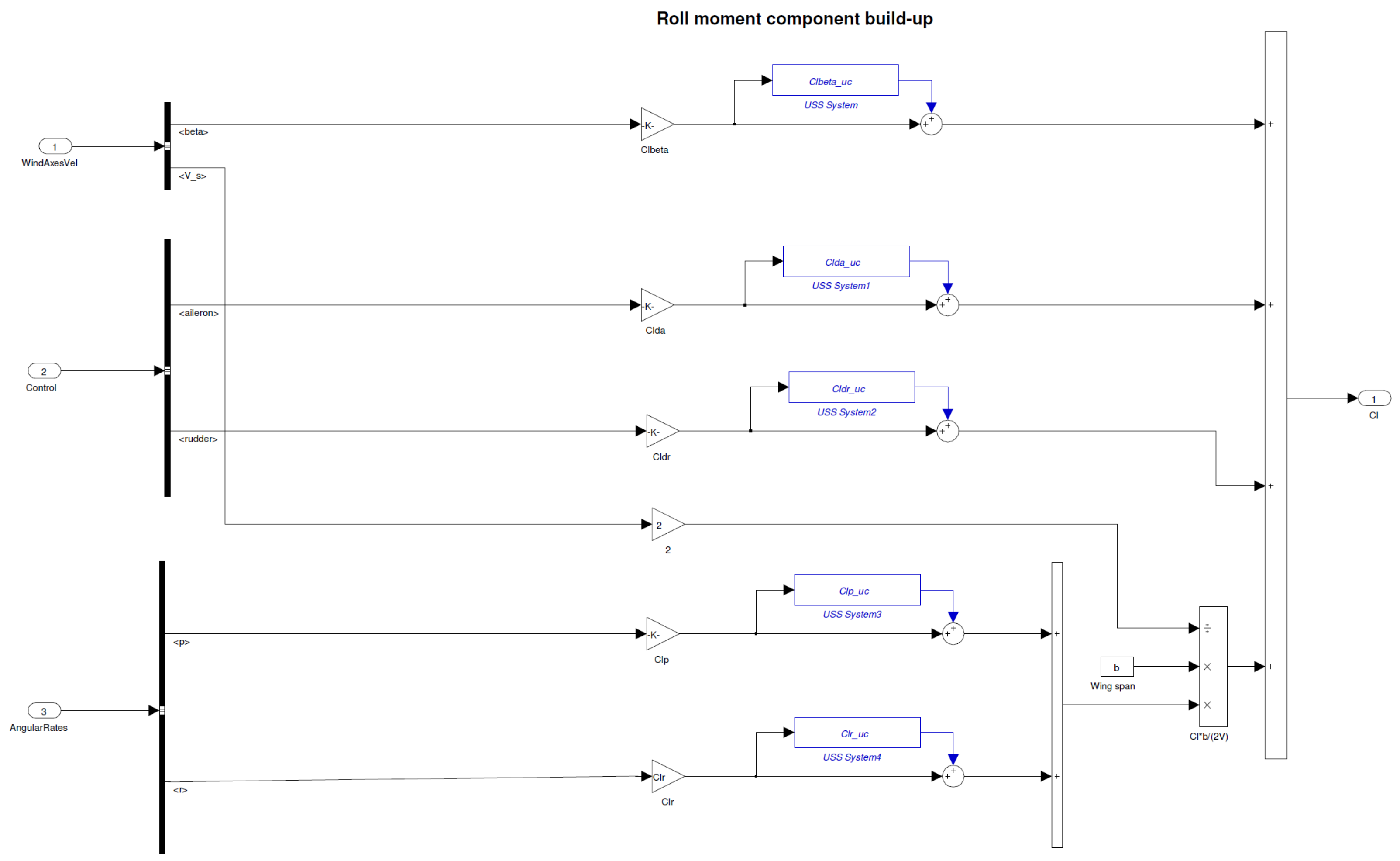

Figure C.1: Simulink model with real parametric uncertainties for dimensionless roll moment coefficient

| Physical parameter | Lower bound | Nominal | Upper bound |
|---|---|---|---|
| $C_{L_0}$ | $2.19 \times 10^{-1}$ | $2.30 \times 10^{-1}$ | $2.42 \times 10^{-1}$ |
| $C_{L_\alpha}$ | 4.35 | 4.58 | 4.81 |
| $C_{L_{de}}$ | $1.24 \times 10^{-1}$ | $1.30 \times 10^{-1}$ | $1.37 \times 10^{-1}$ |
| $C_{L_{\dot{\alpha}}}$ | 1.87 | 1.97 | 2.07 |
| $C_{L_q}$ | 7.56 | 7.95 | 8.35 |
| $C_{L_{minD}}$ | $2.19 \times 10^{-1}$ | $2.30 \times 10^{-1}$ | $2.42 \times 10^{-1}$ |
| $C_{D_{min}}$ | $4.12 \times 10^{-2}$ | $4.34 \times 10^{-2}$ | $4.56 \times 10^{-2}$ |
| $C_{D_{de}}$ | $1.28 \times 10^{-2}$ | $1.35 \times 10^{-2}$ | $1.42 \times 10^{-2}$ |
| $C_{D_{dr}}$ | $2.88 \times 10^{-2}$ | $3.03 \times 10^{-2}$ | $3.18 \times 10^{-2}$ |
| $C_{D_{da}}$ | $2.87 \times 10^{-2}$ | $3.02 \times 10^{-2}$ | $3.17 \times 10^{-2}$ |
| $C_{Y_\beta}$ | $-8.72 \times 10^{-1}$ | $-8.30 \times 10^{-1}$ | $-7.86 \times 10^{-1}$ |
| $C_{Y_{dr}}$ | $1.82 \times 10^{-1}$ | $1.91 \times 10^{-1}$ | $2.01 \times 10^{-1}$ |
| $c_{m_0}$ | $1.28 \times 10^{-1}$ | $1.35\times 10^{-1}$ | $1.42 \times 10^{-1}$ |
| $c_{m_\alpha}$ | -1.58 | -1.50 | -1.43 |
| $c_{m_{de}}$ | -1.18 | -1.13 | -1.07 |
| $c_{m_{\dot{\alpha}}}$ | $-1.09\times 10^{1}$ | $-1.04\times 10^{1}$ | -9.86 |
| $c_{m_q}$ | $-5.37\times 10^{1}$ | $-5.08\times 10^{1}$ | $-4.83\times 10^{1}$ |
| $c_{n_\beta}$ | $3.27 \times 10^{-2}$ | $3.44 \times 10^{-2}$ | $3.61 \times 10^{-2}$ |
| $c_{n_{da}}$ | $-1.54 \times 10^{-2}$ | $-1.20 \times 10^{-2}$ | $-8.60 \times 10^{-2}$ |
| $c_{n_{dr}}$ | $-4.10 \times 10^{-2}$ | $-3.45 \times 10^{-2}$ | $-2.79 \times 10^{-2}$ |
| $c_{n_p}$ | $-2.81 \times 10^{-2}$ | $-7.50 \times 10^{-2}$ | $-4.31 \times 10^{-2}$ |
| $c_{n_r}$ | $-5.32\times 10^{-1}$ | $-4.11\times 10^{-1}$ | $-2.90\times 10^{-1}$ |
| $c_{l_\beta}$ | $-4.20 \times 10^{-2}$ | $-4.00 \times 10^{-2}$ | $-3.80 \times 10^{-2}$ |
| $c_{l_{da}}$ | $5.60 \times 10^{-2}$ | $6.77 \times 10^{-2}$ | $7.94 \times 10^{-2}$ |
| $c_{l_{dr}}$ | $1.60 \times 10^{-2}$ | $1.68 \times 10^{-2}$ | $1.76 \times 10^{-2}$ |
| $c_{l_p}$ | $-4.43\times 10^{-1}$ | $-4.14\times 10^{-1}$ | $-3.84\times 10^{-1}$ |
| $c_{l_r}$ | $2.99\times 10^{-1}$ | $3.99\times 10^{-1}$ | $4.99\times 10^{-1}$ |
| $I_{xx}$ | $7.74 \times 10^{-2}$ | $8.94 \times 10^{-2}$ | $1.03 \times 10^{-1}$ |
| $I_{yy}$ | $1.24 \times 10^{-1}$ | $1.44 \times 10^{-1}$ | $1.59 \times 10^{-1}$ |
| $I_{zz}$ | $1.34 \times 10^{-1}$ | $1.62 \times 10^{-1}$ | $1.99 \times 10^{-1}$ |
| $I_{xz}$ | $1.12 \times 10^{-2}$ | $1.40 \times 10^{-2}$ | $1.68 \times 10^{-2}$ |
| $J_{m_p}$ | $1.29 \times 10^{-4}$ | $1.30 \times 10^{-4}$ | $1.31 \times 10^{-4}$ |

Table C.2: List of parameters with its nominal, lower and upper bound values

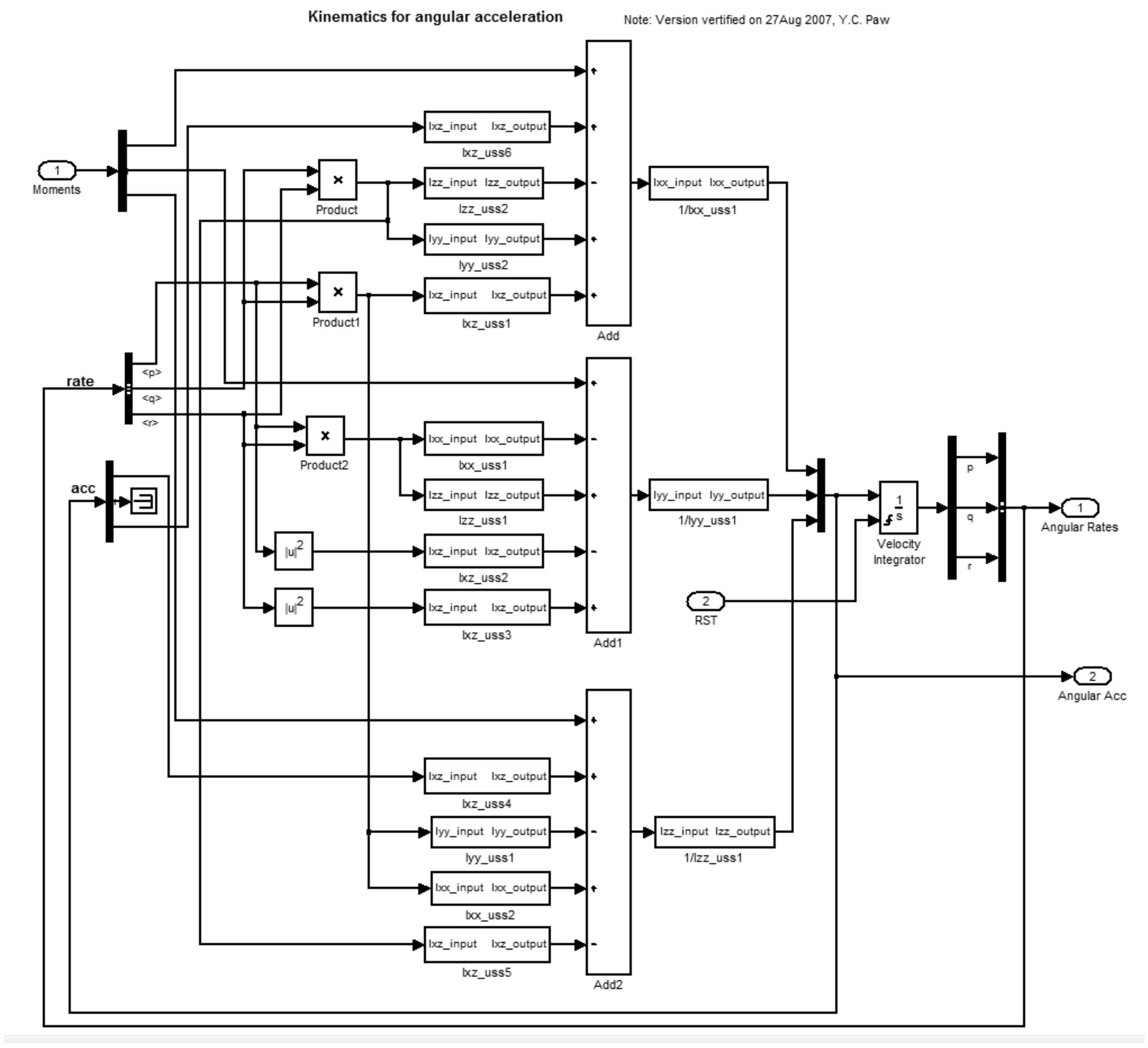

Figure C.2: Simulink model for angular acceleration kinematics

| Parametric uncertainty | Physical parameter | Lower bound | Nominal | Upper bound |
|---|---|---|---|---|
| $\delta_1$ | $C_{D_{da}}$ | -5.00 $\times 10^{-2}$ | 0 | 5.00 $\times 10^{-2}$ |
| $\delta_2$ | $C_{D_{de}}$ | -5.00 $\times 10^{-2}$ | 0 | 5.00 $\times 10^{-2}$ |
| $\delta_3$ | $C_{D_{dr}}$ | -5.00 $\times 10^{-2}$ | 0 | 5.00 $\times 10^{-2}$ |
| $\delta_4$ | $C_{D_{min}}$ | -5.00 $\times 10^{-2}$ | 0 | 5.00 $\times 10^{-2}$ |
| $\delta_5$ | $C_{L_0}$ | -5.00 $\times 10^{-2}$ | 0 | 5.00 $\times 10^{-2}$ |
| $\delta_6$ | $C_{L_\alpha}$ | -5.00 $\times 10^{-2}$ | 0 | 5.00 $\times 10^{-2}$ |
| $\delta_7$ | $C_{L_{\dot{\alpha}}}$ | -5.00 $\times 10^{-2}$ | 0 | 5.00 $\times 10^{-2}$ |
| $\delta_8$ | $C_{L_{de}}$ | -5.00 $\times 10^{-2}$ | 0 | 5.00 $\times 10^{-2}$ |
| $\delta_{9,10}$ | $C_{L_{minD}}$ | -5.00 $\times 10^{-2}$ | 0 | 5.00 $\times 10^{-2}$ |
| $\delta_{11}$ | $C_{L_q}$ | -5.00 $\times 10^{-2}$ | 0 | 5.00 $\times 10^{-2}$ |
| $\delta_{12}$ | $C_P$ | 9.500 $\times 10^{-1}$ | 1 | 1.05 |
| $\delta_{13}$ | $C_T$ | 9.500 $\times 10^{-1}$ | 1 | 1.05 |
| $\delta_{14}$ | $C_{Y_\beta}$ | -5.00 $\times 10^{-2}$ | 0 | 5.00 $\times 10^{-2}$ |
| $\delta_{15}$ | $C_{Y_{dr}}$ | -5.00 $\times 10^{-2}$ | 0 | 5.00 $\times 10^{-2}$ |
| $\delta_{16}$ | $c_{l_\beta}$ | -5.00 $\times 10^{-2}$ | 0 | 5.00 $\times 10^{-2}$ |
| $\delta_{17}$ | $c_{l_{da}}$ | -1.73 $\times 10^{-1}$ | 0 | 1.73 $\times 10^{-1}$ |
| $\delta_{18}$ | $c_{l_{dr}}$ | -4.77 $\times 10^{-2}$ | 0 | 4.77 $\times 10^{-2}$ |
| $\delta_{19}$ | $c_{l_p}$ | -7.00 $\times 10^{-2}$ | 0 | 7.25 $\times 10^{-2}$ |
| $\delta_{20}$ | $c_{l_r}$ | -2.51 $\times 10^{-1}$ | 0 | 2.51 $\times 10^{-1}$ |
| $\delta_{21}$ | $c_{m_0}$ | -5.00 $\times 10^{-2}$ | 0 | 5.00 $\times 10^{-2}$ |
| $\delta_{22}$ | $c_{m_\alpha}$ | -5.00 $\times 10^{-2}$ | 0 | 5.00 $\times 10^{-2}$ |
| $\delta_{23}$ | $c_{m_{\dot{\alpha}}}$ | -5.00 $\times 10^{-2}$ | 0 | 5.00 $\times 10^{-2}$ |
| $\delta_{24}$ | $c_{m_{de}}$ | -5.00 $\times 10^{-2}$ | 0 | 5.00 $\times 10^{-2}$ |
| $\delta_{25}$ | $c_{m_q}$ | -5.00 $\times 10^{-2}$ | 0 | 5.00 $\times 10^{-2}$ |
| $\delta_{26}$ | $c_{n_\beta}$ | -5.00 $\times 10^{-2}$ | 0 | 5.00 $\times 10^{-2}$ |
| $\delta_{27}$ | $c_{n_{da}}$ | -2.83 $\times 10^{-1}$ | 0 | 2.83 $\times 10^{-1}$ |
| $\delta_{28}$ | $c_{n_{dr}}$ | -1.88 $\times 10^{-1}$ | 0 | -1.91 $\times 10^{-1}$ |
| $\delta_{29}$ | $c_{n_p}$ | -2.75 | 0 | 6.75 |
| $\delta_{30}$ | $c_{n_r}$ | -2.94 $\times 10^{-1}$ | 0 | -2.94 $\times 10^{-1}$ |
| $\delta_{31}$ | $J_{m_p}$ | -7.00 $\times 10^{-3}$ | 0 | 8.39 $\times 10^{-3}$ |
| $\delta_{32,33,34}$ | $I_{xx}$ | -1.34 $\times 10^{-1}$ | 0 | 1.52 $\times 10^{-1}$ |
| $\delta_{35,36,37,38,39,40}$ | $I_{xz}$ | -2.00 $\times 10^{-1}$ | 0 | 2.00 $\times 10^{-1}$ |
| $\delta_{41,42,43}$ | $I_{yy}$ | -1.41 $\times 10^{-1}$ | 0 | 1.01 $\times 10^{-1}$ |
| $\delta_{44,45,46}$ | $I_{zz}$ | -1.73 $\times 10^{-1}$ | 0 | 2.28 $\times 10^{-1}$ |

Table C.3: $\Delta$ matrix of LFT realization using ulinearize

| **Parametric uncertainty** | **Physical parameter** | **Worst-case gain condition** |
|---|---|---|
| $\boldsymbol{\delta_1}$ | $C_{D_{da}}$ | $5.00 \times 10^{-2}$ |
| $\boldsymbol{\delta_2}$ | $C_{D_{de}}$ | $5.00 \times 10^{-2}$ |
| $\boldsymbol{\delta_3}$ | $C_{D_{dr}}$ | $5.00 \times 10^{-2}$ |
| $\boldsymbol{\delta_4}$ | $C_{D_{min}}$ | $-5.00 \times 10^{-2}$ |
| $\boldsymbol{\delta_5}$ | $C_{L_0}$ | $5.00 \times 10^{-2}$ |
| $\boldsymbol{\delta_6}$ | $C_{L_\alpha}$ | $5.00 \times 10^{-2}$ |
| $\boldsymbol{\delta_7}$ | $C_{L_{\dot{\alpha}}}$ | $5.00 \times 10^{-2}$ |
| $\boldsymbol{\delta_8}$ | $C_{L_{de}}$ | $-5.00 \times 10^{-2}$ |
| $\boldsymbol{\delta_{9,10}}$ | $C_{L_{minD}}$ | $5.00 \times 10^{-2}$ |
| $\boldsymbol{\delta_{11}}$ | $C_{L_q}$ | $5.00 \times 10^{-2}$ |
| $\boldsymbol{\delta_{12}}$ | $C_P$ | $9.500 \times 10^{-1}$ |
| $\boldsymbol{\delta_{13}}$ | $C_T$ | 1.05 |
| $\boldsymbol{\delta_{14}}$ | $C_{Y_\beta}$ | $-5.00 \times 10^{-2}$ |
| $\boldsymbol{\delta_{15}}$ | $C_{Y_{dr}}$ | $5.00 \times 10^{-2}$ |
| $\boldsymbol{\delta_{16}}$ | $c_{l_\beta}$ | $5.00 \times 10^{-2}$ |
| $\boldsymbol{\delta_{17}}$ | $c_{l_{da}}$ | $1.73 \times 10^{-1}$ |
| $\boldsymbol{\delta_{18}}$ | $c_{l_{dr}}$ | $-4.77 \times 10^{-2}$ |
| $\boldsymbol{\delta_{19}}$ | $c_{l_p}$ | $-7.00 \times 10^{-2}$ |
| $\boldsymbol{\delta_{20}}$ | $c_{l_r}$ | $2.51 \times 10^{-1}$ |
| $\boldsymbol{\delta_{21}}$ | $c_{m_0}$ | $5.00 \times 10^{-2}$ |
| $\boldsymbol{\delta_{22}}$ | $c_{m_\alpha}$ | $-5.00 \times 10^{-2}$ |
| $\boldsymbol{\delta_{23}}$ | $c_{m_{\dot{\alpha}}}$ | $5.00 \times 10^{-2}$ |
| $\boldsymbol{\delta_{24}}$ | $c_{m_{de}}$ | $5.00 \times 10^{-2}$ |
| $\boldsymbol{\delta_{25}}$ | $c_{m_q}$ | $-5.00 \times 10^{-2}$ |
| $\boldsymbol{\delta_{26}}$ | $c_{n_\beta}$ | $-5.00 \times 10^{-2}$ |
| $\boldsymbol{\delta_{27}}$ | $c_{n_{da}}$ | $-2.83 \times 10^{-1}$ |
| $\boldsymbol{\delta_{28}}$ | $c_{n_{dr}}$ | $1.91 \times 10^{-1}$ |
| $\boldsymbol{\delta_{29}}$ | $c_{n_p}$ | -2.75 |
| $\boldsymbol{\delta_{30}}$ | $c_{n_r}$ | $-2.94 \times 10^{-1}$ |
| $\boldsymbol{\delta_{31}}$ | $J_{m_p}$ | $-7.00 \times 10^{-3}$ |
| $\boldsymbol{\delta_{32,33,34}}$ | $I_{xx}$ | $-1.34 \times 10^{-1}$ |
| $\boldsymbol{\delta_{35,36,37,38,39,40}}$ | $I_{xz}$ | $2.00 \times 10^{-1}$ |
| $\boldsymbol{\delta_{41,42,43}}$ | $I_{yy}$ | $1.01 \times 10^{-1}$ |
| $\boldsymbol{\delta_{44,45,46}}$ | $I_{zz}$ | $-1.73 \times 10^{-1}$ |

Table C.4: $\Delta$ matrix of worst-case gain condition at 5 rad/s